Discovering Genetic Modifiers in Niemann-Pick Disease Type C

Jorge L. Rodriguez-Gil

A thesis presented for the degree of Doctor of Philosophy



Department of Pharmacology
Nuffield Department of Medicine
St Hugh's College
University of Oxford
Trinity Term 2019

Abstract

Niemann-Pick Disease, Type C (NPC) is a rare, fatal neurodegenerative disorder characterized by lysosomal accumulation of unesterified cholesterol and sphingolipids. These subcellular pathologies eventually cause phenotypes of hepatosplenomegaly and neurological degeneration leading to premature death. NPC is extremely heterogeneous in the timing of clinical presentation (prenatal to adulthood) and is associated with a wide spectrum of causative *NPC1* mutations. Miglustat (Zavesca) is the only approved therapy for NPC, and while it has been shown to improve clinical outcomes it is not a cure. To study the genetic architecture of NPC, including the clinical and genetic heterogeneity seen in this patient population, we have generated a new mouse model (*Npc1*^{em1Pav}). Using this model, we identified strain-specific quantitative trait loci (QTL) affecting lifespan and characterized a novel lung phenotype causing neonatal lethality. Interestingly, *Npc1*^{em1Pav} mutants on a C57BL/6J (B6J) genetic background had a more severe visceral pathology of foam cell accumulation than *Npc1*^{em1Pav} mutants on a BALB/cJ background. These underlying pathological changes translated into B6J mutants having a significantly shorter lifespan (70 $\pm$ 4.30 days) than mutants on a BALB/cJ background (84 $\pm$ 7.25; $p<0.0001$), suggesting strain-specific modifiers contribute to disease severity. QTL analysis of backcross N2 mutants detected significant linkage to markers on chromosomes 1 (LOD=5.57) and 7 (LOD=8.91). Analysis of predicted deleterious sequence variants between B6J and BALB/cJ strains at these two loci resulted in a short list of candidate genes that can now be evaluated as potential modifiers of NPC severity and progression.

A significant reduction of viable *Npc1*^{em1Pav} mice was also observed on the B6J background at Postnatal day 10 (P10) (10.5% vs. 25%, $p<0.0001$). Interestingly, the expected genotype frequency was observed at E18.5-E19.5 (26.5% % vs. 25%, $p=0.034$) indicating *Npc1*^{em1Pav} mutants exhibit a previously uncharacterized lethal phenotype postnatally. C-sections accompanied by maternal fostering confirmed that the majority of *Npc1*^{em1Pav} mutants died shortly after birth showing signs of respiratory insufficiency and abnormal surfactant pathology. A similar phenomenon reported in NPC patients with pre/perinatal onset indicates *Npc1*^{em1Pav} may be the first valid animal model of this severely affected group.

Acknowledgments

"What makes the desert beautiful is that somewhere it hides a well"

Antoine de Saint-Exupéry, The Little Prince

To my mom and Thad.

I would like to thank my two supervisors: Dr. Frances M. Platt and Dr. Bill Pavan for their mentorship and support. I have been so fortunate to have found great mentors and friends in both the NIH and Oxford. Special thanks to Dr. Laura Baxter and Dr. Dawn Watkins-Chow for their valuable input and scientific discussions. I would also like to thank all the members of the Platt and Pavan labs where I found myself surrounded by not only great colleagues but also great friends. Thank you to all collaborators from NIH, UW and Oxford. Finally, thank you to all the patients and their families for their unbreakable strength, courage and support.

Contents:

Abstract 3

Acknowledgments 5

List of figures 13

List of tables 17

Abbreviations 18

Chapter I: General Introduction 20

Lysosomal Storage Disorders 20

Niemann-Pick Type C Disease 22

Epidemiology and Genetics 22

Molecular Etiology 25

Clinical Manifestations of NPC 27

Pre/perinatal Onset 27

Infantile and Juvenile Onset 28

Adult Onset 28

Current Treatments 30

Investigational Therapies 30

Animal Models of Niemann-Pick Disease Type C1 31

Mouse Models 33

Genetic Modifiers in NPC 38

Chapter II: Generation of *Npc1*^{em1Pav} 39

Introduction 39

Materials and Methods 40

CRISPR/Cas9 Design 40
Off-target Effects 40
Synthesis of gRNA 40
Pronuclear Injection 43
Genotype Identification 43
Sanger Sequencing 46
cDNA Preparation 46
Colony Management 46
Nomenclature 47
Results 48
Targeted mutagenesis of *Npc1* with CRISPR/Cas9 results in a nine base-pair deletion 48
Npc1^{em1Pav} harbors a mutation located in the cysteine-rich domain of NPC1 52
Discussion 54
Summary 55

Chapter III: Characterization of *Npc1*^{em1Pav} 56

Introduction 56
Materials and Methods 57
Western Blot 57
RT-qPCR (RNA 57
Animal Perfusion and Tissue Harvest Protocol 58
Tissue Histology and Immunohistochemistry 57
Specialized Staining 59
Microscopy 59
Glycosphingolipid analysis 59

Sphingosine analysis 59
Behavioral Analysis 60
Lifespan Measurement 61
Colonies Management and Genotyping 61
Statistical Analysis 61
Results 63
Npc1^{em1Pav} is a hypomorphic allele 63
Npc1 mRNA levels in *Npc1*^{em1Pav} mutants do not correlate with NPC1 protein levels and are regulated in a tissue-specific manner 65
Biochemical profile of *Npc1*^{em1Pav} shows marked lipid accumulation consistent with NPC1 deficiency 67
Npc1^{em1Pav} mutants display classical storage pathology and neurodegenerative pattern consistent with NPC 69
Reduced lifespan and progressive weight loss onset in *Npc1*^{em1Pav} mutants 73
Npc1^{em1Pav} mutants display ataxia and other neurogenerative phenotypes characteristic of NPC 76
Discussion 78
Summary 80

Chapter IV: Using *Npc1*^{em1Pav} to map genetic modifiers of NPC **81**
Introduction 81
Materials and Methods 83
Mouse Strains 83

Speed Congenics 83
Lifespan Measurement for Mapping 83
Colony Management 84
DNA Extraction 84
Genotype of Samples Used for Genetic Mapping 84
Statistical Analysis 84
Genotype Data Analysis 85
QTL Linkage Analysis 85
Analysis of Candidate Genes 85
Results 87
Lifespan as a quantitative trait 87
BALB/cJ background increases survival in *Npc1*^{em1Pav} mutants 89
Breeding strategy and lifespan measurement for the N2 backcross generation 94
C57BL/6N and C57BL/6J have a similar effect on survival in *Npc1*^{em1Pav} mutants 98
Two QTL loci located on Chromosome 1 and 7 associated with survival in *Npc1*^{em1Pav} mutants 100
Identifying candidate genetic variants and genes within the QTL regions on chromosome 1 and 7 105
Severity of visceral pathology in *Npc1*^{em1Pav} mutants is modified by genetic background 117
Discussion 119
Strengths and limitations 123
Future work 124

Chapter V: Characterizing Neonatal Lethality in *Npc1*^{em1Pav} **125**

Introduction 125

Materials and Methods 126

Mouse Genetic Strains and *Npc1* Alleles 126

Colonies Genotyping and Management 126

Organ Weights and Dissections 127

Embryo and Tissue Histology/Staining and Immunohistochemistry 127

Hematoxylin and Eosin (H&E) Staining 127

Skeletal Preparations 128

Cesarean Delivery and Fostering Experiments 128

Medroxyprogesterone Injections 128

Dexamethasone Injections 128

Light Microscopy 129

Transmission Electron Microscopy 129

DNA Extraction 130

Genotype of Samples Used for Genetic Mapping 130

Genotype Data Analysis 130

QTL Linkage Analysis 130

Statistical Analysis 130

Results 131

Reduced postnatal viability of *Npc1*$^{em1Pav/em1Pav}$ offspring 131

Fetal growth restriction and low birth weight in *Npc1*$^{em1Pav/em1Pav}$ 133

Npc1 mutation leads to neonatal lethality in the majority of *Npc1*$^{em1Pav/em1Pav}$ 138

Respiratory insufficiency as a potential cause of neonatal lethality in *Npc1*$^{em1Pav/em1Pav}$ 141

Antenatal corticosteroid therapy does not increase neonatal survival in *Npc1*$^{em1Pav/em1Pav}$ 151

Severity of neonatal lethality in *Npc1*^{em1Pav} mutants depends on genetic background 153

Using genetic test-crosses in order to map genetic modifiers of neonatal lethality in *Npc1*$^{em1Pav/em1Pav}$ 155

Discussion 160

Strength and limitations 164

Future work 165

Chapter VI: Conclusions **166**

Identifying Genetic Modifiers in NPC Affecting Lifespan 167

Neonatal Lethality in *Npc1*^{em1Pav}: a new NPC mouse model of pre/perinatal onset 170

Relevance 170

References **172**

List of figures:

1.1 The lysosome as a complex organelle ……..... 21

1.2 Genetic variants of NPC1 and NPC2 ……..... 23

1.3 *NPC1* mutations are present in many different protein domains 24

1.4 Proposed mechanism of NPC1 and NPC2 in cholesterol transport within the lysosome 26

1.5 Clinical heterogeneity in NPC ……..... 29

1.6 Location of NPC1 mutations in current mouse models 37

2.1 Targeting *Npc1* with CRISPR/Cas9 ……..... 41

2.2 DNA capillary electrophoresis results 45

2.3 Sanger sequencing results from $Npc1^{em1Pav}$ 49

2.4 $Npc1^{em1Pav}$ mutation results in a deletion of 3 amino acids in NPC1 50

2.5 Sequence homology of NPC1 protein across species 51

2.6 Location of the $Npc1^{em1Pav}$ mutation compared to other *Npc1* mouse models 53

3.1 $Npc1^{em1Pav}$ mutants have significantly reduced levels of NPC1 protein 64

3.2 RT-qPCR analysis of *Npc1* mRNA normalized to *Gapdh* 66

3.3 Abnormal lipid profiles in $Npc1^{em1Pav}$ 68

3.4 Histological analysis of liver tissue from $Npc1^{em1Pav}$ 70

3.5 Histological analysis of spleen tissue from $Npc1^{em1Pav}$ 71

3.6 Purkinje cell loss in $Npc1^{em1Pav}$ mutants 72

3.7 Survival analysis of $Npc1^{em1Pav/em1Pav}$ 74

3.8 Progressive weight loss in $Npc1^{em1Pav/em1Pav}$ separated by gender 75

3.9 Neurodegenerative and behavioral phenotypes in $Npc1^{em1Pav/em1Pav}$ 77

4.1 Positive correlation between two end-point criteria in *Npc1*$^{em1Pav/em1Pav}$ 88

4.2 Protocol for marker-assisted selection (Speed congenics) 90

4.3 Marker-assisted selection results from *Npc1*^{em1Pav} heterozygous males (N3) 91

4.4 Marker-assisted selection results from *Npc1*^{em1Pav} heterozygous males (N4) 92

4.5 Strain-specific lifespan differences in *Npc1*^{em1Pav} mutants 93

4.6 Breeding strategy for mapping genetic modifiers of NPC 95

4.7 The mean lifespan of N2 backcross homozygote mice falls between that of homozygotes on a C57BL/6J or BALB/cJ background..... 96

4.8 Distribution of lifespan in *Npc1*^{em1Pav} mutants 97

4.9 Lifespan of N2 backcross generation between C57BL/6J and C57BL/6N 99

4.10 Genetic linkage results between lifespan of *Npc1*^{em1Pav} mutants and strain specific-markers for C57BL/6J and BALB/cJ 102

4.11 Effects and interactions between QTLs (Chromosome 1 & 7) 103

4.12 An additional QTL on chromosome 17 104

4.13 Workflow for genetic variant analysis for both QTLs (chromosome 1 & 7) 106

4.14 Candidate genes from damaging/deleterious genetic variants located on chromosome 1 111

4.15 Candidate genes from damaging/deleterious genetic variants located on chromosome 7 116

4.16 Visceral pathology in *Npc1*^{em1Pav} mutants varies with genetic background 118

5.1 Gross anatomy of *Npc1*^{em1Pav} embryos 134

5.2 *Npc1*^{em1Pav} embryonic development (E14.5) 135

5.3 *Npc1* ^{em1Pav} embryonic development (E16.5) 136

5.4 Growth restriction during embryogenesis in *Npc1*^{em1Pav} mutants 137

5.5 Timeline for Cesarean deliveries and maternal fostering of *Npc1*^{em1Pav} 140

5.6 Neonatal lethality in *Npc1*$^{em1Pav/em1Pav}$ 142

5.7 Low birth weight in *Npc1*^{em1Pav} mutants 143

5.8 Cross-sectional examination of thoracic cavity from *Npc1*^{em1Pav} 144

5.9 Skeletal preparation of *Npc1*^{em1Pav} mutants at birth 145

5.10 Normalized weight of lung and heart in *Npc1*^{em1Pav} mutants 146

5.11 Alveolar lipidosis in *Npc1*^{em1Pav} newborn mutants 147

5.12 Abnormal intra-alveolar surfactant accumulation in *Npc1*^{em1Pav} newborn mutants 148

5.13 Enlarged alveolar macrophages are present in in *Npc1*^{em1Pav} newborn mutants 149

5.14 Alveolar lipidosis in *Npc1*^{em1Pav} during embryogenesis 150

5.15 Overall survival of *Npc1*^{em1Pav} after Dexamethasone treatment *in-utero* 152

5.16 Using genetic test crosses in order to discover genetic modifiers of neonatal survival in *Npc1*^{em1Pav} 156

5.17 Genetic linkage results for neonatal lethality in *Npc1*^{em1Pav} from test crosses 159

6.1 Dissecting the genetic architecture of NPC 169

List of tables:

1.1 Summary of current *Npc1* mouse models 32

1.2 Potential off-target effects from CRISPR/Cas9 sequence 42

4.1 Summary of strain-specific genetic variants between C57BL/6J and BALB/cJ retrieved from the Mouse Genomes Project (Sanger) 107

4.2 List of candidate variants from QTL on chromosome 1 (PROVEAN score) 108

4.3 List of candidate variants from QTL on chromosome 1 (SIFT score) 109-110

.

4.4 List of candidate variants from QTL on chromosome 7 (PROVEAN score) 112-113

4.5 List of candidate variants from QTL on chromosome 7 (SIFT score) 114-115

5.1 Reduction of $Npc1^{em1Pav/em1Pav}$ offspring at P10 in several *Npc1* alleles 132

5.2 Normal Mendelian ratios of $Npc1^{em1Pav/em1Pav}$ offspring during embryogenesis 139

5.3 Strain-specific differences in neonatal lethality from *Npc1* mouse models 154

5.4 Variation in *Npc1* mutant survival in progeny of individual genetic test crosses 158

Abbreviations:

LSD	Lysosomal Storage Disorders
NPC	Niemann-Pick Type C Disease
CNS	Central Nervous System
HMG-CoA	3-hydroxy-3-methylglutaryl coenzyme A
SREBP	Sterol Regulatory Element Binding Protein
PTC	Patched
LDL	Low-density Lipoprotein
VSGP	Supranuclear Gaze Palsy
GSL	Glycosphingolipid
HPβCD	2-hydroxypropyl-β-cyclodextrin
ENU	N-ethyl-N-nitrosourea
EM	Electron Microscopy
T2C	Type 2 cells (pneumocytes)

Chapter I: General Introduction

Lysosomal Storage Diseases

Lysosomal storage diseases (LSDs) include more than 70 different inherited metabolic disorders characterized by extensive accumulation of the undigested metabolites in the lysosome (Fig. 1.1). Collectively, LSDs present a complex clinical picture affecting multiple organ systems with extremely variable phenotypes [1,2]. The majority of these disorders are considered monogenic with a recessive inheritance pattern [1]. Symptomatic patients present with peripheral symptoms due to organomegaly as well as neurodegeneration affecting the central nervous system [3]. While each individual disorder is usually considered a rare disease, as a group the incidence rate for LSDs is much more prevalent, with 1 affected individual for every 5000 live births [4]. During the past few years, potential treatment approaches such as improved gene therapy methods and genome editing have offered new hope for desperately needed interventions in these devastating disorders [5-7]. As part of this introductory chapter, we will briefly describe the epidemiology, genetics, molecular etiology, clinical presentation and current animal models for one of these LSDs: Niemann-Pick Type C Disease (NPC).

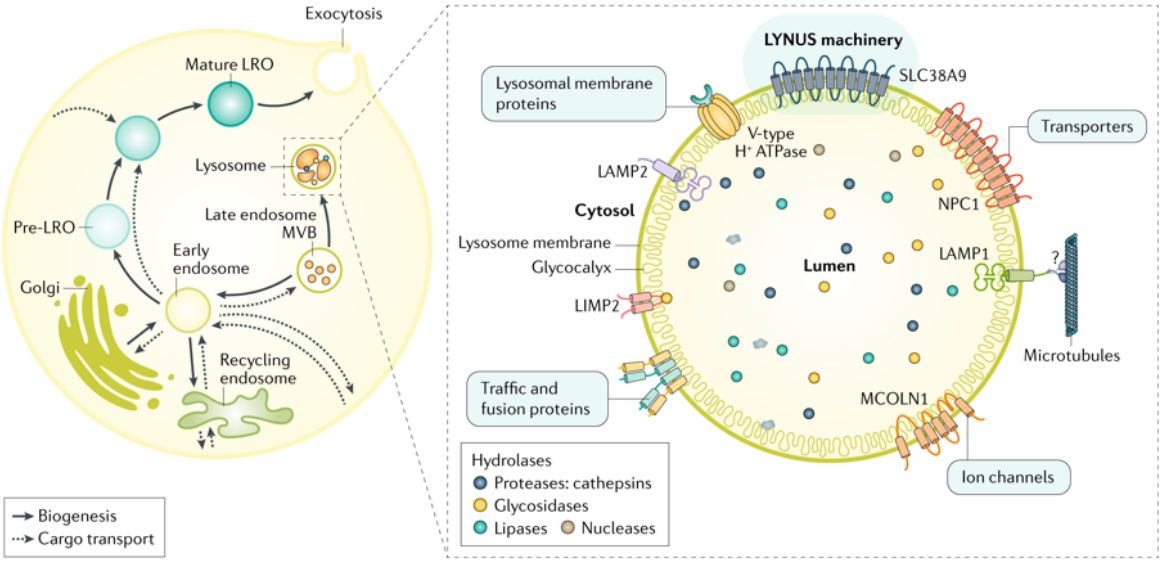


Figure 1.1 The lysosome as a complex organelle. As depicted in this figure the lysosome is a major cellular hub for trafficking and recycling. In LSDs, these processes become dysfunctional leading to the classical "storage-pathology" seen in multiple organ systems of affected individuals. Figure from Platt *et., al* 2018.[1].

Niemann-Pick Type C Disease

In 1914, the German pediatrician Albert Niemann (1880-1921) described a case of a young child of Ashkenazi Jewish descent with visceral enlargement, lymphadenopathy and neurological impairment who died at 1.5 years old. [8]. A few years later, a pathologist named Ludwig Pick analyzed *post-mortem* tissues from patients suffering from the same clinical presentation and concluded that this was a novel disease rather than a variant of Gaucher Disease as previously proposed by Dr. Niemann.[9] Today, Niemann-Pick Disease encompasses a spectrum of three different disorders. Niemann-Pick Type A has a pronounced neurological severity and Type B is a variant of Type A without CNS involvement. Both Type A and Type B are caused by mutations in the SMPD1 gene [10]. In Niemann-Pick Type C (NPC), the primary defect is in the lysosomal cholesterol transport proteins NPC1 or NPC2. While Nieman-Pick Type A, B, and C are categorized as different disorders, patients from all three usually present with similarities in lipid accumulation and visceral pathology with or without CNS involvement [3].

Epidemiology and Genetics

NPC is a rare lysosomal storage disorder affecting approximately 1 in 120,000 to 150,000 live births with a higher incidence in patients of Ashkenazi Jewish descent [11]. NPC has an autosomal recessive inheritance pattern [1]. Most of the causative mutations (95%) have been identified in the NPC1 gene (18q11- q12, OMIM: 257220), while the remainder (5%) are located in the NPC2 gene (14q24.3, OMIM:607625) [11-13]. At least 486 disease-causing variants haven been identified for NPC1 and 27 for NPC2 to date (www.hgmd.org, accessed April 25th, 2019) (Fig. 1.2). The majority of these mutations are categorized as missense/nonsense for both NPC1 (66%) and NPC2 (70%). For *NPC1*, the three most frequent alleles are I1061T, P1007A and G992W [11,14,15] (Fig. 1.3).

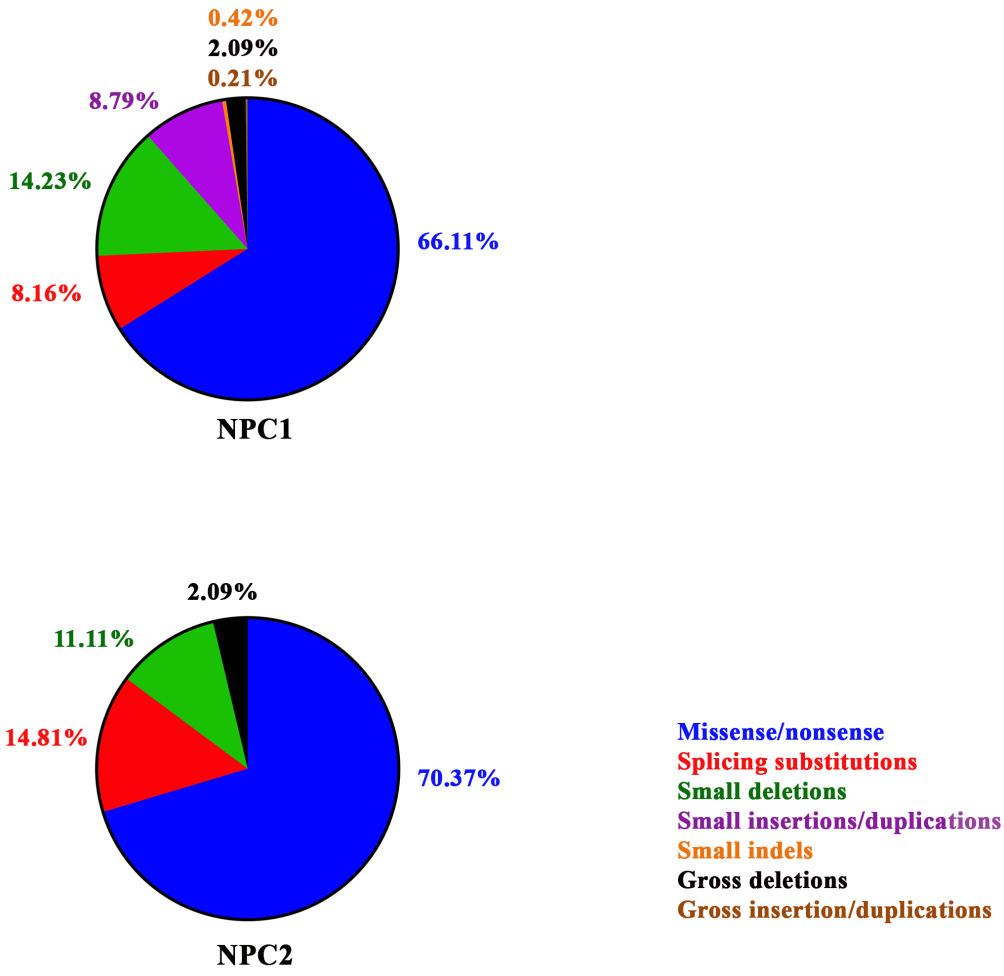


Figure 1.2 Genetic variants identified for both NPC1 and NPC2. Classification and percentage of the total genetic variants per gene are depicted by the pie charts. The majority of the mutations for both NPC1 and NPC2 are missense/nonsense (blue). Total number of disease-causing mutations: NPC1=461, NPC2=23, Likely-disease variants: NPC1=23, NPC2=4. Disease-associated polymorphisms: NPC1=2, NPC2=0. This figure was generated with genetic variant information obtained from HGMD Professional 2018.4 (Qiagen), accessed April 25th, 2019. [16].

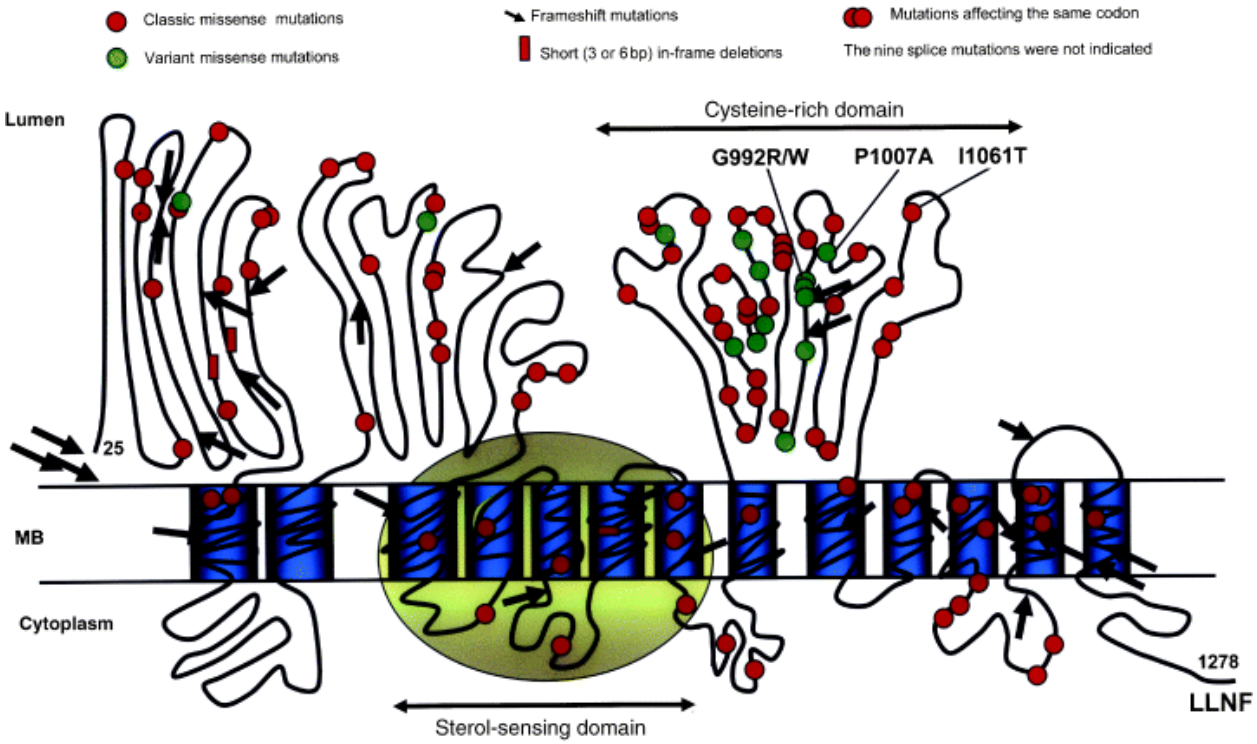


Figure 1.3 *NPC1* mutations are present in many different protein domains. NPC1 topology with representation of mutations associated with NPC1 disease. As depicted by the figure, these mutations are not localized to a specific domain of the protein. The three most prevalent identified alleles (G992R/W, P1007A, I1061T) are located in the cysteine-rich loop domain of the protein. Figure from Vanier *et al.,* 2003.[11].

Molecular Etiology

Both NPC1 and NPC2 genes encode lysosomal proteins known to participate in cholesterol transport and trafficking [17]. NPC1 is a highly conserved transmembrane protein comprised of 1278 amino acids, 13 transmembrane helices and 3 luminal domains {Lu:2015wq} (Fig. 1.3). The sterol-sensing-domain (a.a. 616-791) has been shown to have sequence homology to other sterol sensing proteins such as 3-hydroxy-3-methylglutaryl coenzyme A (HMG-CoA) reductase, SREBP cleavage-activating protein (SCAP) and the Hedgehog signaling protein receptor Patched (PTC) [12,18]. The cysteine-rich loop domain (a.a. 855-1098) harbors more than one third of the identified mutations and contains a ring-finger motif potentially participating in protein-protein interactions [18]. Recent crystal structures and biochemical studies have proposed that NPC1 and NPC2 bind to cholesterol in opposite orientations, leading to a working model of these two proteins [17,19].

NPC2, is soluble protein which binds to cholesterol from LDL and transfers it to the N-terminal domain of NPC1 (a.a. 25-264) for subsequent trafficking out of the lysosome. Loss of function mutations in either NPC1 or NPC2 will result in accumulation unesterified cholesterol, sphingomyelin and other lipids within the late endosome/lysosome [17,19,20] (Fig. 1.4). Accumulation of these metabolites leads to neurodegeneration by mechanisms that are still largely unknown.

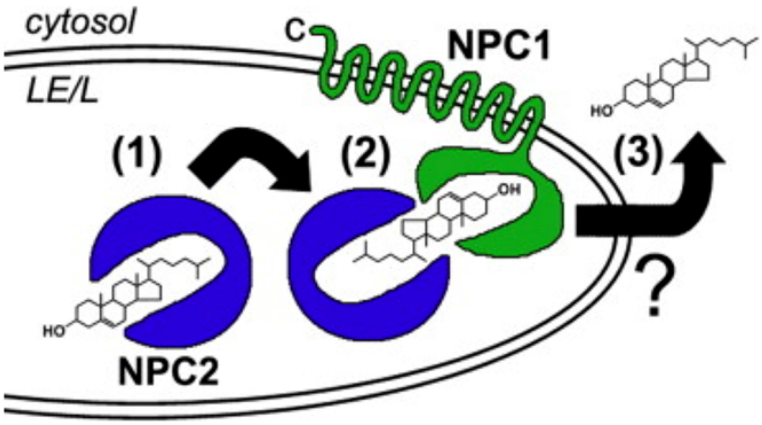


Figure 1.4. Proposed mechanism of NPC1 and NPC2 in cholesterol transport within the lysosome. Cholesterol binds to NPC2, a soluble lysosomal protein. NPC2 transfers the cholesterol to NPC1 via its N-terminal domain. Subsequently, NPC1 (transmembrane protein) transfers the cholesterol out of the lysosome by an unknown mechanism. Mutations leading to loss of function in either NPC1 or NPC2 results in the abnormal storage phenotype seen in NPC. Figure from Peake *et al*., 2010 [19].

Clinical Manifestations of NPC

In general, NPC is considered a neurovisceral disease affecting mainly the liver and the spleen as well as parts of the CNS such as the cerebellum [11,21,22]. The age of disease onset varies from *in-utero* to well into adulthood [11,21] (Fig. 1.5). Most of the clinical manifestations seen in patients are not specific to NPC, which makes it more difficult to diagnose [23]. Several categories have been defined depending on the age of onset which are described in the following sections.

Pre/perinatal Onset

NPC patients suffering from pre/perinatal onset (<3months old) [21] display a visceral presentation with hepatomegaly and/or splenomegaly, along with fetal ascites or hydrops which can be detected during gestation by ultrasound [24]. Hematological findings have also been reported with congenital thrombocytopenia accompanied by a petechial rash [24,25]. This could due in part to splenomegaly, although inherent-platelet defects have been linked to NPC1 dysfunction as well [25]. The presence of jaundice is another common indication of hepatic dysfunction as a result of cholestatic disease. A portion (8-9%) of neonatal patients succumb to the disease due to liver failure within a few weeks after birth [26,27]. For another subgroup of patients these symptoms can subside after a few months, these individuals only retain isolated splenomegaly and/or hepatomegaly until neurological symptoms appear at a later age [26]. More recently, others have shown that pulmonary complications are more common in NPC1 patients than was previously reported [28,29]. Typically, NPC2 patients have been shown to develop more respiratory complications when compared to NPC1 [30].

Infantile and Juvenile Onset

Neurological symptoms typically tend to appear in later onset patients starting during early infancy (2-3 months-2 years old) as patients present with hypotonia and motor delay [21,27]. During the late infantile period (2-6 years old) the neurological signs tend to relate to cerebellar neurodegeneration such as gait disturbance and cerebellar ataxia accompanied by fine-motor skills impairment [27]. These symptoms are also present during juvenile onset (6 to 15 years old) and are coincident with more cognitive symptoms resulting in learning difficulties at school. In general, these symptoms do not occur in an isolated and age-defined manner but as a continuum with a subtle onset (Fig. 1.5) Other neurological manifestations at these ages include supranuclear gaze palsy (VSGP), dysphagia, epileptic seizures and cataplexy [21].

Adult Onset

In addition to the previously described neurological manifestations, adult onset NPC patients (older than 15 years old) present with a higher incidence of psychiatric manifestations [31]. For example, patients can present with symptoms of auditory and visual hallucinations leading to the diagnosis of schizophrenia [32]. Other diagnoses include bipolar disorder and depressive syndrome [31]. As these psychiatric symptoms are common in the general population, diagnosis of NPC is even more difficult at this age [33].

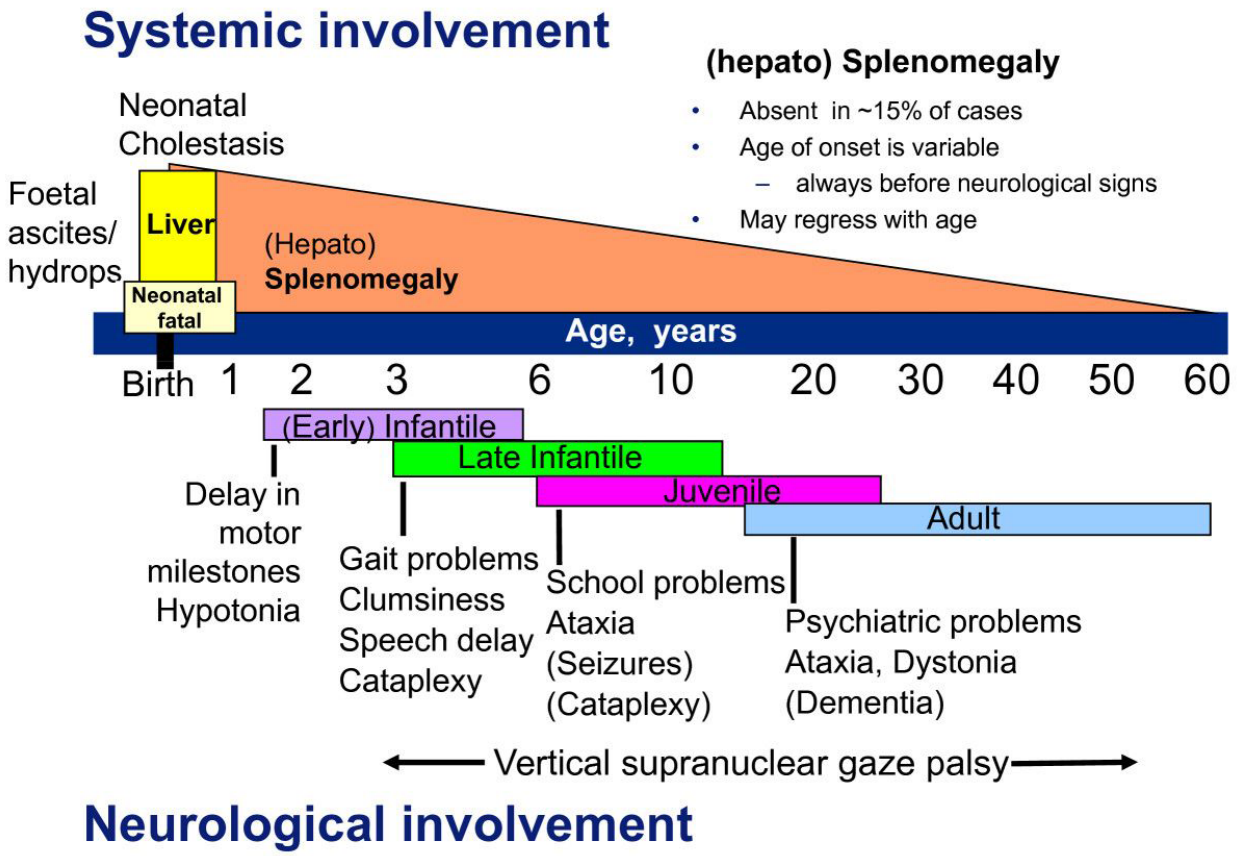


Figure 1.5 Clinical heterogeneity of NPC. Diagram shows classification based on age of onset. Starting *in-utero* a group of NPC patients is predominantly affected by visceral symptoms while later onset groups are defined by neurological symptoms. Adult-onset patients are known to have a higher risk for developing psychiatric symptoms similar to other disorders including schizophrenia and depression. The onset of symptoms does not occur in a rigidly age-defined manner but as continuum. Figure from Vanier *et al*., 2010. [14].

Current Treatments

Currently miglustat (Zavesca) is the only approved treatment for NPC in most countries worldwide. Although, The FDA has approved its use for Gaucher disease it remains being used as off-label for NPC [34]. Miglustat is able to cross the blood-brain-barrier and has been shown to be an inhibitor of glucosylceramide synthase, which catalyzes the first step in glycosphingolipid (GSL) synthesis [35]. As previously mentioned, loss of function mutations in either NPC1 or NPC2 leads to accumulation of GSLs and sphingoid bases within the lysosome [36] leading to impaired calcium-dependent endocytic function [37]. These results suggest sphingolipid accumulation effects are not only a consequence of impaired NPC1/NPC2 function, but directly contribute to lysosomal dysfunction as part of the disease etiology itself [36]. Long-term substrate reduction therapy has been conducted using miglustat in NPC patients [38]. Treatment has been shown to correct several known disease markers and to result in improvement of clinical severity particularly in neurological symptoms [39]. While these results suggest miglustat has an effect in ameliorating some of the neurodegeneration that occurs in NPC patients, it only slows progression of the disease [34].

Investigational Therapies

2-hydroxypropyl-β-cyclodextrin (HPβCD) has been shown to slow disease progression and improve survival in preclinical studies [40,41]. Phase I/IIa trials have provided promising results [42] and subsequent trials are currently being tested (NCT02534844). Other therapies such as heat-shock protein modulating treatment [43] are also currently being pursued (NCT02612129). Additionally, the generation of new viral-mediated serotypes has resulted in more selective and efficient gene therapies for many monogenic disorders [44] and pre-clinical studies with NPC animal models have shown very promising results [45,46].

Animal Models of Niemann-Pick Disease Type C1

As previously mentioned, several clinical trials of multiple treatment approaches for NPC are currently being performed [1]. In general, these human trials are based on results derived from preclinical studies using animal models [47]. One can argue that model organisms play an even more vital role in NPC based on several factors. First, as a rare disease, sample size is greatly reduced and often considered a limiting factor in clinical trial design [48]. Second, due to the genetic and clinical heterogeneity seen in NPC, several animal models are needed to reproduce these differences [49]. For example, assessment of targeted treatments is usually tailored to specific types of mutations [43,50]. Thus, model organisms that are able to recapitulate both the heterogeneity and hallmarks of the disease can greatly improve the diagnostic assays and drug discovery that are desperately needed for this fatal disorder.

There are currently many NPC model organisms [49]. These include: *Saccharomyces cerevisiae* (yeast) [51,52], *C. elegans* (nematode) [53], *Drosophila melanogaster* (fly) [54], *Danio rerio* (zebrafish) [55], *Felis catus* (cat) [56], *Canis lupus familiaris* (dog) [57] and the most widely used *Mus musculus* (house mouse) [58-63]. In this section we will briefly review different *Npc1* mouse models that are currently available (Table 1.1).

Table 1.1 Summary of current *Npc1* mouse models

***Npc1* allele**	**Original strain**	**Mutation**	**Reported survival (weeks)**	**Comparable age of onset in NPC patients**
Npc1^{spm}[60]	C57BL/KsJ	Spontaneous 43bp insertion resulted in null allele	12-14 weeks	Infantile onset (severe)
Npc1^{m1N} or *Npc1*^{nih} [61]	NCTR-BALB/c	Spontaneous 824 base pair insertion resulted in null allele	11.4-17.1 weeks	Infantile onset (severe)
Npc1^{tm1Mbjg} or *Npc1*^{pf} [63]	C57BL/6 and 129Sv/Ev	Targeted-knock in with two point mutations (P202A/F203A) resulting in increased NPC1 protein.	7 weeks (average)	Infantile onset (severe)
Npc1^{nmf164} [59]	C57BL/6J	ENU-generated point mutation (D1005G) resulted in hypomorphic allele	15 weeks (average)	Juvenile (less severe)
Npc1$^{tm1.1Dso}$ or *Npc1*^{I1061T} [62]	C57BL/6J	Targeted knock-in with I1061T mutation resulted in hypomorphic allele	17.8 weeks (average)	Juvenile (less severe)
Npc1^{imagine} [64]	C57BL/6J	Targeted knock-in (c.1554-1009 G>A within intron 9) caused abnormal splicing resulting in a pseudoexon.	9 weeks (average)	Infantile (severe)
Npc1^{pioneer} [64]	C57BL/6J	Targeted knock-in (His641Thrfs*2)	Not reported[a]	-
Npc1^{flox} [58]	C57BL/6J	Two *lox*P sites were inserted flanking exon 9.	-	-

[a] Only double heterozygous mice (*Npc1*$^{imagine/pioneer}$) were reported with a survival of 9 weeks.

Mouse Models

Models of infantile onset:

Npc1^{m1N} or *Npc1^{nih}*

In 1980, Pentchev and colleagues described a new mouse model arising from a spontaneous mutation from the National Center for Toxicology Research, USA in 1975 [61]. The affected mice were characterized by accumulation of unesterified cholesterol and sphingolipids including gangliosides such as GM2 and GM3 in the brain which replicated features of both NPC and Gaucher disease. Further analysis of this mouse model several years later, showed the phenotype was associated with an 824 base-pair insertion of a retrotransposon-like sequence in exon 9 of the *Npc1* gene introducing a premature stop codon and thus resulting in a null allele (Fig. 1.6) [12]. Subsequent studies were able to show that mice homozygous for this *Npc1^{m1N}* allele (also widely known as *Npc1^{nih}*) served as a reliable model for NPC [61,65,66]. Currently, *Npc1^{m1N}* is the most commonly used mouse model in the NPC field [49].

Npc1^{spm}

In 1975, a spontaneous mutant derived from a breeding between littermates developed behavioral symptoms such as motor incoordination and tremor [60]. Over 20 years later, analysis of the responsible mutation revealed a 43 base-pair insertion resulting in a frameshift and a premature stop-codon (Fig. 1.6) [59]. *Npc1^{spm}* mutants showed a decreased lifespan and progressive weight loss. A detailed pathology work-up revealed hepatosplenomegaly and enlarged lymph nodes in the mutants. The presence of foam cells clusters was described in both the liver and the spleen. Purkinje cell loss was also described in the cerebellum. No gender differences were reported. These results in *Npc1^{spm}* mutants were the first ones describing NPC-related pathology in a mouse model.

Npc1^{tm1Mbjg} or *Npc1*^{pf}

This NPC mouse model was generated by knocking in two amino acid substitutions into the N-terminal domain (c.604>G; c.607-608TT>GC, P202A/F203A) (Fig 1.6). Protein quantification showed higher mRNA levels of NPC1 resulting in higher protein expression compared to control littermates. Interestingly, *Npc1*^{pf} mutant mice showed similar disease severity as the previously mentioned null alleles. These results validated the cholesterol binding properties of the N-terminal domain as essential for proper NPC1 function [63].

Models of juvenile onset:

Npc1^{nmf164}

The *Npc1*^{nmf164} allele was generated by chemically-induced (ENU) mutagenesis resulting in a point mutation (c.3163A>G; D1005G) (Fig. 1.6) [59]. This was the first hypomorphic allele described, and it mimicked a later onset and thus less severe disease phenotype. Although the altered amino acid is conserved in humans, this mutation has not been described in NPC patients. The mutation is also located in the cysteine rich domain of the protein, which is essential for protein function.

Npc1$^{tm1.1Dso}$ or *Npc1*^{I1061T}

I1061T has been described as the most common mutation in NPC patients [11,14,15]. This mouse model was generated using a knock-in construct of the I1061T mutation (c.3179T>C) located in exon 21 (Fig. 1.6). Two *loxP* sites were also inserted, which could be useful for generating tissue-specific NPC1 deletion [62]. *Npc1*^{I1061T} mutant mice show a milder disease

severity and longer lifespan compared to the null allele (*Npc1*^{nih}). Protein quantification analysis showed reduced amount of protein compared to control littermates due to misfolding and decreased stability of the NPC1 protein. This process was also shown to be regulated by ER-associated degradation [67].

Other alleles:

***Npc1*^{imagine} and *Npc1*^{pioneer}**

The *Npc1*^{imagine} allele has a mutation located in intron 9 (c.1554-1009 G>A) this generates an alternative donor splice site resulting into a pseudoexon and a frameshift thus making it a feasible model for splicing-specific treatments such as anti-sense oligonucleotides [50]. The second allele *Npc1*^{pioneer}, harbors a mutation in exon 12 (c.1920delG) which results in a frameshift located in the SSD domain. This mutations has also been characterized in NPC1 patients [68]. Although the description of these two alleles is very limited, *Npc1*^{imagine} mutants displayed expected pathology seen in other *Npc1* mouse models such as foam cells in the liver and Purkinje cell death in the cerebellum. This was also accompanied by motor impairment associated with NPC1 deficiency. In the case of the *Npc1*^{pioneer}, due to a low birth rate of homozygous mutant offspring (2% compared to the expected 25%) the authors were able to only describe compound heterozygous mice (*Npc1*$^{imagine/pioneer}$). Thus, characterization of *Npc1*^{pioneer} mutants is still limited [64].

***Npc1*$^{tm1.1Dso}$** or ***Npc1*^{flox}**

This allele was generated in order to study NPC1 loss of function in a tissue/cell-specific manner, particularly in Purkinje cells [58]. First, the *Npc1*^{flox} allele was designed by placing two

*lox*P sites flanking exon 9. Mice positive for Cre-mediated recombination under specific Purkinje cell deletion (*Pcp2-Cre*) displayed motor impairment phenotypes previously described in *Npc1* alleles. Interestingly, these mutants did not experience weight loss and had no change in survival compared to controls. These results suggested Purkinje cell loss is mainly responsible for the classical cerebellar ataxia seen in *Npc1* mice, but they are not the main cause of early mortality. The authors also showed Purkinje cell loss due to NPC1 dysfunction occurs in an autonomous manner and in an anterior-to-posterior gradient.

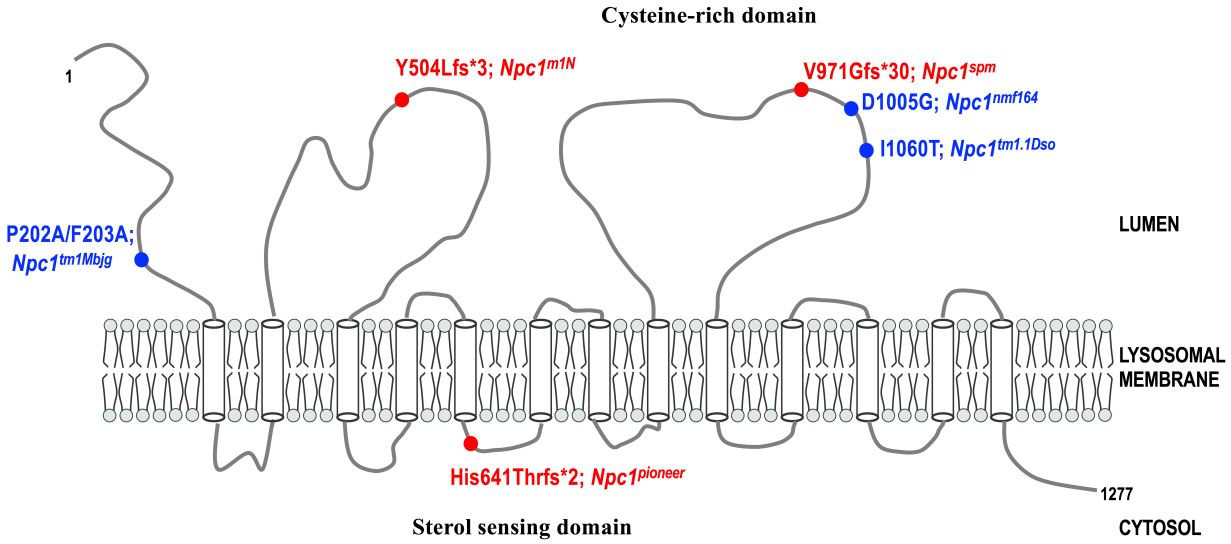


Figure 1.6 Location of NPC1 mutations in current mouse models. Topology drawing of NPC1 depicts the mutation positions for each mouse model. Point mutations are represented in blue. Deletions or insertions resulting in premature truncations are represented in red. Only mutations located in coding regions are included.

Genetic modifiers in NPC

With new advances in sequencing technology many genes responsible for Mendelian disorders have been identified [69]. Further analysis of these mutations has revealed that even when accounting for their causative effect, phenotypic variation still exists [70,71]. As a consequence, the term "monogenic disorder" has been questioned for many of these disorders. Environmental exposure and/or epigenetic changes are potential causes for this effect [72,73]. However, phenotypic differences between affected individuals with the same disease-causing mutations could also be explained by the presence of genetic modifiers [74]. NPC has been shown to be extremely heterogenous in terms of clinical presentation as well as time of onset [14]. Other studies have shown these phenotypic differences are still present even between patients with the same *NPC1* mutation [75-77]. This phenomenon of phenotypic severity being altered by genetic background is also evident when analyzing *Npc1* mouse models in different inbred strain backgrounds. For example, differences in severity [78], onset [79], survival [62,80] and treatment response [81] have all been reported. These results suggest the presence of genetic variants capable of modifying the NPC phenotype. Identification of these genetic modifiers will not only aid the diagnosis of NPC but will also give us the potential to find novel targets for treatment.

During the next few chapters we will describe our efforts to address the genetic architecture of NPC1 disease. To do this, we relied on *Npc1* mouse models to further characterize the disease and identify underlying genetic components affecting its severity and progression.

Chapter II: Generation of *Npc1*^{em1Pav}

Introduction

As mentioned in the previous chapter, Niemann-Pick Disease Type C (NPC) is a rare and fatal neurodegenerative disorder. NPC is highly heterogenous in terms of age of onset and clinical presentation including hepatosplenomegaly *in-utero*, liver failure in neonates and neurodegeneration in juvenile and adult forms [14]. Over 400 human mutations have been identified for NPC. Most of them occur in the NPC1 gene (95%) while the remainder are located in NPC2 (5%) (Fig. 1.2). These mutations are not clustered within specific protein domains and show little concordance with clinical severity and/or disease onset [14,76]. In order to study and recapitulate the heterogeneity and hallmarks of this disease, several *Npc1* mouse models have been created (Table 1.1). While these models have been useful in studying this disease, [59,61,62] they are unable to recapitulate all level of disease-severities as well as types of mutations seen in NPC patients. For example, there are currently no models for pre/perinatal onset [49]. Furthermore, while two mouse models harboring missense mutations have been generated [59,62], there are currently no characterized models with small deletions, the second most common type of mutations in NPC1 patients (Fig 1.2). As different treatments and biomarkers are being tested for NPC having different models representing the genotypic heterogeneity seen this patient population has also become essential [49].

With the help of new advances in genome editing such as the CRISPR/Cas9 system, we generated a new NPC mouse model in the commonly used mouse strain C57BL/6J. In this chapter, we will describe the generation of this new allele: *Npc1*^{em1Pav}.

Materials and Methods

CRISPR/Cas 9 Design:

Npc1 was targeted within exon 21 (Fig. 2.1) at the site of a commonly occurring human mutation, I1061T, using a 20bp CRISPR/Cas9 target sequence (GCTAATAGCCAGTAACATCA) selected with publicly available software tools (Benchling.com).

Off-target Effects:

Potential off-target regions were analyzed based on the target sequence. No off-target sites were detected linked to *Npc1* on chromosome 18. Other regions showed mismatch sequences with a low score (Table 2.1).

Synthesis of gRNA:

Oligonucleotides with a linked T7 site and Cas9 scaffold sequence were synthesized, annealed, and filled in to generate a double stranded template for gRNA synthesis using the MEGAshortscript T7 Kit (Thermo Fisher Scientific). Guide RNA was subsequently purified with the MEGAclear Transcription Clean-Up Kit (Thermo Fisher Scientific) according to manufacturer's instructions. RNA quality was assessed with a Bioanalyzer instrument (Agilent Genomics) and stored in aliquots at -80 until used for injections.

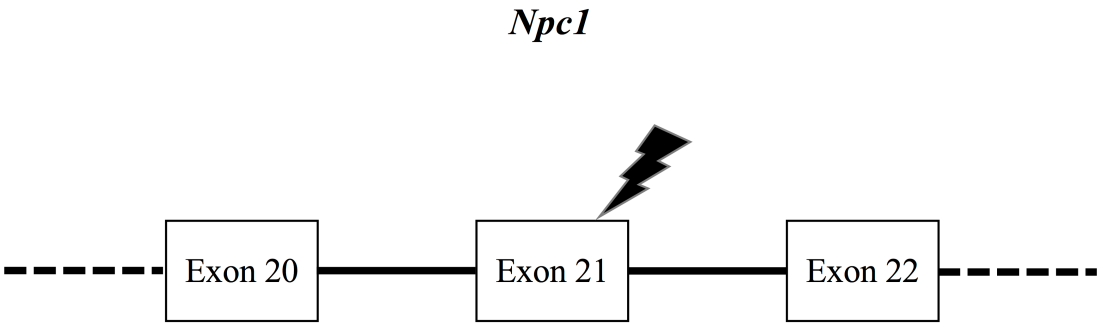


Figure 2.1 Targeting *Npc1* with CRISPR/Cas9. Schematic representation of *Npc1* targeted location (exon 21) by CRISPR/Cas9. Only 3 out of 25 exons are shown.

Table 2.1 Potential off-target effects from CRISPR/Cas9 sequence

Sequence	Pam	Score	Gene	Locus
GCTAATAGCCAGTAACATCA	CGG	100	*Npc1* (ENSMUSG00000024413)	chr18:-12195061
GTTAATAGAAAGTAACATCA	AAG	1.6		chr13:-89173267
GCTTCTAGTCAGTAACATCA	AAG	1.6		chr2:+66840379
CCAAATATCTAGTAACATCA	CAG	1.5		chr9:-112090883
GCACATGACCAGTAACATCA	GGG	0.9		chr2:-57858396
TGTTATAGCCTGTAACATCA	CAG	0.9		chr13:-62601476
TGTTATAGCCTGTAACATCA	CAG	0.9		chr13:-62515053
CGTTATAGCCTGTAACATCA	CAG	0.9		chr13:-62366426
TGTTATAGCCTGTAACATCA	CAG	0.9		chr13:+62176500
TGTTATAGCCAGTAACATCA	CAG	0.9		chr13:+62053639

Original *Npc1* target along with nine additional top scoring regions that are potential locations for off-target nuclease activity. Base-pairs in red denote mismatch with the original target sequence (top). Imported from Belching.com.

Pronuclear Injection:

Pronuclear injection was performed with standard procedures [82]. Briefly, fertilized eggs were collected from super-ovulated C57BL/6J (Jackson Laboratories) females after mating with C57BL/6J males and microinjections were performed using a capillary needle with a 1–2 mm opening pulled with a Sutter P-1000 micropipette puller. A mixture of Cas9 mRNA (10ng/ul; TriLink BioTechnologies) and the synthesized gRNAs (25ng/ul) diluted in 10 mM Tris, 0.25 mM EDTA (pH 7.5) was used for pronuclear injection into the C57BL/6J x C57BL/6J zygotes. Injected eggs were surgically transferred to pseudo-pregnant CB6F1 hybrid recipient females, bred at the NIH from a cross of BALB/cJ females to C57BL/6J males. All animal procedures were performed in a pathogen-free, AAALAC- approved facility, in accordance with National Institutes of Health (NIH) guidelines and approved by the National Human Genome Research Institute (NHGRI) Animal Care and Use Committee (ACUC).

Genotype Identification:

Founders were screened using a combination of PCR and sequencing. Briefly, DNA was extracted from pup tail biopsies at Postnatal day 10 (P10) and purified using a Gentra Puregene Mouse Tail Kit (Qiagen). A PCR product spanning the gRNA target site was generated using a *Npc1*-specific forward primer with an M13-tail (5'-tgtaaac gacggccagtTGAGAGCGAAGGATCTGCAGTC), and a *Npc1*-specific reverse primer containing a pig-tail (5'-gtgtcttGGGGCCACTTACTTCATGACCT). The PCR product was amplified with the addition of a 6-FAM or HEX labeled M13-forward oligonucleotide and run on an ABI 3130xl with ROX400 or ROX500 size standards to detect small indels

at single base pair resolution by capillary electrophoresis. (Fig. 2.2). Standard agarose gels were also used to screen PCR products for larger indels

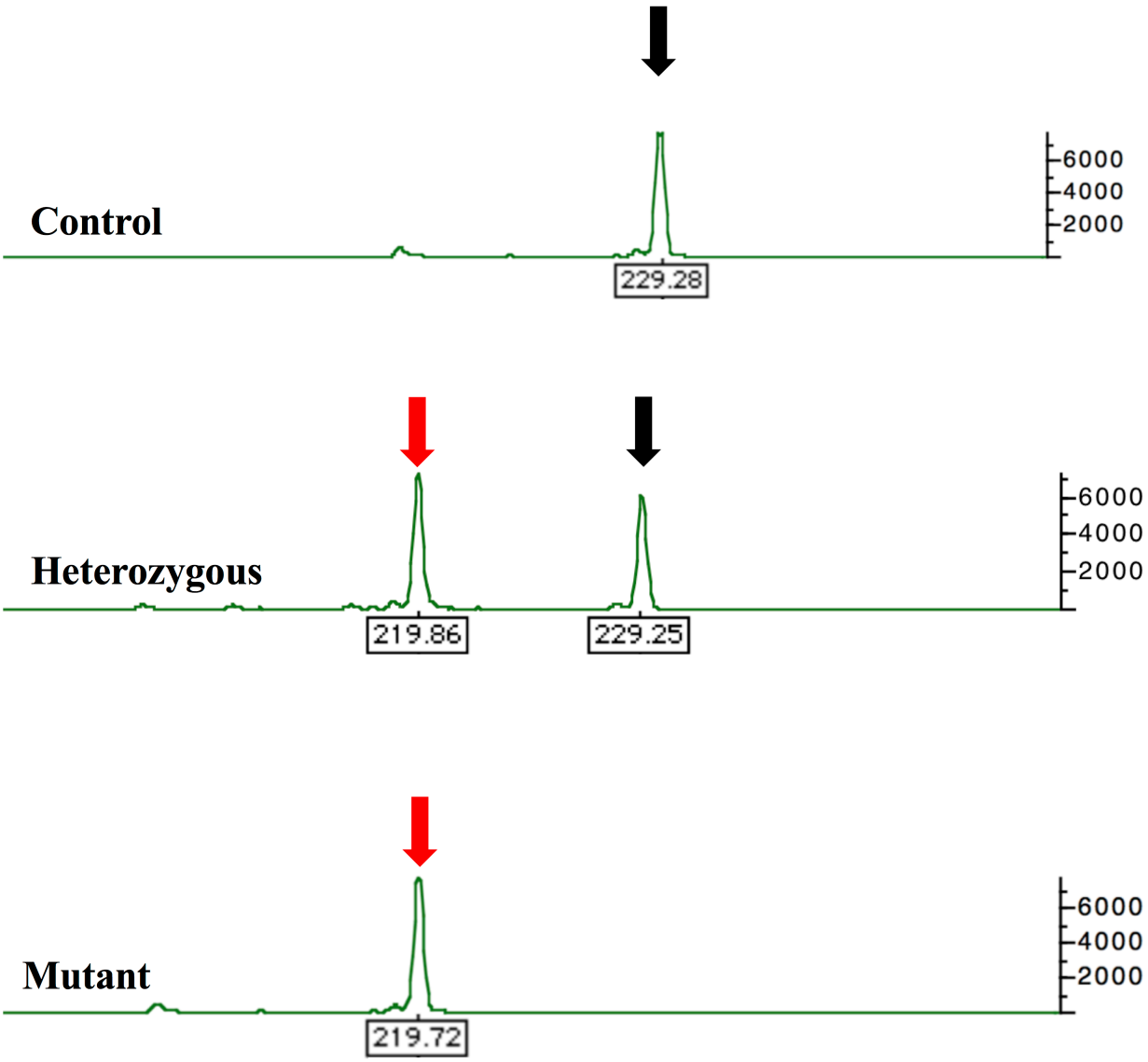


Figure 2.2 DNA capillary electrophoresis results. Black arrow indicates the control allele. Red arrow shows the mutant allele. Each peak represents the amplified DNA product and its relative size on the x-axis. The control sample shows an approximately 229bp size for both alleles while the mutant allele shows an approximately 9-10 base pair deletion. The heterozygous sample shows both alleles.

Sanger Sequencing:

The precise mutation in the founder used to establish the *Npc1*^{del} colony was further characterized by Sanger sequencing (Eurofins Genomics, USA) of PCR products generated with additional gene specific primers (F: CTCTCCTGTGACTCTCTGGG and R: AGCTGTGCATCATGTTTGGT) and confirmed in multiple offspring of the original founder.

cDNA preparation:

Brain tissues were harvested from control and mutant animals. Tissues were homogenized and transferred to Trizol (Thermo Fisher Scientific). RNA was isolated using standard protocol (Qiagen) and quantified. cDNA was synthesized from 1μg of total RNA per reaction using High-Capacity cDNA Reverse Transcription Kits (Thermo Fisher Scientific).

Colony management:

This new colony was maintained by following the standard protocol of Animal Care and Use Committee, (ACUC) from the NHGRI. A backcross to C57BL/6J (Jackson Laboratories) was used to maintain the colony and heterozygotes were mated to generate homozygote mice for analysis. We have bred more than 10 generations from the founder mutant male selected up-to-date. Genotyping was designed for gel electrophoresis with an expected amplification of 150 base-pairs, using the following primers: Forward: CACCTGTAAGGGAATACGCGG; Reverse: GGCCACTTACTTCATGACCT. Since the mutation was a small deletion, we used a high-definition agarose (NuSieve 3:1, Loza). To reduce the high costs and time spent using the traditional electrophoresis genotyping, we

designed a real-time PCR assay (Custom Taqman Assay Design Tool; Thermo Fisher Scientific) which allowed us to genotype a large group of samples with higher accuracy and efficiency. Samples were amplified with primers and probes (FAM: TTACTGGCTGTTAGCCG-MGBNFQ, VIC: ATGTTACTGGCTATTAGCCG-MGBNFQ, F: GCGGTAGTCACTCCCCTTAG, R: CCATGAAGAAAGCTCGGCTA) using a Universal 2x Taqman Master Mix (Thermo Fisher Scientific) and an ABI 7500 instrument for thermocycling and detection.

Nomenclature:

Standard nomenclature of the allele was registered as *Npc1*^{em1Pav} following the *Guidelines for Nomenclature of Genes, Genetic Markers, Alleles, and Mutations in Mouse and Rat* approved by the International Committee of Standardized Genetic Nomenclature for Mice (Mouse Genome Informatics).

Results

Targeted mutagenesis of *Npc1* with CRISPR/Cas9 results in a nine base-pair deletion:

The *Npc1*^{em1Pav} allele was identified by screening founders from CRISPR/Cas9 targeted injections. Further analysis by Sanger sequencing of the selected mutation revealed a nine base-pair deletion located in exon 21 of *Npc1* (Fig. 2.3). Sequencing results were verified by analyzing both genomic DNA and cDNA. This mutation is predicted to result in the deletion of three amino acids (S1062-I1064) (Fig. 2.4). Sequence homology analysis reveals these three amino acids are highly conserved in multiple mammalian species (Fig. 2.5). Of note, the third amino acid is not identical in human, as isoleucine is replaced by valine. However, this is a conservative substitution, since both amino acids share similar biochemical properties as they are both aliphatic with hydrophobic side-chains.

As this deletion spans nine nucleotides that fully include three amino acids (3 codons), there will be no change in the translational frame. This is also known as an in-frame deletion. Based on these changes, we predict that the *Npc1*$^{em1Pav/em1Pav}$ mice will express residual protein and thus will not be null for NPC1

.

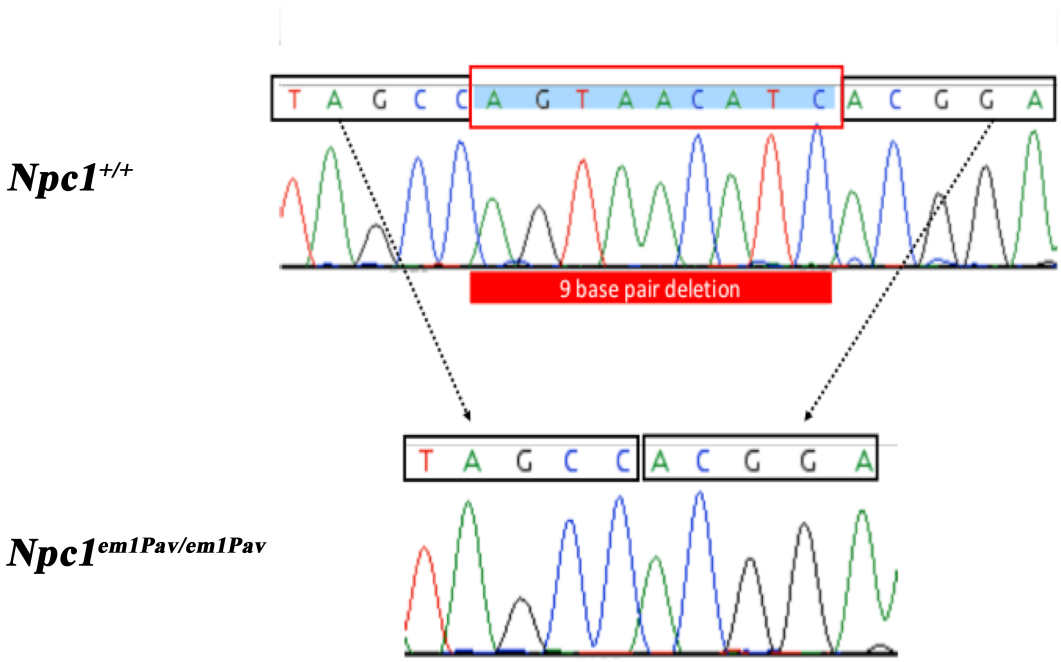


Figure 2.3 Sanger sequencing results from *Npc1*^{em1Pav}. Bottom chromatogram shows sequence from *Npc1*^{em1Pav} mutant (genomic DNA) with a nine base-pair deletion (AGTAACATC) compared to the control (*Npc1*$^{+/+}$) on top.



Figure 2.4 *Npc1*^{em1Pav} mutation results in a deletion of 3 amino acids in NPC1. Amino acid sequence of *Npc1* (mouse) showing the 3 amino acids that are predicted to be deleted as a result of the nine-base pair deletion in exon 21.

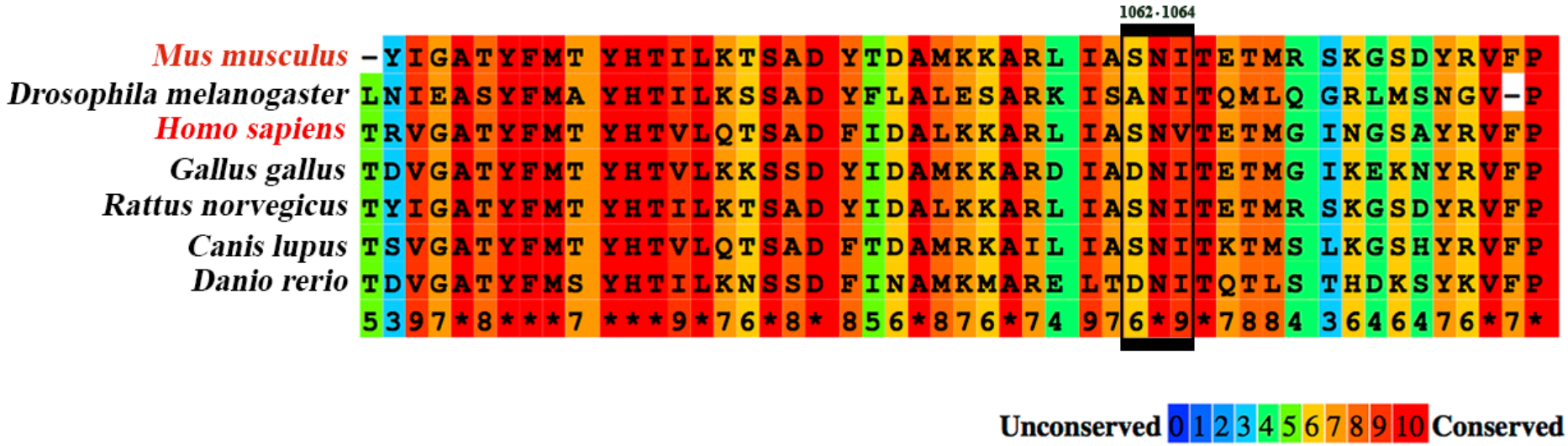


Figure 2.5 Sequence homology of NPC1 protein across species. The three amino acids deleted in *Npc1*^{em1Pav} are shown. While there is less conservation at S across species, there is identity at N, and conservative substitution for I in human. Modified from Praline analysis (Center for Integrative Bioinformatics VU, Amsterdam).

$Npc1^{em1Pav}$ harbors a mutation located in the cysteine-rich domain of NPC1:

The $Npc1^{em1Pav}$ mutation is located in the cysteine-rich domain of the protein (Fig. 1.3). As previously described in Chapter I, this domain contains more than one third of the identified human mutations for NPC1 [11]. This new deletion is also located distal to I1061T, the most common human mutation [11,14,15]. As previously shown, one of the three amino acids involved in this deletion is not conserved in humans (mouse 1062-1064 Ser-Asn-Ile; human 1063-1065 Ser-Asn-Val). Interestingly, we identified a missense mutation at this location in the Human Gene Mutation Database (HMGD) that is predicted to result in a substitution of the nonconserved valine (c.3194T>G; p.V1065G; ENST00000269228.9). In this specific case, the patient was heterozygous for this mutation and was reported with infantile onset of NPC disease [83]. This human V1065G mutation along with the well-characterized I1061T mutation suggest that the region of the protein impacted by the novel three amino acid $Npc1^{em1Pav}$ deletion is critical for NPC1 function

.

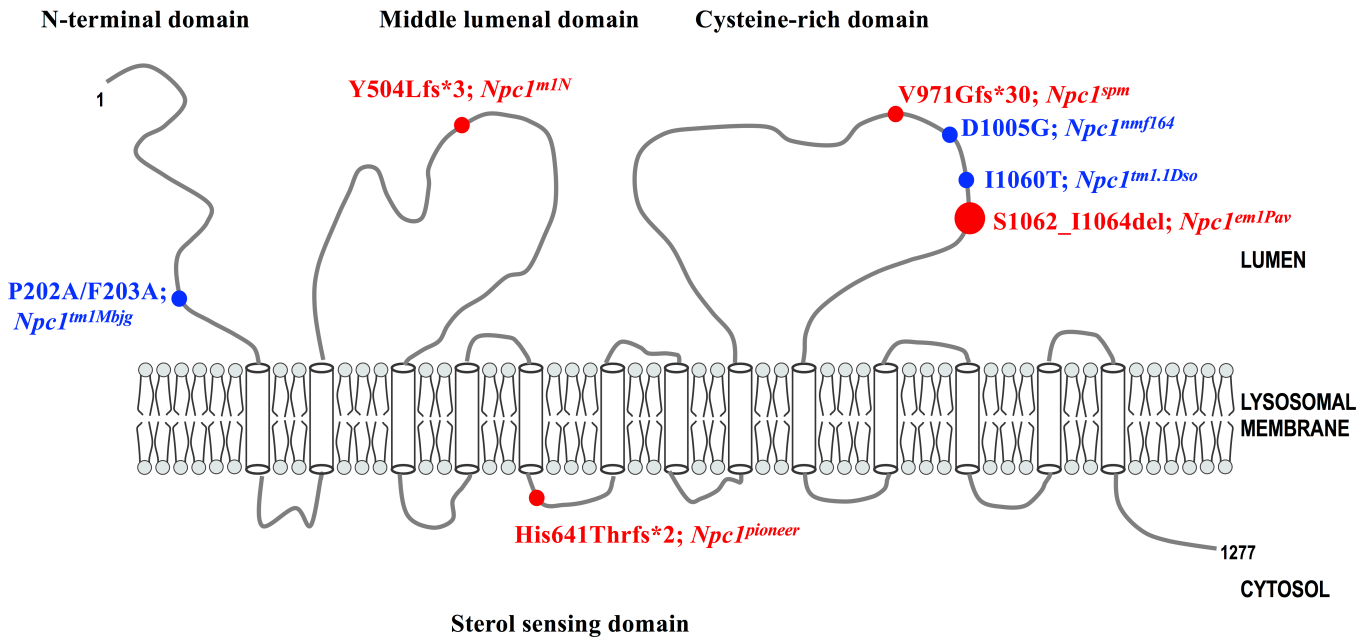


Figure 2.6 Location of the *Npc1*^{em1Pav} mutation compared to other *Npc1* mouse models.

Nine base-pair deletion for *Npc1*^{em1Pav} (large red dot) compared to the mutations of other previously published mouse models. *Npc1*^{em1Pav} is located in the cysteine-rich loop domain adjacent to the I1061T mutation. Mutations in non-coding regions are not shown. Red = alleles due to truncation and deletions; Blue = missense alleles.

Discussion

With newly developed techniques in genome editing such as the CRISPR/Cas9 system, we are now able to target regions in the genome with higher accuracy and efficiency. By taking advantage of this, we were able to create the first NPC mouse model generated with CRISPR/Cas9 targeting. We combined capillary electrophoresis and DNA sequencing in order to select non-mosaic founders. At the end of the screening process, we were able to select one male harboring a novel mutation located in exon 21 of the NPC1 protein. Based on the targeted sequence used, we do not anticipate the founder would carry any potential off-target sites on chromosome 18. The other regions which could have off-target sites showed very low probability scores and would segregate independently of *Npc1* during the multiple generations of breeding that have been completed from our male founder.

This new allele harbors a nine-base pair mutation resulting in the deletion of three amino acids (S1062-I1064). Examination of NPC1 protein sequences across species showed that one of the amino acids affected is not identical in humans (mouse I1064, human V1065). However, we consider this to be a conservative substitution as both amino acids are very similar in terms of their chemical properties. The mutation is located in the cysteine-rich loop domain of the protein and nearby to the most common *NPC1* human mutation: I1061T. We predict this in-frame deletion may result in a hypomorphic allele rather than a complete null. We hypothesize that this new allele carrying a new *Npc1* mutation will be able to recapitulate unique phenotypes associated with NPC that have yet been characterized in previous models. In order to do this, we evaluated if this new allele will display classical hallmarks of the disease. The next chapter will focus on the results from this characterization.

Summary

- We generated a new mouse model of NPC by using CRISPR/Cas9: *Npc1*^{em1Pav}.
- No potential off-target sites are predicted on chromosome 18.
- Mutation was identified as nine-base pair in-frame deletion and likely encodes a hypomorphic allele.

Chapter III: Characterization of *Npc1*^{em1Pav}

Introduction

Model systems serve as valuable tools for understanding disease processes and trialing potential treatments [84]. For most common diseases, clinical trials serve as the gold standard for diagnosis and treatment [85]. As a rare disease, NPC poses a challenge in designing clinical studies due to a small sample size and an extremely variable phenotype. Since the discovery of the first spontaneous *Npc1* mouse mutant [61], many preclinical studies have been performed in this mouse model resulting in the approved drug miglustat [86]. Currently, other potential treatments that showed benefit in NPC mice are being tested in patients [42,43]. This is partially due to the ability of *Npc1* mouse models to recapitulate the disease's natural history and phenotypes.

For example, *Npc1* mice exhibit the same classical storage-pathology seen in NPC patients. The presence of foam cells in peripheral organs such as the liver, spleen and lungs can be observed within the first 3 weeks of life [59,62,66]. They also exhibit splenomegaly and a significant accumulation of cholesterol in these organs [59,80]. In the central nervous system, *Npc1* mutants show loss of cerebellar Purkinje cells in an autonomous and temporal manner [58,87,88] as well as microglial activation [62]. Progressive weight loss accompanied by ataxia and a shorter lifespan have also been described [59,61,62]. Behavioral tests including rotarod performance, hot plate test and ledge test have been used to quantify motor impairment in these mice [62,64]. In this chapter, we will describe the characterization of a novel mouse model (*Npc1*^{em1Pav}) and how it recapitulates phenotypes previously seen in other *Npc1* alleles consistent with NPC disease.

Materials and Methods

Western Blot:

Tissue lysates were prepared by incubating them with RIPA buffer (150nM sodium chloride, 1% Triton X-100, 0.5% sodium deoxycholate, 0.1% SDS (sodium dodecyl sulfate), 50 mM Tris pH 8.0) for 2 hours at 4˚C with 10X protein inhibitor cocktail (Millipore Sigma). Samples were centrifuged for 20 minutes at 13,523 rcf on a table centrifuge (Eppendorf 5424, 24-place aerosol). Supernatant was separated and loaded with 5% BME (Sigma) and 2X Tris-Glycine SDS sample buffer (Thermo Fisher Scientific) on a 4-12 % Bis-Tris protein gel (Thermo Fisher Scientific). Protein was transferred onto a nitrocellulose membrane (Thermo Fisher Scientific) using an iBLOT dry transfer system (Thermo Fisher Scientific) with an eight-minute transfer time. Primary antibody for NPC1 (Abcam catalog# 134113) was diluted 1:1000 as well as alpha-tubulin (Millipore Sigma catalog#CP06; 1:1000) were incubated overnight at 4˚C in blocking buffer (Licor) with 0.1 TBST with Tween (Millipore Sigma catalog # T9039). Blots were washed 3 times in PBST before incubating with Secondary antibodies (1:10000, 1hr RT), imaging and protein quantification was done using the Odyssey system (Licor).

RT-qPCR (RNA):

Tissues were harvested and immediately homogenized in 1ml Trizol (Thermo Fisher Scientific Fisher). 200µL Chloroform was added, and the recovered supernatant was loaded onto a silica-membrane column for purification following the manufacturer's instructions (Qiagen RNeasy). cDNA was synthesized by using 1µg of total RNA per reaction using High-Capacity cDNA Reverse Transcription Kit (Thermo Fisher Scientific). Taqman gene expression assays were used to amplify *Npc1* (Assay ID: Mm00435300_m1) and *Gapdh* (Assay ID: Mm99999915_g1). A control cDNA was used in serial dilutions to generate a standard curve and calculate the relative

expression level of each gene. Real-time PCR reactions were performed by using StepOne machine (Applied Biosystems). Each sample was analyzed by using three technical replicates in a 96 well plate. Technical replicates were averaged, and the expression level of *Npc1* was normalized to *Gapdh*, the selected housekeeping gene.

Animal Perfusion and Tissue Harvest Protocol:

Animals were anesthetized with tribromoethanol (Avertin) 1.25 % solution, following NHGRI Animal Care and Use Committee guidelines. Perfusion was performed by making an incision on the right atrium and administering 35mls of 1X PBS followed by 35mls of 4% paraformaldehyde (Ted Pella) intravascularly via the heart. Following perfusion, tissues were harvested, fixed overnight in 4% paraformaldehyde, washed with 1X PBS and stored in 70% EtOH until processing for histology. Tissues used for GSL and Sphingosine analysis were immediately frozen in liquid nitrogen after perfusion (1X PBS) and stored in -80˚C until further processing by RP-HPLC.

Tissue Histology and Immunohistochemistry:

Tissues stored in 70% ethanol were processed for histology. Briefly, samples were dehydrated through graded alcohols, cleared in xylene, and infiltrated with paraffin. After processing, all tissues were embedded in paraffin. The paraffin blocks were cut on a microtome at 5 μm. For hematoxylin and eosin (H&E) staining, the unstained slides were deparaffinized through xylene and graded alcohols to water, stained in hematoxylin, then rinsed again in water. The slides were then placed in 95% ethanol before staining with eosin and dehydrating through graded alcohols to xylene. The stained H&E slides were then mounted with permount.

Specialized Staining:

Purkinje cells in the cerebellum: calbindin D (catalog number C9848, Sigma-Aldrich) was used at a 1:1000 dilution; mouse Ig was used as a secondary with biotin.

Macrophages in the liver and spleen: anti-CD68 (rabbit polyclonal) was used at a 1:120 dilution, mouse Ig was used as a secondary with biotin.

Microscopy:

Immunohistochemical images were collected using a Zeiss AxioScan.Z1 slide scanning microscope system (Carl Zeiss Inc., Thornwood, NY, USA) with a Plan-Apochromat 20x/0.8 objective lens. All images were acquired using a Hitachi HV-F202 SCL camera. Zeiss ZEN blue 2.3 software package was used for image processing and stitching.

Glycosphingolipid analysis:

Lipids from tissue homogenates were extracted with chloroform:methanol (1:2, v/v) overnight at 4°C. The GSLs were further purified using solid-phase C18 columns (Telos, Kinesis, UK). After elution, the GSL fractions were dried down under a stream of nitrogen and treated with recombinant ceramide glycanase (rEGCase, kindly provided by Orphazyme, Denmark) to obtain oligosaccharides from GSLs. The liberated glycans were then fluorescently-labelled with anthranillic acid (2AA). Excess 2AA-label was removed using DPA-6S SPE columns (Supelco, PA, USA). Purified 2AA-labelled oligosaccharides were separated and quantified by normal-phase high-performance liquid chromatography (NP-HPLC). The NP-HPLC system consisted of a Waters Alliance 2695 separations module and an in-line Waters 2475 multi λ-fluorescence detector set at Ex λ360nm and Em λ425nm. The solid phase used was a 4.6×250mm TSK gel-Amide 80

column (Anachem, Luton, UK). A 2AA-labelled glucose homopolymer ladder (Ludger, UK) was included to determine the glucose unit values (GUs) for the HPLC peaks. Individual GSL species were identified by their GU values and quantified by comparison of integrated peak areas with a known amount of 2AA-labelled BioQuant chitotriose standard (Ludger, UK). Results for tissue homogenates were normalized to protein content, determined by the bicinchoninic acid (BCA) assay.

Sphingosine analysis:

Sphingosine from tissue homogenates was extracted in chloroform:methanol (1:2, v/v) with sonication for 10 min at room temperature. Lipids were purified using SPE NH2 columns (Biotage, #470-0010-A). After elution, sphingosine species were labelled with o-Phthalaldehyde (OPA) for 20 min at room temperature in the dark and OPA-labelled lipids were taken for analysis by reverse phase high-performance liquid chromatography (RP-HPLC). The RP-HPLC system consisted of a VWR Hitachi Elite LaChrom HPLC system with a L-2485 fluorescence detector set at Ex λ340nm and Em λ455nm. The solid phase used was a Chromolith Performance RP-18e 100-4.6 HPLC column (Merck, Darmstadt, Germany). Individual sphingosine species were identified by their retention time and quantified by comparison of integrated peak areas with a known amount of OPA-labelled C20 sphingosine standard (Avanti Polar Lipids, Alabama, USA). Results were normalized to protein content, determined by the bicinchoninic acid (BCA) assay.

Behavioral Analysis:

Mice were scored weekly starting at 4 weeks of age based on the following categories: grooming, gait, kyphosis, ledge test, hindlimb clasp and tremor as previously published [89].

Each category had a range score from zero, meaning no phenotype, to three, as the most severe. A composite score for each animal was obtained by adding the scores for each of the 6 behavioral categories, resulting in a composite score range of 0 to 18.

Lifespan Measurement:

Each litter was born by a mother previously separated from a male once a vaginal plug was identified or the female was noticeably pregnant. Animals were weighed weekly after weaning (P28). Lifespan was measured by ACUC-approved end-point criteria of 30% weight loss from the maximum weight.

Colonies Management and Genotyping:

Npc1$^{em/Pav}$ was generated and genotyped as previously described in Chapter I. The *Npc1*^{nih} allele, also known as *Npc1*^{m1N} (JAX Mice 003092), was genotyped by using the following PCR primers (F: GGTGCTGGACAGCCAAGTA and R: GATGGTCTGTTCTCCCATG). As our end-point criteria was based on percentage weight loss, no nutritional supplements or food pellets on the cage floor were provided to animals. All animal procedures were performed in a pathogen-free, AAALAC- approved facility, in accordance with National Institutes of Health (NIH) guidelines and approved by the National Human Genome Research Institute (NHGRI) Animal Care and Use Committee (ACUC).

Statistical Analysis:

Statistical analyses were done using Prism software (GraphPad). For figures 3.1B and 3.2, an unpaired t-test was performed with $*p<0.05$ being significant. All survival analyses were done using the log-rank test (Mantel-Cox). For figure 3.8B, a two-way ANOVA test using genotype

and timepoints as the two factors was performed. A Bonferroni correction for multiple comparisons was also included. In all figures *$p<0.05$, **$p<0.001$, ***$p<0.0001$.

Results

Npc1^{em1Pav} is a hypomorphic allele:

The previous chapter described the generation of *Npc1^{em1Pav}* as a novel *Npc1* allele in mouse. We showed the responsible mutation consisted of a nine-base-pair in-frame deletion located in the cysteine-rich loop domain of NPC1. As expected, protein quantification by Western blot revealed a significantly reduced amount of NPC1 compared to littermates that was evident in both brain and liver tissues (Fig. 3.1A). Further analysis by quantification of the Western blot confirmed that NPC1 was significantly reduced in *Npc1$^{em1Pav/em1Pav}$* homozygotes in both the brain ($p=0.0068$) and in the liver ($p=0.0002$) compared to control littermates (Fig. 3.1B). The results indicate as expected, *Npc1^{em1Pav}* mutants have significantly reduced levels of NPC1 suggesting this a hypomorohic allele and not a null.

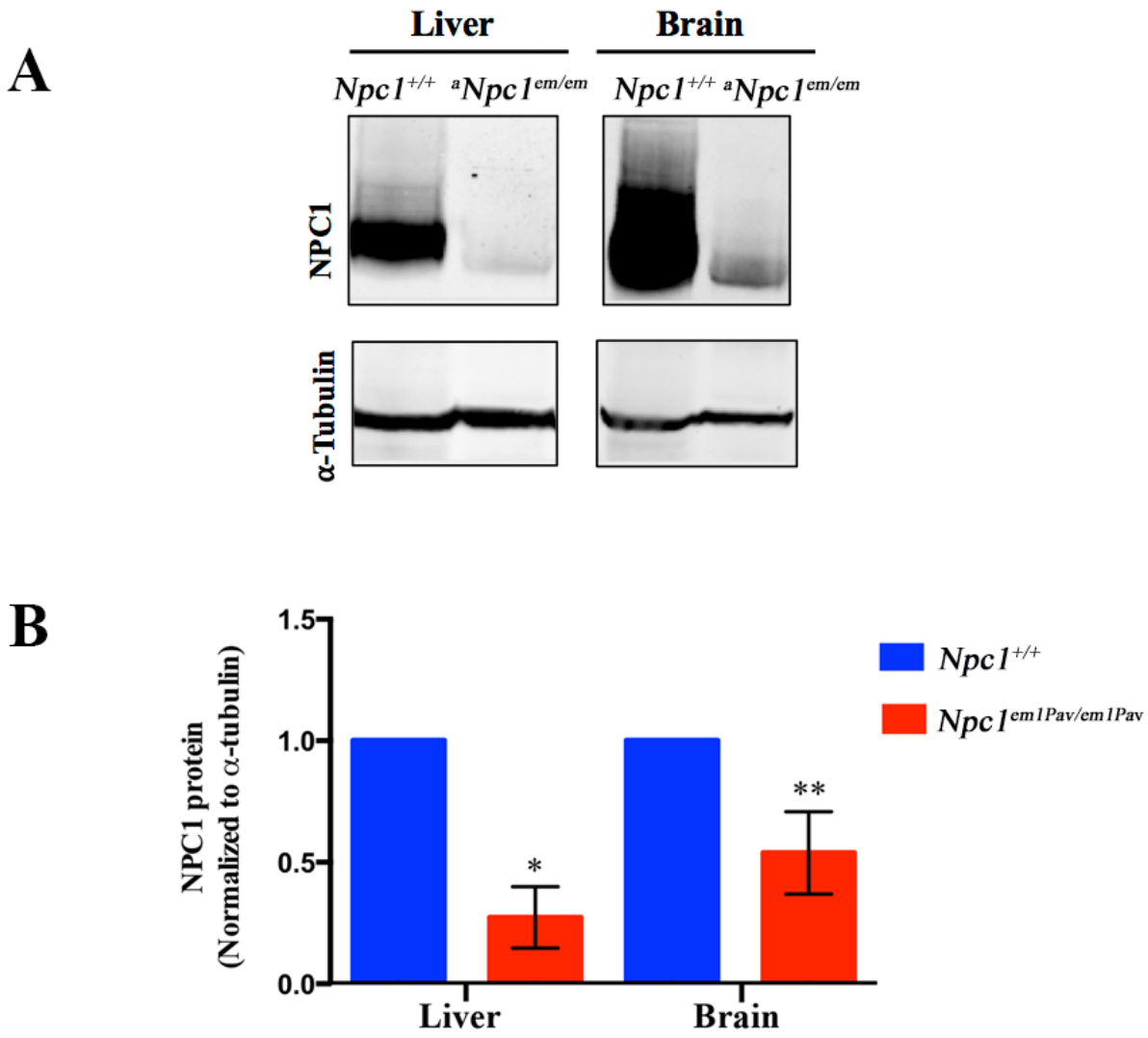


Figure 3.1 *Npc1*^{em1Pav} mutants have significantly reduced levels of NPC1 protein. **A)** Western blot analysis of NPC1 protein levels. Liver and spleen tissues were harvested at 8 weeks from *Npc1*^{em1Pav} mutants and control littermates (*Npc1*$^{+/+}$). ^{a}*Npc1*$^{em1/em1}$ was used as an abbreviated name for mutants (*Npc1*$^{em1Pav/em1Pav}$). **B)** Quantification of Western blot showed significant reduction in NPC1 in both liver (*p=0.0068)* and brain (*p=0.0002)*, when comparing *Npc1*^{em1Pav} mutants (N=2) and control littermates (N=2). *$p<0.05$, **$p<0.001$

Npc1 mRNA levels in _Npc1^{em1Pav}_ mutants do not correlate with NPC1 protein levels and are regulated in a tissue-specific manner:

Normalized levels of *Npc1* mRNA were measured by qRT-PCR Taqman assay in the spleen, liver and brain at approximately 9 weeks of age. In both the liver and the spleen, *Npc1* mRNA levels were significantly increased compared to control animals. However, no difference in expression level was observed in the brain (Fig. 3.2). The average cycle thresholds of detection (Ct) of the control groups were as follows: liver (24.51 $\pm$ 0.16, N=3), spleen (25.89 $\pm$ 0.44, N=3), and brain (24.87 $\pm$ 0.23, N=3). For the mutants the Ct values were: liver (22.81 $\pm$ 0.5, N=3), spleen (24.34 $\pm$ 0.45, N=3), and brain (24.22 $\pm$ 0.13). These Ct values were normalized to *Gapdh*

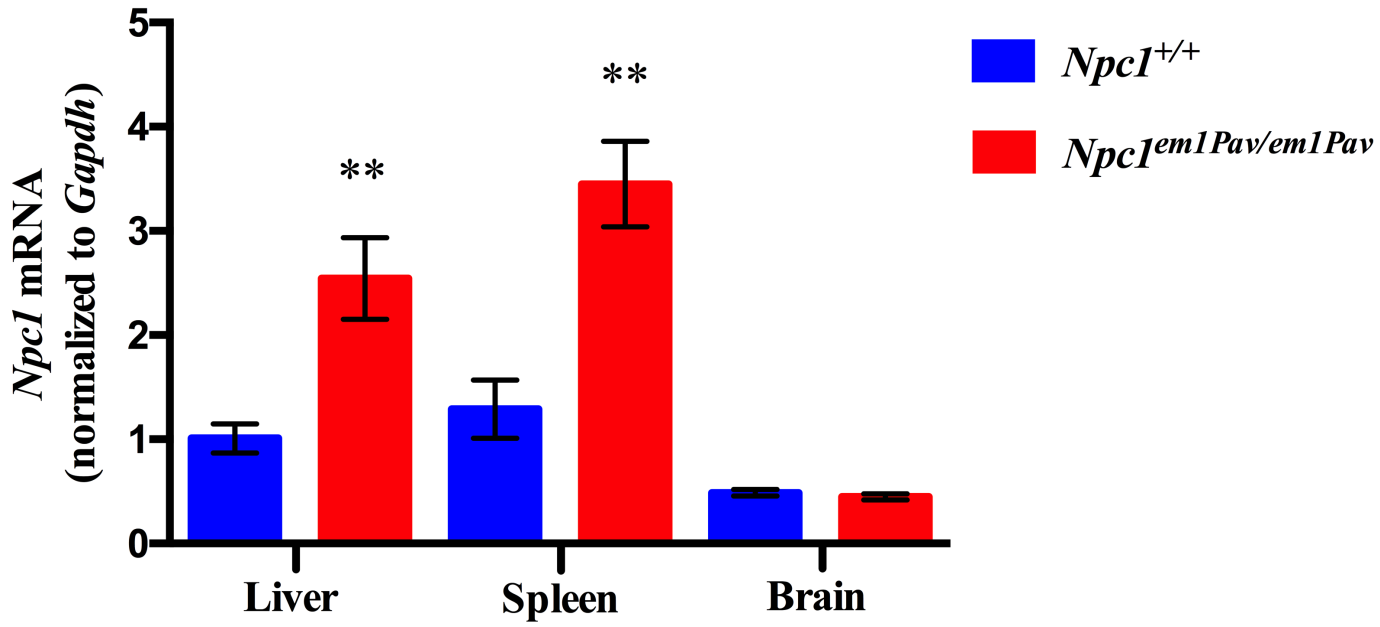


Figure 3.2 RT-qPCR analysis of *Npc1* mRNA normalized to *Gapdh*. Liver, spleen and brain were collected from both *Npc1*^{em1Pav} mutants (n=3) and control littermates (n=3) at P68. Both liver and spleen showed significantly higher levels of mRNA in the *Npc1*^{em1Pav} mutants compared to controls; *p=0.0031* and *p=0.0017,* respectively. *Npc1* mRNA levels in the brain were unchanged between the two groups (p=0.1749) ***p<0.001*.

Biochemical profile of *Npc1*^{em1Pav} shows marked lipid accumulation consistent with NPC1 deficiency:

As previously mentioned in Chapter I, loss of function in either NPC1 or NPC2 leads to accumulation of cholesterol and other lipids such as sphingolipids within the lysosome. GSL and sphingosine analysis of brain and liver tissues from *Npc1*^{em1Pav} mutants (P63 to P68) also showed a significant accumulation of total glycosphingolipids compared to controls ($p<0.0001$) (Fig. 3.4) This accumulation was similar to what was seen with the the null allele (*Npc1*^{nih}*)* also on a C57BL/6J genetic background (Fig. 3.4). These results indicate *Npc1*^{em1Pav} mutants recapitulated metabolic and storage disturbances associated with NPC.

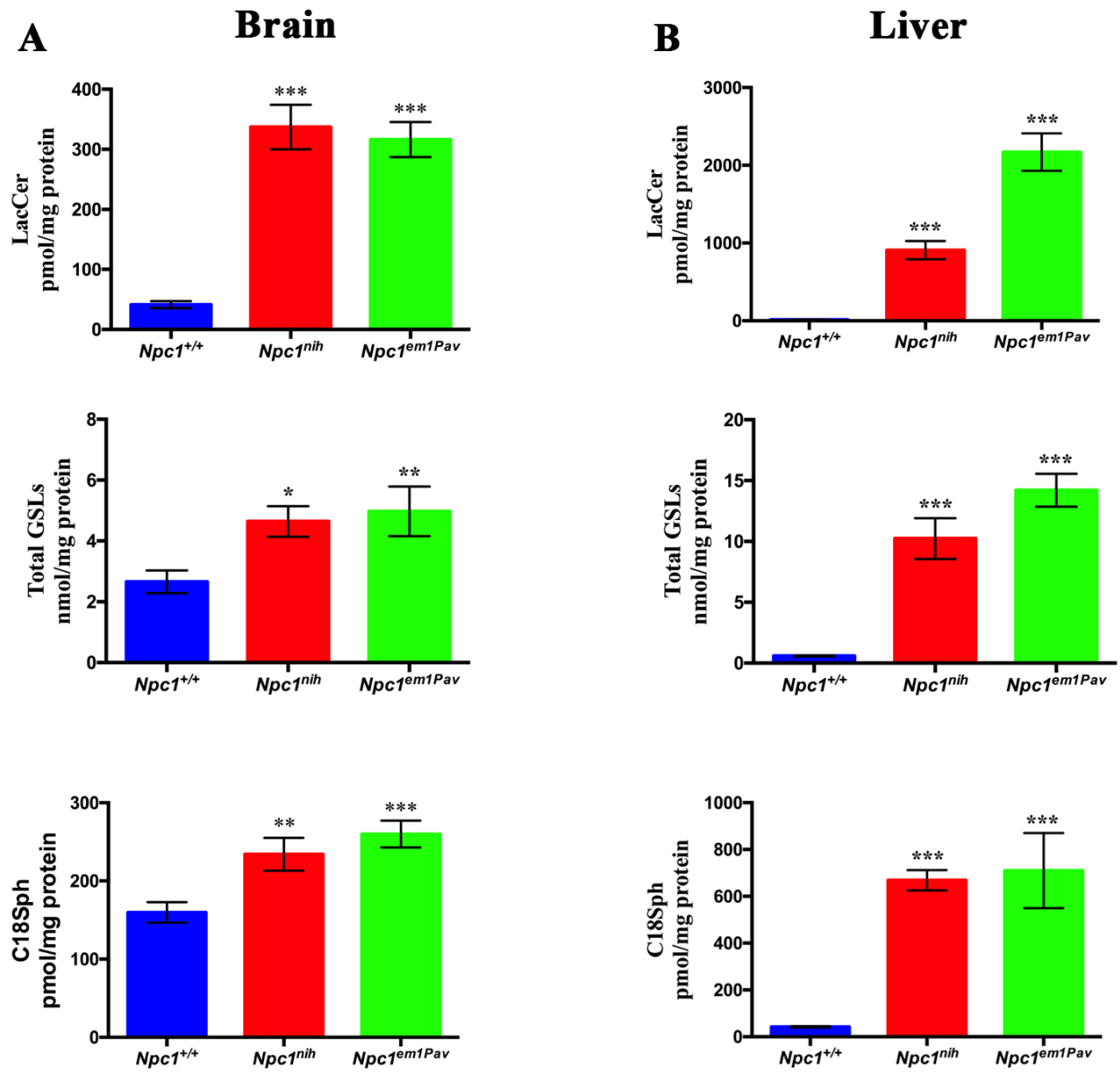


Figure 3.3 Abnormal lipid profiles in *Npc1*^{em1Pav}. Brain **A)** and liver **B)** were collected from controls (*Npc1*$^{+/+}$) n =3, *Npc1*^{nih} mutants (null allele) n=2 and *Npc1*^{em1Pav} mutants n=2, between P63 and P68. Similar to the null allele (*Npc1*^{nih}), *Npc1*^{em1Pav} mutants showed significantly elevated levels of LacCer, total GSLs and C18Sph compared to controls. All animals were on C57BL/6J genetic background. LacCer = lactosylceramide, GSL = glyconsphingolipids, C18Sph = sphingosine.

$Npc1^{em1Pav}$ mutants display classical storage pathology and neurodegenerative pattern consistent with NPC:

Histopathology of the liver and spleen of $Npc1^{em1Pav/em1Pav}$ mice confirmed the presence of foam cells at P21 and P68 detectable with H&E staining as well as with the macrophage-specific antibody CD68 (Fig. 3.4). This progressive infiltration of lipid-laden macrophages ultimately leads to architectural disruption of tissues such as the spleen (Fig. 3.5).

The cerebellum of $Npc1^{em1Pav}$ mutants showed no loss of Purkinje cells (Fig. 3.6 top) at P28, which is consistent with the lack of ataxia observed at this age. As the disease progressed (P68) the loss of Purkinje cells became apparent by immune-histochemistry (Fig. 3.6 middle and bottom).

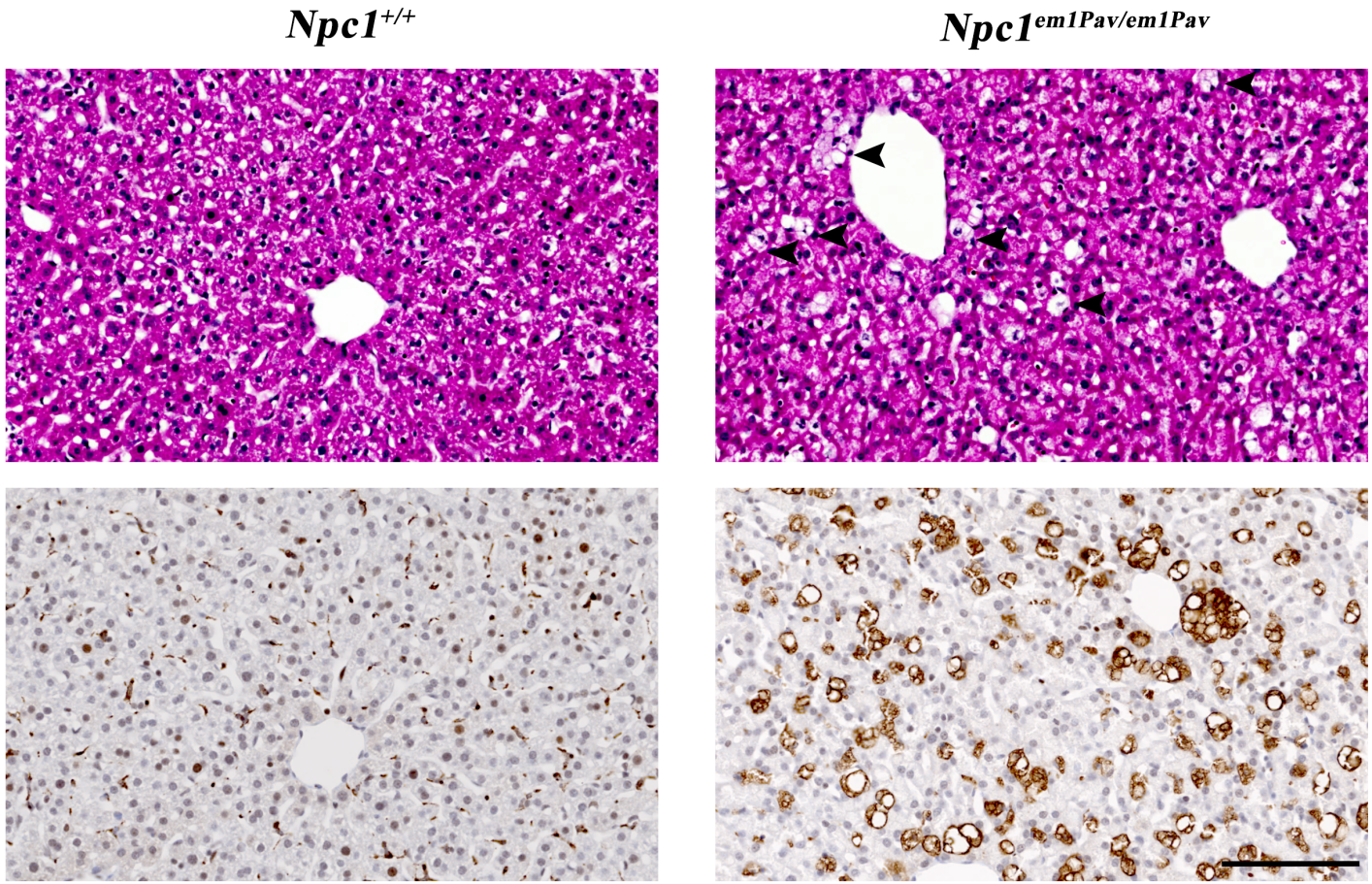


Figure 3.4 Histological analysis of liver tissue from *Npc1*^{em1Pav}. **Top row** shows H&E staining of control (*Npc1*$^{+/+}$) and of *Npc1*^{em1Pav} mutants (P21). Black arrowheads indicate foam cells. **Bottom panel**: Macrophages are visible (+CD68; brown) in the bottom two panels. Scale bar equals 100 μm.

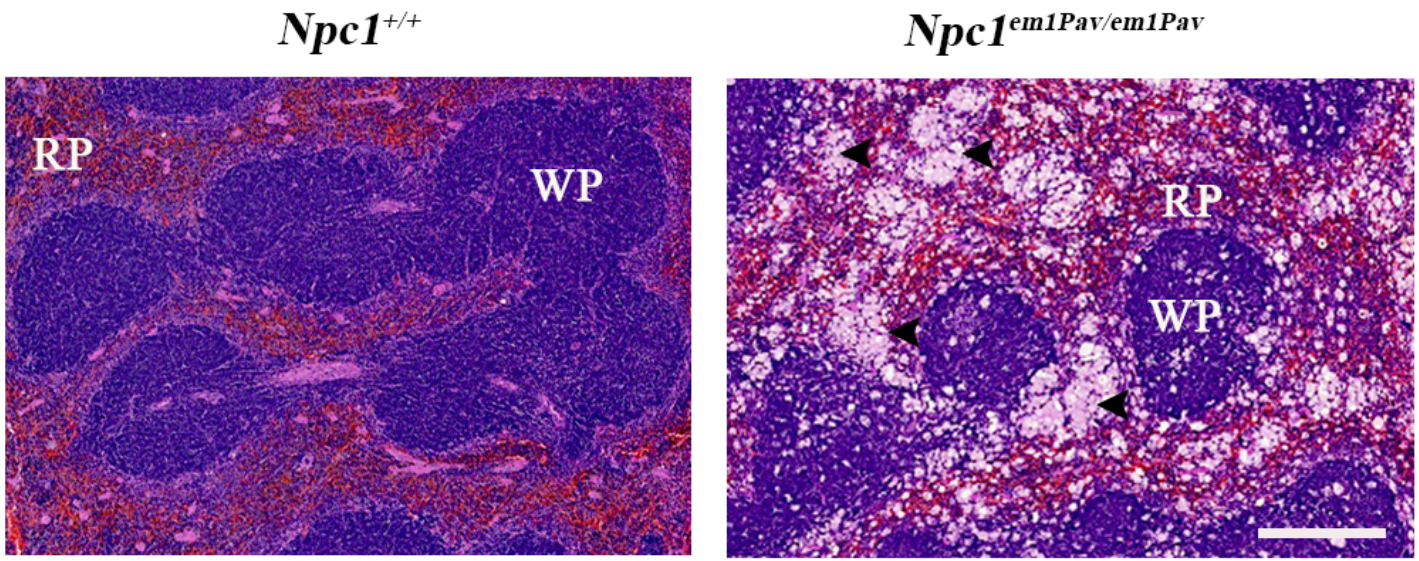


Figure 3.5 Histological analysis of spleen tissue from *Npc1*^{em1Pav}. H&E staining shows foamy appearance within the spleen tissue due to lipid-laden macrophages (black arrowhead) resulted in architectural disruption of both the WP (White Pulp) and RP (Red Pulp) at P68. Scale= 500μm.

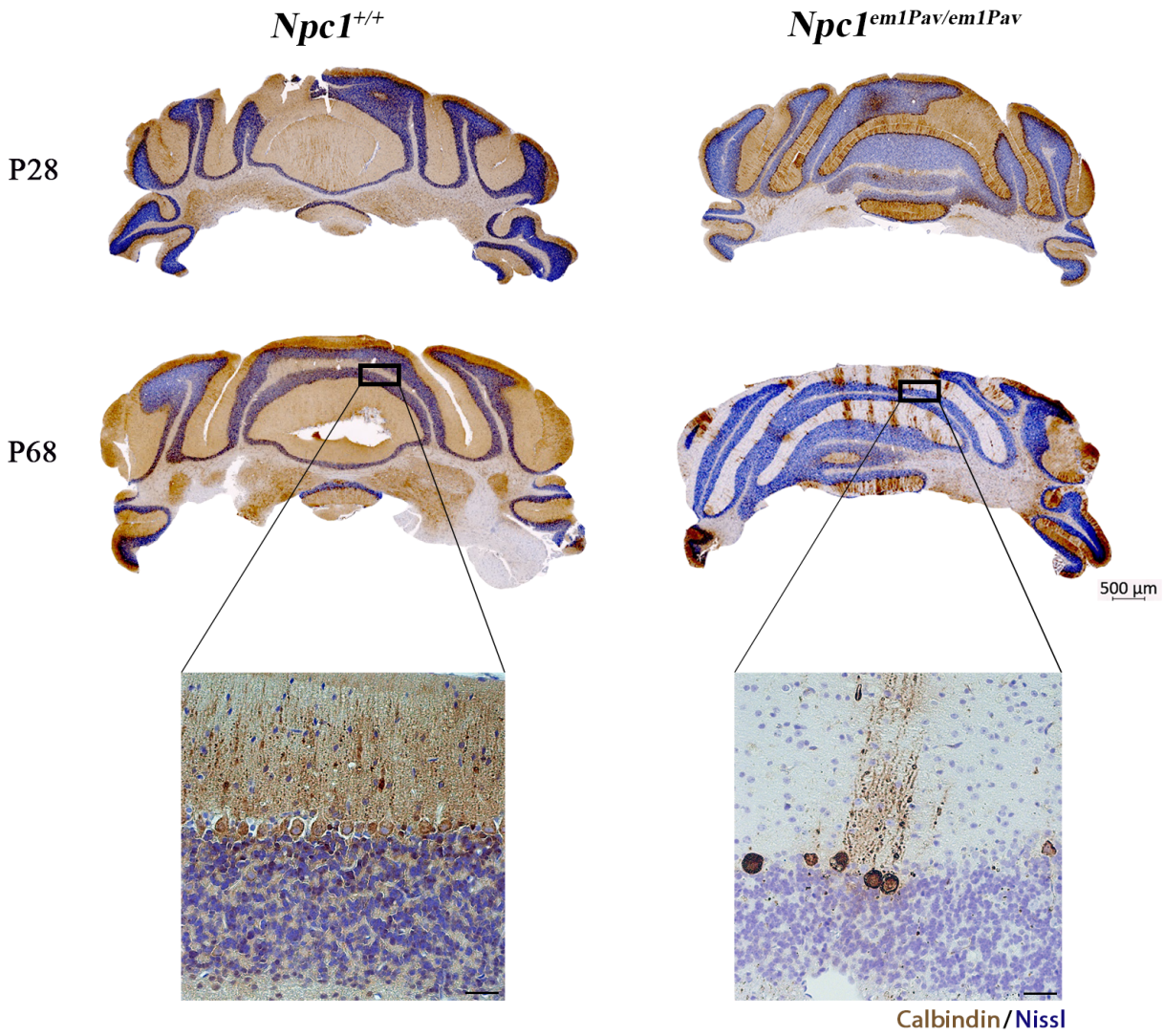


Figure 3.6 Purkinje cell loss in *Npc1*^{em1Pav} mutants. Each row shows age-matched *Npc1*^{em1Pav} mutants and littermate controls (*Npc1*$^{+/+}$). At P28, no difference is seen in Purkinje cells (Calbindin) between genotypes. In contrast, at P68 loss of Purkinje cells is evident in *Npc1*^{em1Pav} mutants compared to control littermates. The typical "zebra-like stripes" shown are due to temporal loss of Purkinje cells. This phenotype is also seen in other *Npc1* mouse models [58,62]. Bottom scale bar = 25µm.

Reduced lifespan and progressive weight loss onset in *Npc1*^{em1Pav} mutants:

Npc1$^{em1Pav/em1Pav}$ mice showed a significantly reduced lifespan, with a median survival of 70 days. Interestingly, they also have a significantly longer lifespan compared to the *Npc1*^{nih} null allele (mean survival of 63 days) in the same genetic background (C57BL/6J) (Fig. 3.7A), consistent with *Npc1*^{em1Pav} functioning as a hypomorphic *Npc1* allele. Allelism to the *Npc1* gene was established by failure to complement the *Npc1*^{nih} allele. As seen in Figure 3.7B, the lifespan of *Npc1*$^{nih/em1Pav}$ compound heterozygous mutants was not significantly different from the lifespan of *Npc1*$^{nih/nih}$ or *Npc1*$^{em1Pav/em1Pav}$ mice (p=0.058; p=0.7125 respectively), indicating that the *Npc1*^{em1Pav} phenotype is due to mutation at the *Npc1* locus and that the allele is unable to rescue the homozygote null phenotype.

Npc1$^{em1Pav/em1Pav}$ mutants also showed progressive weight loss starting at around 59 days of age. This weight loss was consistent for both males and female mutants (Fig. 3.8A&B). Most of the mutants were smaller at birth (see Chapter V) and as adults in comparison to their control littermates.

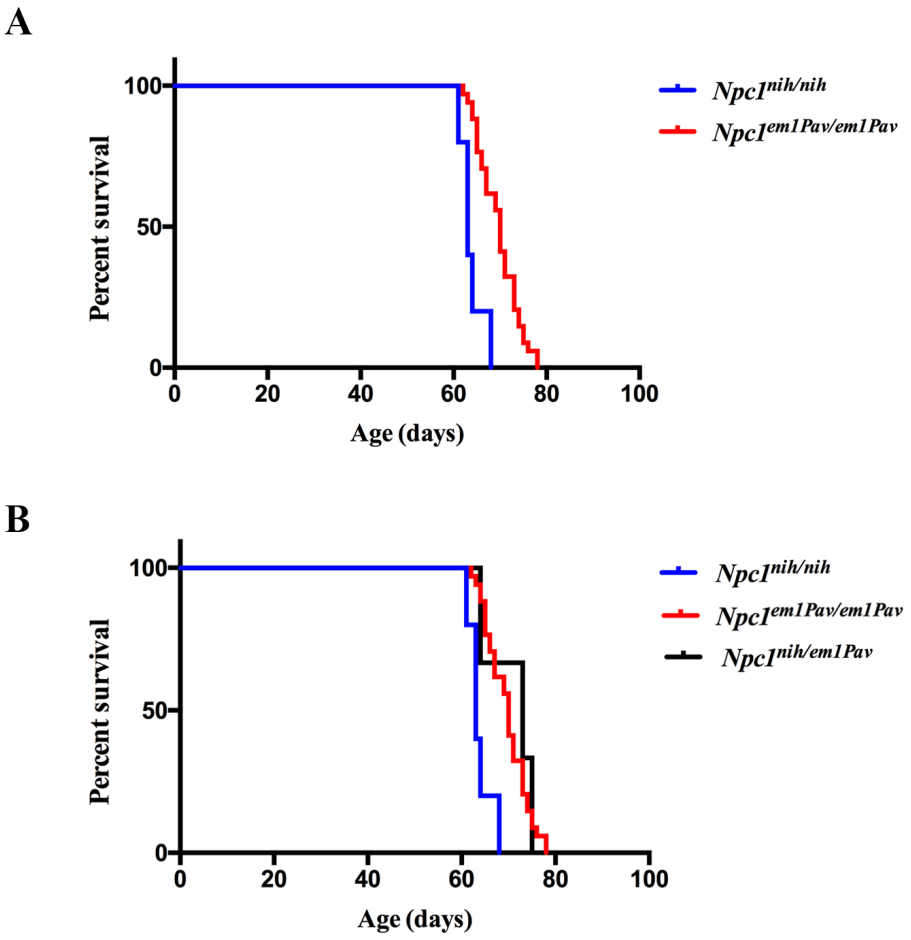


Figure 3.7 Survival analysis of *Npc1*$^{em1Pav/em1Pav}$ **A)** Survival analysis comparing *Npc1*^{em1Pav} and *Npc1*^{nih} alleles. Both alleles were on a C57BL6/J background. *Npc1*^{em1Pav} (n=34) mean survival was 70 days, which was significantly longer ($p<0.0001$) than 63 days mean survival for the null allele, *Npc1*^{nih} (n=4). **B)** Complementation test between *Npc1*^{nih} (blue line) and *Npc1*^{em1Pav} (red line) was done by generating *Npc1*$^{nih/em1Pav}$ (black line). No differences in lifespan were observed between *Npc1*^{nih} vs. *Npc1*$^{nih/em1Pav}$ (p=0.06), or *Npc1*^{em1Pav} vs. *Npc1*$^{nih/em1Pav}$ (p=0.71).

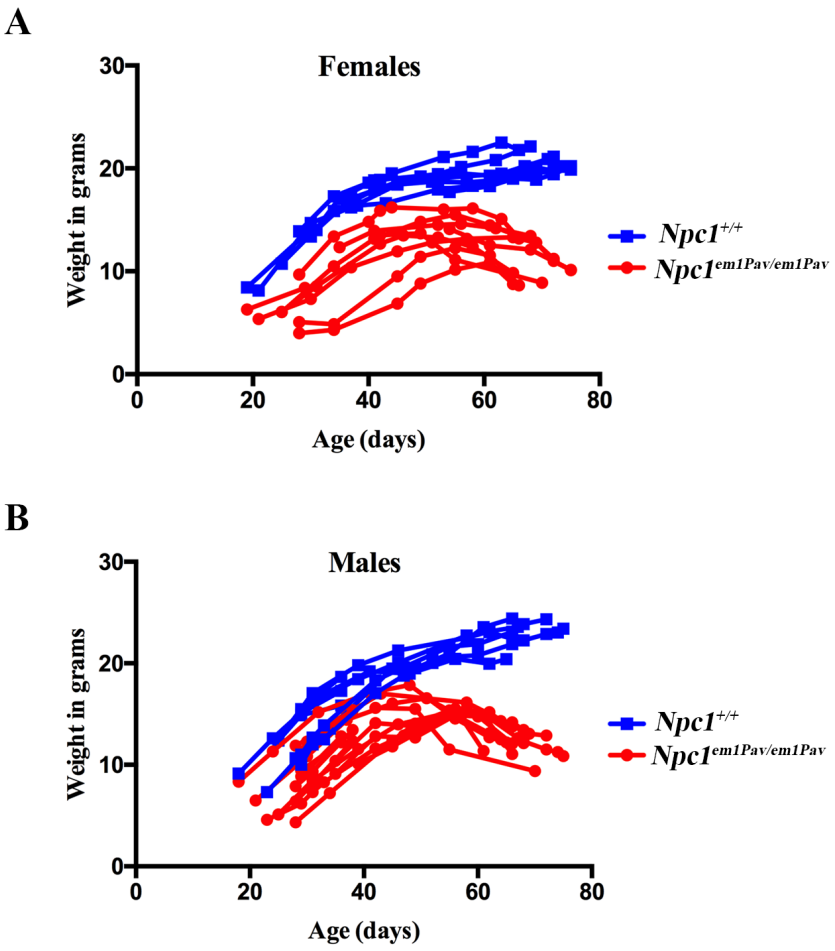
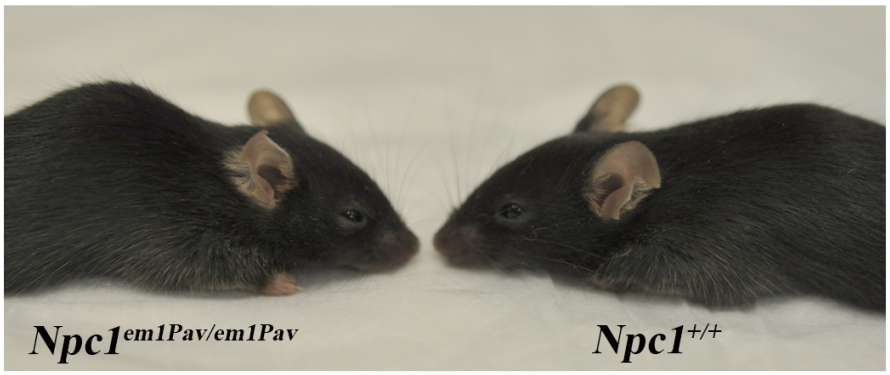


Figure 3.8 Progressive weight loss in *Npc1*$^{em1Pav/em1Pav}$ separated by gender. Weight loss onset was observed at around 59 days for both genders. **A)** Females. Controls shown by blue line (n=8) and *Npc1*^{em1Pav} mutants shown by red line (n= 10) **B)** Males. Controls shown by blue line (n=9) *Npc1*^{em1Pav} mutants shown by red line (n= 16).

$Npc1^{em1Pav}$ mutants display ataxia and other neurogenerative phenotypes characteristic of NPC:

As previously mentioned, some of the hallmarks of *Npc1* mouse models are phenotypes of progressive motor impairment, such as ataxia and changes in gait. Starting at week 4, a weekly composite score was measured as the sum of scores given for the following six categories as previously described [89] grooming, kyphosis (curvature of the spine) (Fig. 3.9A), ledge test, hindlimb clasp and tremors (Fig. 3.9B). $Npc1^{em1Pav}$ mutants do not show any phenotype at weaning (P28). As the disease progresses, the score becomes significantly higher compared to age-matched controls. The earliest noticeable phenotype was change in gait accompanied with kyphosis. Hindlimb clasping was observed at a later stage of the disease (week 9). These results confirm $Npc1^{em1Pav}$ exhibited phenotypes associated with neurodegeneration and motor impairment previously observed in other *Npc1* mutants.

A



B

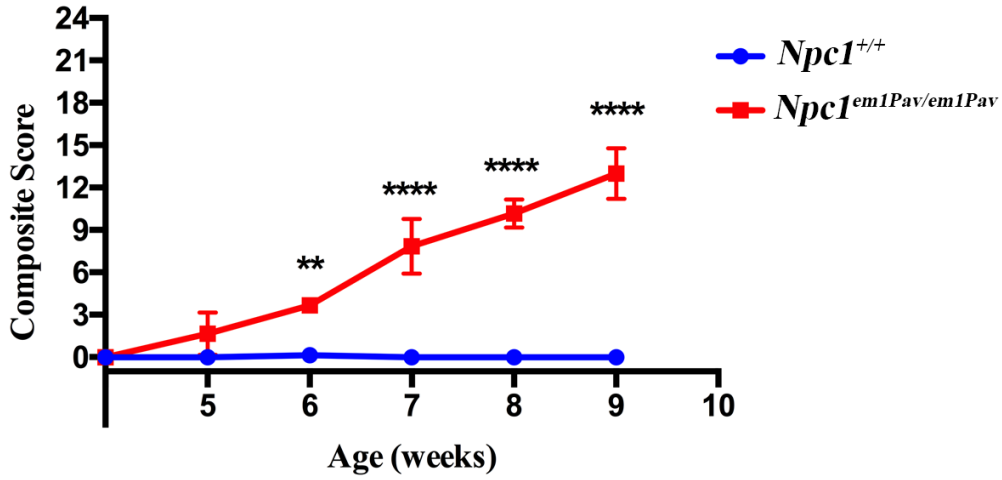


Figure 3.9 Neurodegenerative and behavioral phenotypes in *Npc1*$^{em1Pav/em1Pav}$. **A**) Kyphosis (curvature of the spine) was present in *Npc1*^{em1Pav} mutants (n=6) compared to control littermates (n=6). **B**) Progressive neurodegenerative and motor impairment in *Npc1*^{em1Pav} mutants. A combination of six different neurodegenerative phenotypes and behavioral tests were scored weekly starting at weaning (P28) and combined into a composite score (see methods for details). A higher score means greater severity. $^{**}p<0.001$, $^{****}p<0.00001$.

Discussion

In this chapter we characterized *Npc1*^{em1Pav} as a novel and valid NPC mouse model. As previously described, the mutation responsible for this new allele is a nine-base pair in-frame deletion. As predicted, we showed based on protein quantification this is not a null allele with *Npc1*^{em1Pav} mutants expressing residual NPC1 protein. However, this level of expression is significantly lower when compared to control levels in both brain and liver tissues. We also showed that because *Npc1*^{em1Pav} is a hypomorphic allele, *Npc1*^{em1Pav} mutants have a longer lifespan when compared to the null allele (*Npc1*^{nih}) in the same genetic background (C57BL/6J). Allelism to the *Npc1* gene was also established with a complementation test where the *Npc1*^{em1Pav} allele failed to complement the previously well characterized null allele, *Npc1*^{nih}.

When quantifying *Npc1* mRNA levels from *Npc1*^{em1Pav} mutants, we showed in peripheral tissues such as the liver and spleen mRNA levels did not correlate with diminished NPC1 protein levels, as they were actually higher in the *Npc1*$^{em1Pav/em1Pav}$ homozygotes. Previous publications have also shown similar results in homozygous I1061T patient-derived fibroblasts as well as the I1061T mouse model (*Npc1*$^{tm1.1Dso}$) [62,67]. These studies showed similar to our results, there is no correlation between the levels of transcribed *Npc1* and the amount of mutant protein. These data suggest *Npc1* is regulated at the transcriptional level, possibly by a feedback mechanism in response to lower protein levels. In the specific case of another hypomorphic mouse model such as *Npc1*$^{tm1.1Dso}$, denatured NPC1 protein from the brain of *Npc1*$^{tm1.1Dso}$ mutants was shown to have a higher molecular weight [62]. This could lead to a hypothesis of NPC1 protein post-translational modifications such as glycosylation being different in the brain tissue compared to the liver or spleen. In our analysis we also showed that in contrast to the liver and spleen, the

brain seems to be unique since there was no difference in *Npc1* mRNA levels between the two genotypes. These findings could be important for future targeted mRNA stability treatments such as anti-sense oligonucleotides [50] and already tested/ongoing treatments such as histone deacetylases inhibitors [90]. Our results only showed mRNA levels normalized to *Gapdh*, a widely used housekeeping gene. Additional housekeeping genes such as *Actb* should be used in order to validate these results.

Accumulation of lipids in the reticuloendothelial system leads to the presence of foam cells in peripheral tissues seen in NPC. These lipid-laden macrophages become enlarged and easily distinguished in liver and spleen by H&E staining. Our pathology work-up showed this classical foamy appearance in both liver and spleen from $Npc1^{em1Pav}$ mutants.

One of the main clinical presentations we see in NPC patients is cerebellar ataxia. When analyzing the cerebellum of $Npc1^{em1Pav}$ mutants, we showed loss of Purkinje cells with disease progression. This led to motor impairment, quantified by behavioral tests showing a deterioration of $Npc1^{em1Pav}$ mutants over time. Other neurodegenerative phenotypes such as kyphosis (curvature of the spine) were shown to be present $Npc1^{em1Pav/em1Pav}$. This is thought to be due to proximal muscle weakness [91,92].

In this chapter we have shown the characterization process of our novel NPC mouse model. Based on our results we can conclude that $Npc1^{em1Pav}$ mutant mice are able to recapitulate many aspects of NPC disease. In the new few chapters we will describe how by using this new mouse model we will be able to set-up a mapping project in order to look for genetic modifiers (Chapter IV) as well as uncharacterized phenotypes associated with NPC (Chapter V).

Summary

- *Npc1*$^{em1Pav/em1Pav}$ mice recapitulate the storage pathology, lipid profile and neurodegenerative abnormalities that are characteristic of NPC disease, indicating they are a valid NPC animal model.
- We will use this mouse model to find genetic modifiers and uncharacterized phenotypes associated with NPC

Chapter IV: Using *Npc1*^{em1Pav} to map genetic modifiers of NPC

Introduction

Phenotypic variation can arise from multiple causes, including environmental or genetic factors [72,73]. With the advancement of new sequencing technology, an increased number of causative genes have been identified for many Mendelian disorders [69]. Further analysis of these disease-causing mutations has revealed phenotypic variation still exists even when accounting for the "causative-gene", underlying the importance of gene-to-gene interactions. [70,71].

A genetic modifier can be defined as a genetic variant that interacts with other genetic elements by different mechanisms ultimately leading to expression changes displayed as a phenotype. [74,93]. As previously discussed, this phenomenon is observed in NPC, as evidence suggests the presence of genetic modifier(s) in *Npc1* mouse models [62,78-80] and human patients [75-77]. Genetic modifiers can be discovered by analyzing how genetic variants correlate to the phenotypic variation within an affected population. This can be done using patient's genotypic and clinical data [94,95]. In the case of rare disorders such as NPC, where sample size is limited, model organisms such as the common house mouse (*Mus musculus*) can be used instead [96,97]. Mouse strains also provide an inbred background, which cannot be achieved with human patients. Currently available inbred strains are derived from the original colonies established by William Castle and Abbie Lathrop in the early 1900's [98]. The level of genotypic and phenotypic similarities between them depend on how closely related they are to each other based on their genealogy [99]. Furthermore, these genetic changes can translate into functional differences. For example, differences in immune response between C57BL/6J and BALB/cJ have resulted in strain-specific susceptibility to certain infections [100-102]. More genetically

similar strains such as C57BL/6J and C57BL/6N can offer a powerful tool for QTL linkage analysis due to a decreased unique number of variants between them [103]. Strain-specific differences in *Npc1* mutants have been reported in disease onset and/or severity between mouse strains such as C57BL/6J and BALB/cJ [62,80], and also C57BL/6KsJ or C57BL/6J and DBA/2J [78,79]. However, the genetic variants responsible for these differences are still unknown [62].

As previously mentioned in Chapter I, we have generated a new *Npc1* allele ($Npc1^{em1Pav}$). We have also shown $Npc1^{em1Pav}$ mutants are able to recapitulate many aspects of NPC (Chapter II), thus providing a valid model of the disease. We hypothesize that by comparing this *Npc1* mutation between genetic backgrounds such as C57BL/6J (original strain) BALB/cJ and C57BL/6N we will observe strain-specific differences resulting in lifespan changes due to the presence of genetic modifiers. In addition, by using newly developed genomic tools we can potentially identify these unknown genetic variants. In this chapter we will describe our approach to mapping these modifier genes using the $Npc1^{em1Pav}$ allele.

Materials and Methods

Mouse Strains:

BALBc/J (Stock number: 000651) and C57BL/6J (Stock number: 000664) mice were imported from Jackson Laboratories (ME, USA). C57BL/6N were imported from Taconic Farms (MD, USA).

Speed Congenics:

Npc1^{em1Pav} heterozygote mice on a C57BL/6J background were backcrossed to BALB/cJ for four generations using marker-assisted selection (Speed congenics) (Fig. 4.2). Mouse genomes were assessed at the DartMouse™ Speed Congenic Core Facility (Geisel School of Medicine, Dartmouth College) using the Infinium Genotyping Platform (Illumina, Inc; San Diego, CA) to interrogate a custom panel of 5,307 SNPs spread throughout the genome. The raw SNP data were analyzed using DartMouse's SNaP-Map™ and Map-Synth™ software, allowing the determination for each mouse of the genetic background at each SNP location. For each generation, the top three males with the highest percentage of BALB/cJ homozygosity were selected in order to establish the next generation. Subsequent backcrosses have been performed for up to nine generations to date.

Lifespan Measurement for Mapping:

Each litter was born to a mother previously separated from a male once a vaginal plug was identified or the female was noticeably pregnant. Animals were weighed weekly starting at weaning (P28). The maximum weight was recorded, and lifespan was defined by NHGRI ACUC approved end-point criteria of thirty percent weight loss from the maximum weight. Animals were euthanized, and tails were collected for DNA extraction.

Colony Management:

All colonies were maintained by following the standard protocol of the NHGRI Animal Care and Use Committee (ACUC). Heterozygotes were mated to generate homozygote mice for analysis. Genotype identification was performed as previously described in Chapter II.

DNA Extraction:

DNA was extracted from pup tail biopsies at P10 and purified using a Gentra Puregene Mouse Tail Kit (Qiagen). For the N2 backcross generation, each sample was analyzed for concentration and purity using a DS-11 Series Spectrophotometer/Fluorometer (DeNovix).

Genotype of Samples Used for Genetic Mapping:

DNA samples were shipped to Neogen (NE, USA) for genotyping. Concentration was at least 100ng/μl for all samples. Total DNA per sample was 1μg. A total of 202 samples were sent from the N2 backcross [B6J(B6JCF1)] generation. DNA from the parental generation (B6JCF1 hybrids) as well as a C57BL/6J female were also included as genotype controls for data analysis. All samples were genotyped using the Giga Mouse Universal Genotyping Array (GigaMUGA) from Neogen (NE, USA). The array included more than 140K SNPs spread throughout the genome, providing informative markers for most mouse strains.

Statistical Analysis:

Statistical analyses were done using Prism software (GraphPad). For figures 4.5, 4.7 and 4.9 an ordinary one-way ANOVA was performed with multiple comparisons using C57BL/6J as the

control group. For figure 4.16, a student's t-test was performed. All survival analyses were done using the log-rank test (Mantel-Cox). In all figures *$p<0.05$, **$p<0.001$, ***$p<0.0001$.

Genotype Data Analysis:

Csv files containing genotype calls from GeneSeek (Neogen Corp.) were uploaded into Galaxy using a Linux platform (galaxyproject.org) for data formatting. Further data manipulation was achieved by using Partek Genomic Suites (Partek Inc.) Non-informative variants were excluded based on control samples (Parental F1 and C57BL/6J only animals) as well as unreliable markers that failed in control samples or the majority of N2 samples. A total of 28,873 markers were informative between the two strains (C57BL/6J and BALB/cJ). Genotype calls were classified as AA for C57BL/6J homozygous and AB for heterozygote (C57BL/6J and BALB/cJ).

QTL Linkage Analysis:

A mouse map converter (http://churchill-lab.jax.org/mousemapconverter) was used to convert the position of each SNP marker from base pair (GRCm38/mm10) to cM (Sex Averaged cM-Cox) [104,105]. QTL linkage analysis was performed using a data format as previously described [106] using both J/qtl (Jackson Laboratories) and R/qtl [107]. One QTL genome scan was performed selecting lifespan as the phenotype with a normal distribution. A permutation test (10,000 permutations) was done to obtain a 5% significance threshold (LOD = 3.09).

Analysis of Candidate Genes:

Genomic regions of interest for each of the two significant QTL peaks were defined using a 1.5-LOD support interval flanking the SNP with the maximum LOD score, as previously recommended [108]. The Mouse Genomes Project (Wellcome Sanger Institute) was used to

identify all known SNPs, indels and structural variants (SVs) within each genomic region that differ between C57BL/6J and BALB/cJ. The following filters were selected to retain SNPs most likely to impact protein function: missense variants, splice acceptor variant, splice donor variant, splice region variant, stop gained and stop loss. In order to predict the consequences for these variants, PROVEAN and SIFT scores were obtained (htpp://provean.jcvi.org/index.php) from J. Craig Venter Institute. These two scores have been widely used in order to predict pathogenic variants [109]. Both scores use predictive algorithms based on protein sequence conservation, however PROVEAN can calculate predicted consequences for both indels and SNPs [110] while the SIFT algorithm is limited to SNPs. The PROVEAN score categorizes variants as either neutral and deleterious. Similarly, the SIFT score categorizes variants as either tolerated and damaging. Only variants with deleterious (PROVEAN) or damaging (SIFT) scores were retained for further analysis. A list of candidate genes from these selected variants was generated from both QTL regions. All genomic regions were analyzed using coordinates from the GRCm38/mm10 build.

Results

Lifespan as a quantitative trait:

As previously mentioned, several studies have shown strain-specific differences in NPC severity usually measured by survival (lifespan) [62,80]. Methods to measure the lifespan in *Npc1* mutants have combined aspects of the phenotype including weight loss and inability to reach food or water (moribund state) [62,63]. For our genetic linkage study, we wanted to use lifespan as a quantitative trait. However, defining lifespan using this combination of weight loss plus inactivity could be difficult to apply to the large number of *Npc1*^{em1Pav} mutant mice required for linkage studies. Measurements of inactivity (moribund state) are potentially highly variable between assessors as it requires additional training and expertise with *Npc1* mutant mice. Therefore, we first evaluated if weight loss as a single end-stage criterion could be a surrogate for lifespan in NPC.

Based on anecdotal evidence from our previous NPC mouse studies, we defined 30% weight loss from the peak weight as the end criterion. When measuring 30% weight loss and inactivity (moribund state) ascertained by a single assessor in *Npc1*^{em1Pav} mutants, we found a direct correlation between these two variables (R^2=0.85, $p<0.0001$) (Fig. 4.1). We also noticed once the animals reached 30% weight loss, all of them were at or only a few days away from becoming inactive and in need of euthanasia. These results suggested that 30% weight loss could be used as a valid, consistent measurement of lifespan in *Npc1*^{em1Pav} mutants. Thus, we weighed mice once a week beginning at weaning (P28), changing to daily weights as *Npc1*^{em1Pav} mutants were approaching 30% weight loss. Lifespan was recorded as the number of days between birth and the day the mice reached 30% weight loss.

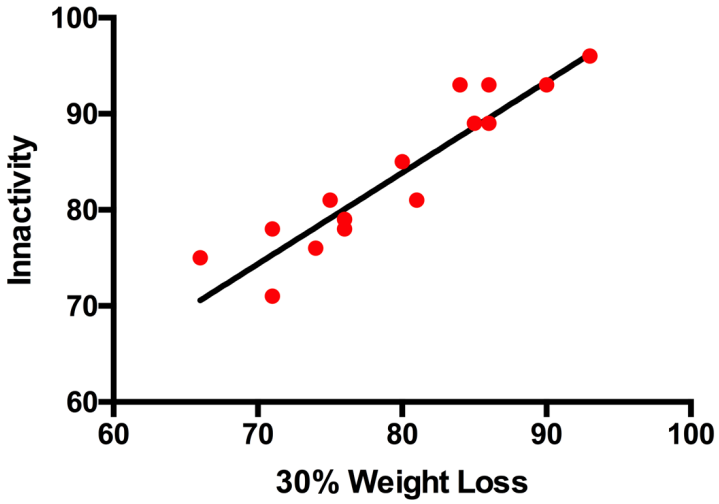


Figure 4.1 Positive correlation between two end-point criteria in *Npc1*$^{em1Pav/em1Pav}$. The age at which each *Npc1*^{em1Pav} mutant reached 30% percent weight loss relative to peak weight was recorded (X-axis). A measurement for inactivity or moribund state (Y-axis) was also recorded as unable to reach food and water due to lethargy. A significant correlation was found between these two variables (R^2=0.85, *p<0.0001*, n=17) and 30% weight loss was chosen as the end-point criteria measured for subsequent QTL mapping.

BALB/cJ background increases survival in *Npc1*^{em1Pav} mutants

In order to quickly establish a congenic strain of the *Npc1*^{em1Pav} allele on a BALB/cJ background, we used a marker-assisted selection as described in Figure 4.2. Genome scan results showed the top three males from the N3 generation genotyped as homozygous BALB/cJ for at least 75% of the informative SNP markers (Fig. 4.3). The top three breeders were then selected and crossed with BALB/cJ females (backcross). Ten males from the next generation (N4) were also genotyped to identify the top three males from this generation which genotyped as homozygous BALB/cJ for at least 92% of the markers (Figure 4.4). We then measured the lifespan of *Npc1*^{em1Pav} homozygous mutants at each of these generations (N3 & N4) by performing a heterozygous intercross and comparing the lifespan to *Npc1*^{em1Pav} mutants on a C57BL/6J genetic background.

Lifespan of *Npc1*^{em1Pav} mutants from the N3 intercross [C(B6JC)N3 x C(B6JC)N3] generation was significantly longer than C57BL/6J ($p<0.01$), and this difference was even greater at the N4 intercross [C(B6JC)N4 x C(B6JC)N4] generation ($p<0.0001$) (Fig. 4.5). These results support our hypothesis that strain-specific variants between C57BL/6J and BALB/cJ play a role in NPC survival.

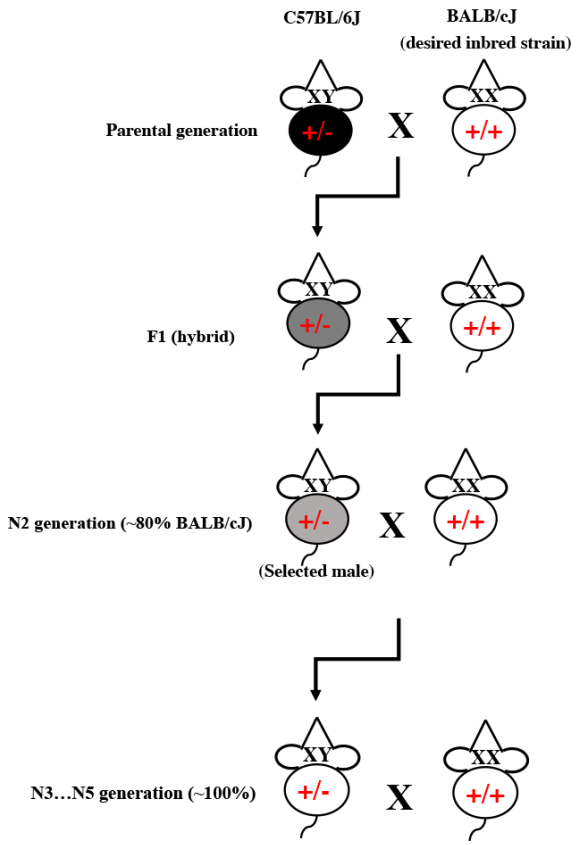


Figure 4.2 Protocol for marker-assisted selection (Speed congenics). The parental generation should include the desired inbred strain (e.g. for our project: BALB/cJ). Males are selected for genotyping starting at the N2 backcross generation. Based on the genome scan results, the males with the highest percentage of markers from the desired inbred strain are selected as breeders for the next generation. The same steps are repeated at each subsequent generation until N5. By targeting male breeders carrying the highest percentage of the desired inbred strain, a congenic strain can be obtained in only five generations (1.25 years) compared to the traditional backcross which can take up to ten generations (2.5 years). +/- = *Npc1*$^{+/em1Pav}$; +/+ = control. Shading color is a representation of genetic background with black representing the C57BL/6J strain and lighter shades of gray representing the increasing genomic contribution of BALB/cJ.

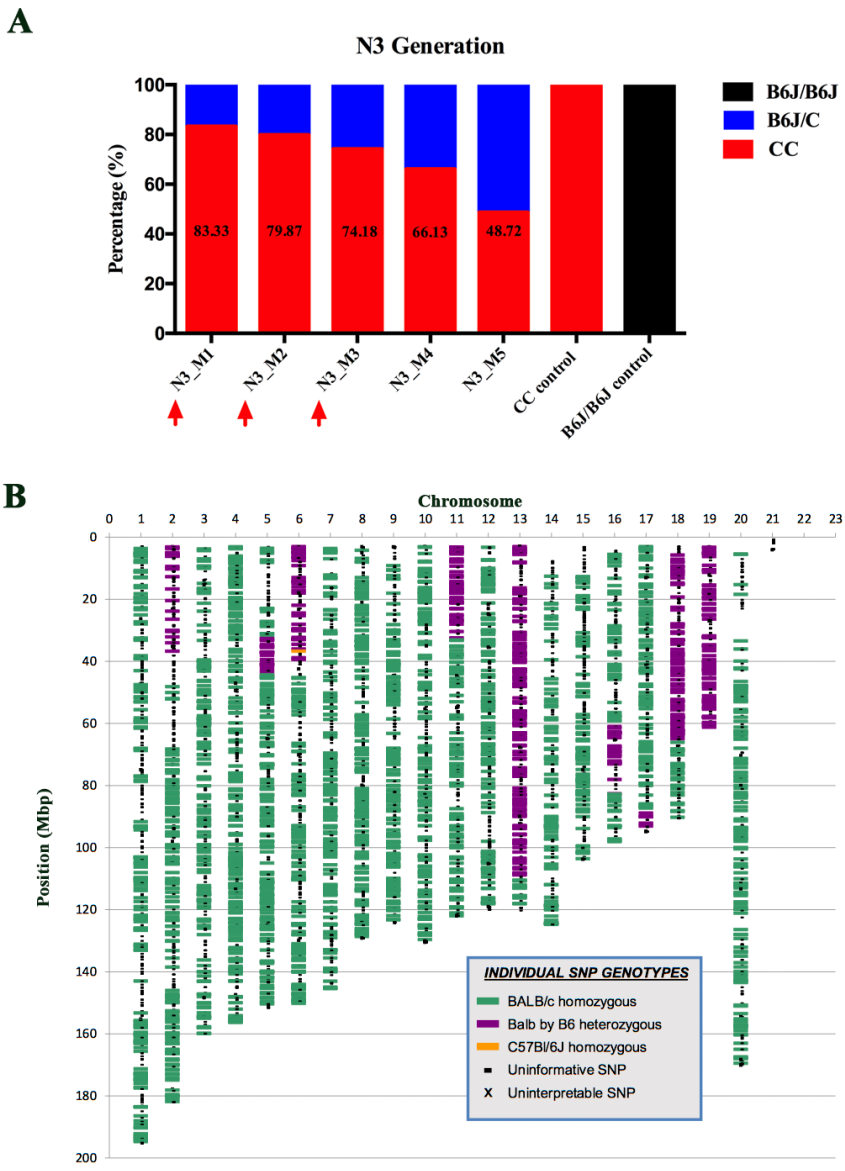


Figure 4.3 Marker-assisted selection results from *Npc1*^{em1Pav} heterozygous males (N3). A) Results for all genotyped males are shown as percentage of the SNPs with each of the possible genotypes: homozygous BALB/cJ (red), heterozygous C57BL/6J and BALB/cJ (blue). Red arrows denote the top three male breeders selected to generate N4 offspring. **B)** View by chromosome for the genome scan results of the top male (N3_M1) showing the location for each of the SNP markers with their respective genotype call. B6J=C57BL/6J, C=BALB/cJ.

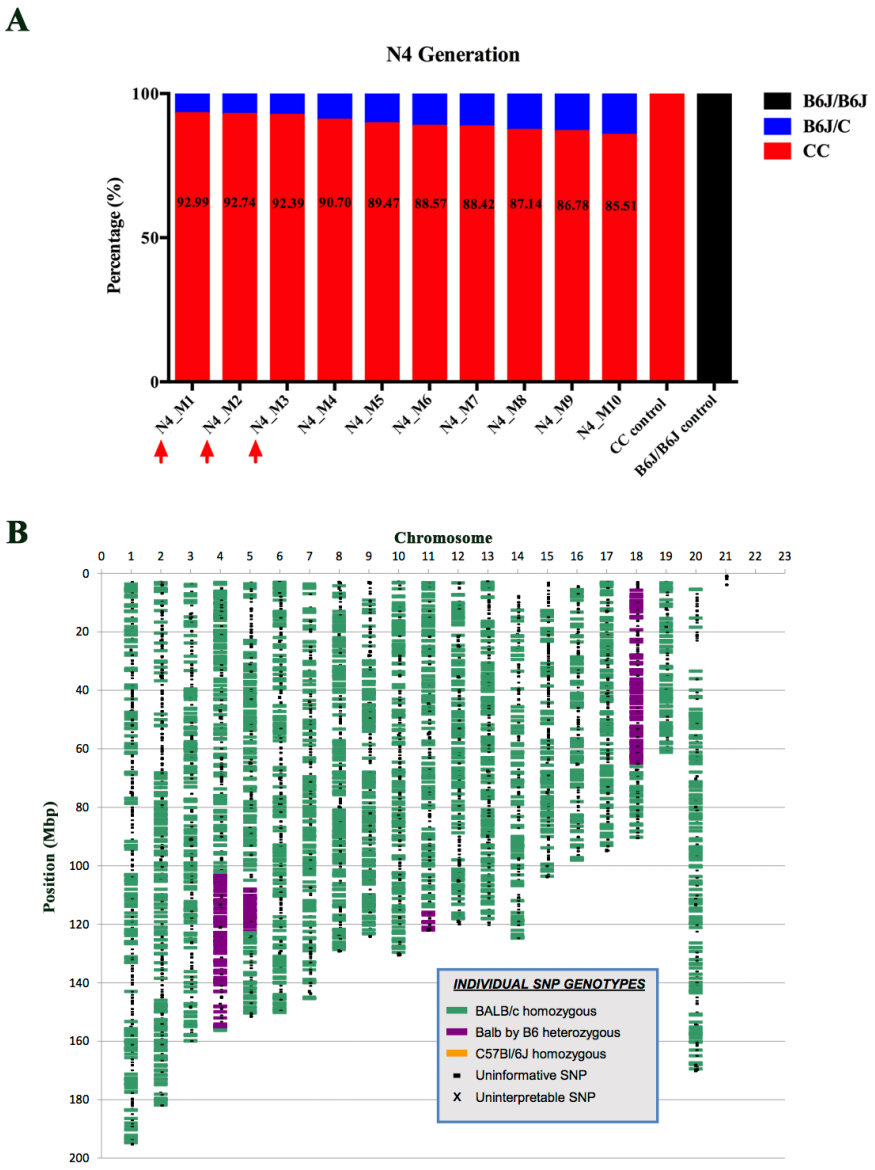


Figure 4.4 Marker-assisted selection results from *Npc1*^{em1Pav} heterozygous males (N4). A) As in the previous figure results are shown for the genotypes of each N4 male. Notice the increase of BALB/cJ homozygosity compared to the previous generation. Red arrows denote the males selected for further breeding. **B)** Genome scan results per chromosome from the male with the highest percentage of BALB/cJ homozygosity (N4_M1). As expected, the region where *Npc1* is located (Chr18: 12,189,694-12,2363,86) shows a large region of C57BL/6J heterozygosity (original strain used for CRISPR/Cas9 targeting) linked to the *Npc1*^{em1Pav} allele.

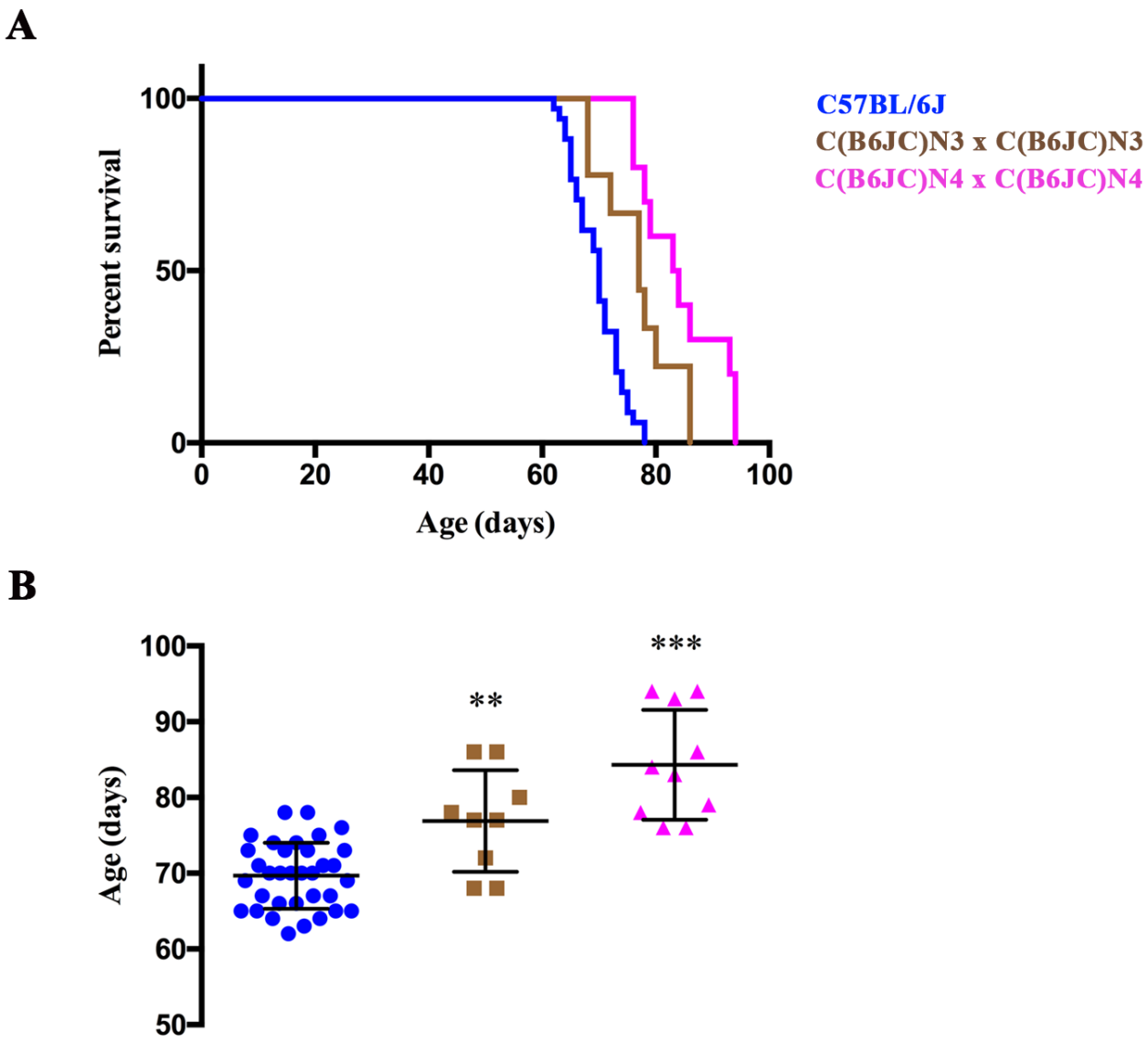


Figure 4.5 Strain-specific lifespan differences in *Npc1*^{em1Pav} mutants. A) Lifespan was measured between *Npc1*^{em1Pav} mutants with different genetic backgrounds. Median survivals: C57BL/6J (blue)= 70 days, N3 intercross (brown)= 77 days, N4 intercross (pink)= 83.5 days. *p<0.0001* **B)** Individual plots. As homozygosity for BALB/cJ increased over generations (N3 & N4), survival was also increased compared to *Npc1*^{em1Pav} mutants with a C57BL/6J genetic background. C57BL/6J (n=34), N3 intercross (n=9), N4 intercross (n=10). ***p<0.001*, ****p<0.0001*.

Breeding strategy and lifespan measurement for the N2 backcross generation:

Based on our results showing strain-specific (C57BL/6J vs. BALB/cJ) differences in NPC survival, we wanted to measure lifespan from a generation with a mixed genetic background between the two strains to facilitate mapping genetic modifiers of lifespan. In order to do this, we used a traditional backcross and measured the lifespan of *Npc1*^{em1Pav} mutants from the N2 backcross generation between the two strains of interest (C57BL/6J and BALB/cJ) (Fig. 4.6). We performed a backcross to C57BL/6J since this was the original strain from the CRISPR/Cas9 founder (Chapter II) and there was an established colony of heterozygous *Npc1*^{em1Pav} females with this genetic background. Lifespan was measured for *Npc1*^{em1Pav} mutants (n=202) in the N2 backcross [B6J(B6JCF1)] generation as described earlier.

When compared to our previously analyzed results, the lifespan of N2 backcross mutants showed a wide range overlapping both with C56BL/6J and BALB/cJ intercrosses (N3 & N4) (Fig. 4.7). The lifespan distribution for the C57BL/6J population (unimodal) ranged from 62 to 78 days while the N2 backcross generation was between 63 to 99 days (multimodal) (Fig. 4.8). These results suggest the presence of multiple genetic modifiers affecting lifespan in *Npc1*^{em1Pav} mutants.

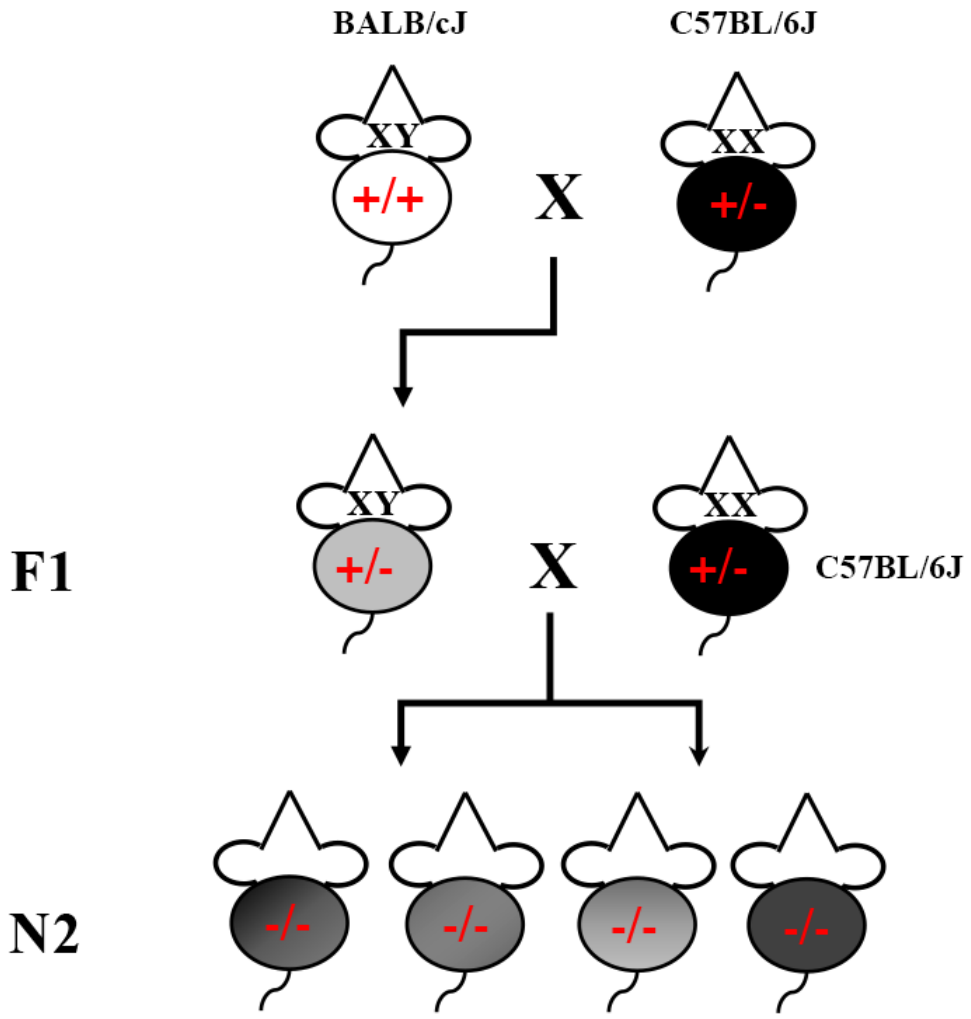


Figure 4.6 Breeding strategy for mapping genetic modifiers of NPC. A heterozygous *Npc1*^{em1Pav} female (C57BL/6J) was crossed to a control (+/+) BALB/cJ male in order to generate a hybrid (F1) heterozygous for variants from both strains. Heterozygous *Npc1*^{em1Pav} males (F1) were selected as breeders and crossed with heterozygous *Npc1*^{em1Pav} females (backcross). Lifespan was measured from homozygote *Npc1*^{em1Pav} mutants (N2 backcross generation) which were subsequently used for QTL analysis.

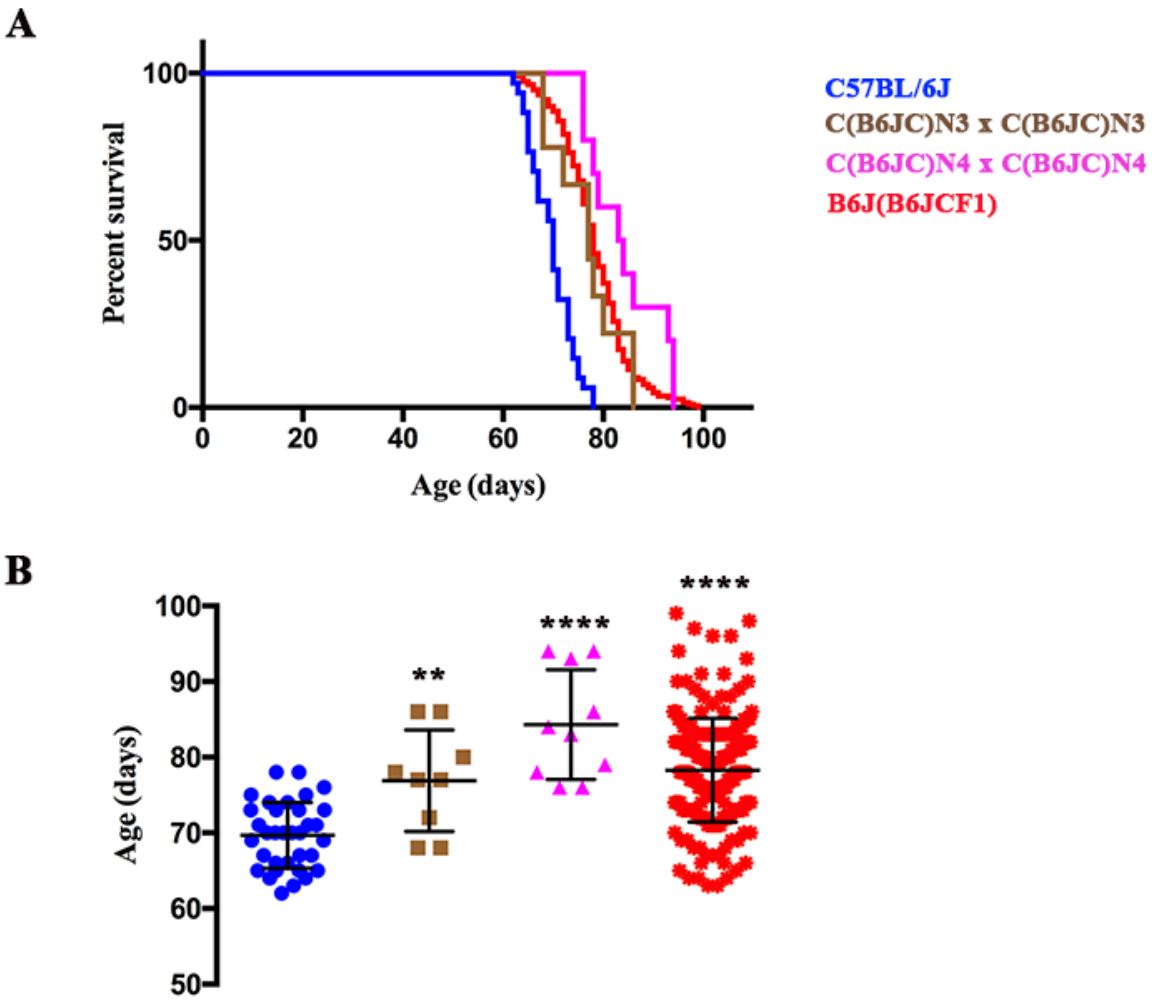


Figure 4.7 The mean lifespan of N2 backcross homozygote mice falls between that of homozygotes on a C57BL/6J or BALB/cJ background. A) Survival comparison between *Npc1*^{em1Pav} mutants from different crosses. Median survivals: C57BL/6J (blue) 70 days, N3 intercross (brown) 77 days, N4 intercross (pink) 83.5 days, N2 backcross (red) 78 days, *p<0.0001.* **B)** Individual plots. The N2 backcross generation [B6J(B6JCF1)] shows a wide range in lifespan (78.29 ± 6.840 days; n=202) spanning the extremes of both the C57BL/6J (69.68 ± 4.36 days; n=34) and the BALB/cJ N3 (76.89 ± 6.69 day; n=9) and N4 (84.30 ± 7.25; n=10) generations. Each dot-plot represents an individual mouse. ***p<0.01*, ****p<0.001*, *****p<0.0001*.

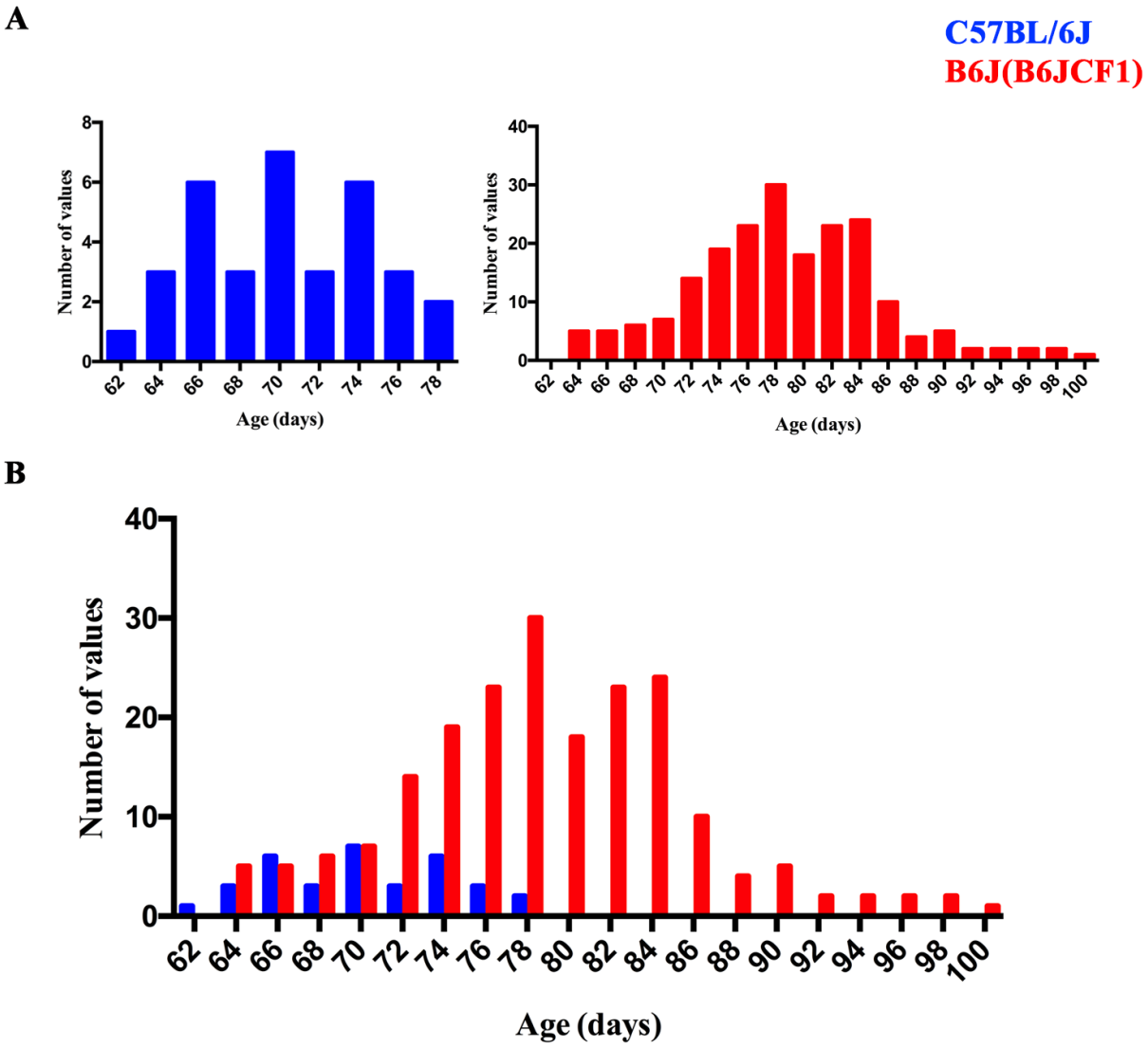


Figure 4.8 Distribution of lifespan in *Npc1*^{em1Pav} mutants. **A)** Frequency distribution of the homozygote lifespan on a C57BL/6J (n=34; blue) or N2 [B6J(B6JCF1)] (n=202; red) genetic background. **B)** Overlap between the two populations shows unimodal distribution for the C57BL/6J population centered at 70 days. In contrast, the N2 backcross generation shows a greater range with a mean located at the high end of the C57BL/6J population (78 days).

C57BL/6N and C57BL/6J have a similar effect on *Npc1*^{em1Pav} mutant lifespan:

As previously mentioned in the introduction, C57BL/6N is considered a sub-strain of C57BL/6. Thus, the number of identified genetic variants that are different between them is limited [103]. If NPC had a different lifespan on a C57BL/6N background compared to C57BL/6J, then only a small number of candidate variants would need to be considered to validate the causative gene(s). Therefore, we used the same backcross breeding strategy as previously described for BALB/cJ to determine if we could also see a difference in survival from the C57BL/6N N2 backcross generation [B6J(B6JB6NF1)]. Figure 4.9 shows that there was no significant difference between *Npc1*^{em1Pav} mutants on a C57BL/6J background compared to a C57BL/6N backcross N2 background. Based on these results, we proceeded to use the C57BL/6J and BALB/cJ N2 backcross samples for QTL mapping knowing that a potentially large number of strain specific variants would need to be considered within any linkage intervals.

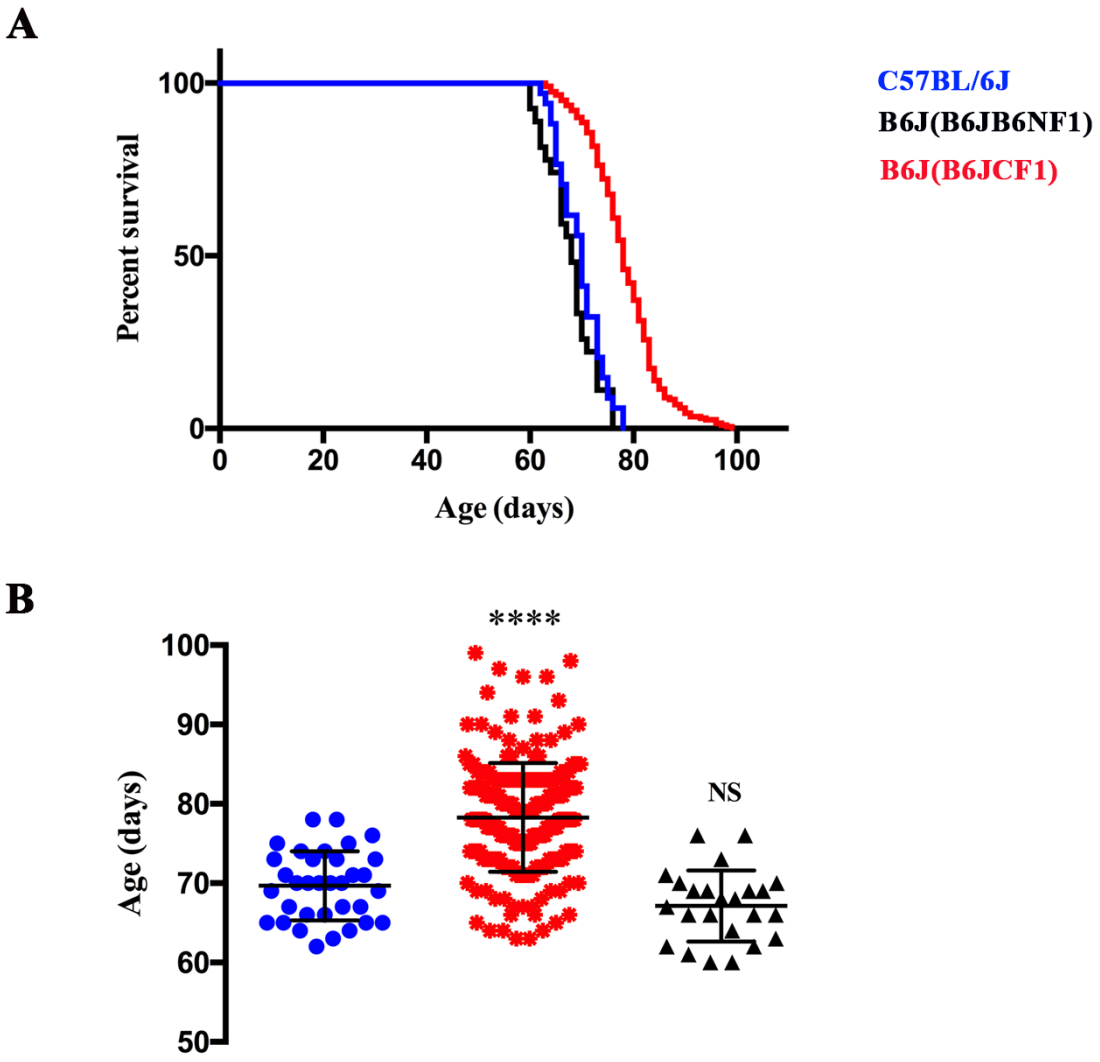


Figure 4.9 Lifespan of N2 backcross generation between C57BL/6J and C57BL/6N. A) Survival comparison between *Npc1*^{em1Pav} mutants from different crosses. Median survivals: C57BL/6J (blue) 70 days, C57BL/6N N2 backcross (black) 68 days p=0.223. The N2 backcross generation using BALB/cJ (red) is shown for comparison. **B)** Individual plots. N2 backcross generation using C57BL/6N (n= 24) compared to C57BL/6J showed no significant difference between the two groups, in contrast to the significant difference shown by the BALB/cJ N2 backcross (shown for comparison) *p<0.0001*. NS= p>0.05, ****$p<0.0001$.

Two QTL loci located on Chromosome 1 and 7 associated with survival in *Npc1*^{em1Pav} mutants:

Genotype results from the BALB/cJ N2 backcross generation (n=202) were analyzed using 28,873 genome-wide SNPs informative between C57BL/6J and BALB/cJ. Lifespan was used as the phenotype for QTL analysis. Linkage results revealed markers associated with significant LOD scores located on chromosome 1 (Marker ID: UNC99871, 40.76 cM; LOD=5.57) and chromosome 7 (Marker ID: UNC13374196, 51.5 cM; LOD=8.91) (Fig. 4.10). When controlling for the effect of each QTL one at a time, we found no evidence of a secondary QTL in the same area nor a change in the effect of the other QTL (Fig. 4.11A). To examine if there was a possible epistatic interaction between the two QTL regions, we separated the N2 backcross samples into four possible genotypes. Figure. 4.11B shows that the effect of the QTL region on chromosome 1 does not depend on the genotype of chromosome 7 and *vice versa* (shown by the pink lines forming a parallelogram), suggesting additivity. This analysis also shows homozygosity for C57BL/6J (B6J/B6J) in chromosome 7 resulted in a shorter lifespan compared with *Npc1*^{em1Pav} heterozygous mutants for BALB/cJ (B6J/C) in the same region. In contrast, chromosome 1 showed the opposite effect, with C57BL/6J homozygosity in this region resulting in longer lifespan. Thus, *Npc1*^{em1Pav} mutants with C57BL/6J homozygosity at chromosome 1 and BALB/cJ and C57BL/6J heterozygosity on chromosome 7 showed the longest lifespan.

In order to find additional QTLs contributing to lifespan differences in *Npc1*^{em1Pav} mutants, we normalized the effects of both QTL regions (chromosome 1 & 7). This analysis identified one additional QTL located on Chromosome 17 (LOD>3) (Fig. 4.12).

In summary, genetic linkage analysis from the backcross N2 generation showed two significant QTL regions associated with lifespan: one located in chromosome 1 and another one in chromosome 7. These two regions showed an additive effect in the survival of *Npc1*^{em1Pav}

mutants. The greatest effect was shown by combining homozygosity for C57BL/6J in the QTL region of chromosome 1 and BALB/cJ and C57BL/6J heterozygosity in the QTL region on chromosome 7. An additional QTL region was also identified on chromosome 17. Based on these results, we conclude that strain-specific survival changes in *Npc1*^{em1Pav} mutants are due to interactions between multiple modifier genes that impact NPC lifespan.

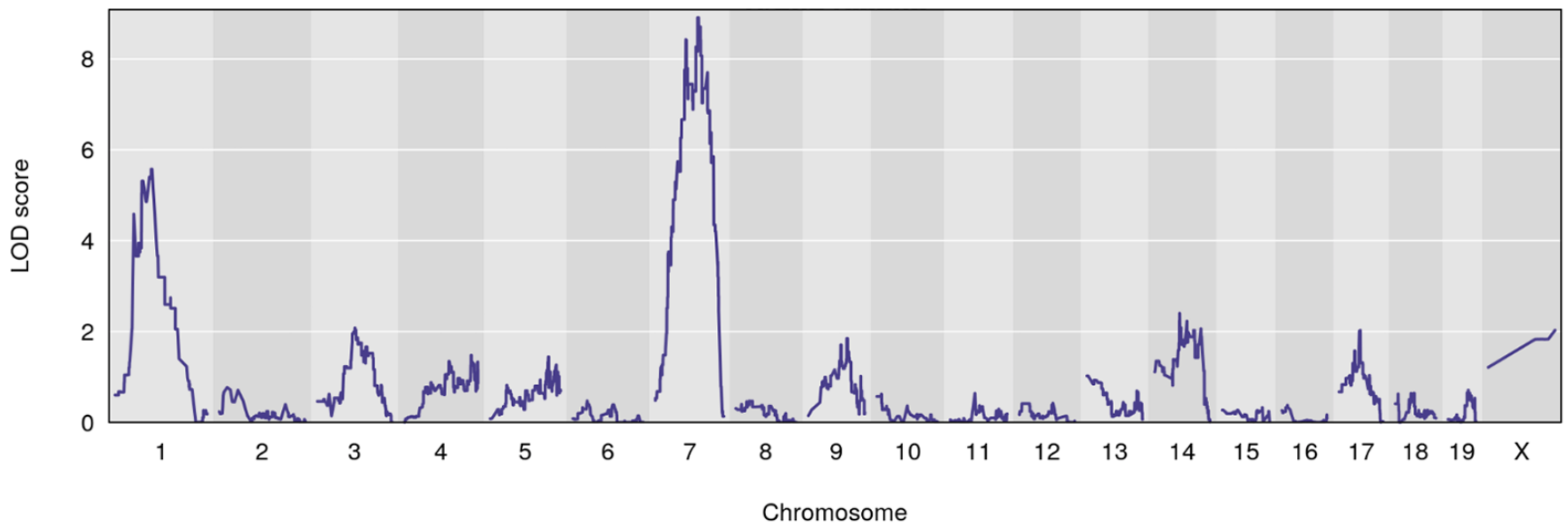


Figure 4.10 Genetic linkage results between lifespan of *Npc1*^{em1Pav} mutants and strain specific-markers for C57BL/6J and BALB/cJ. Genome scan results from N2 backcross generation by individual chromosome locations show areas with a significant LOD score in chromosome 1, marker with the highest score (peak), UNC99871, 40.76 cM; LOD=5.57 and chromosome 7 at UNC13374196, 51.5 cM; LOD= 8.91). Analysis was performed with a 5% significant threshold of LOD>3.09.

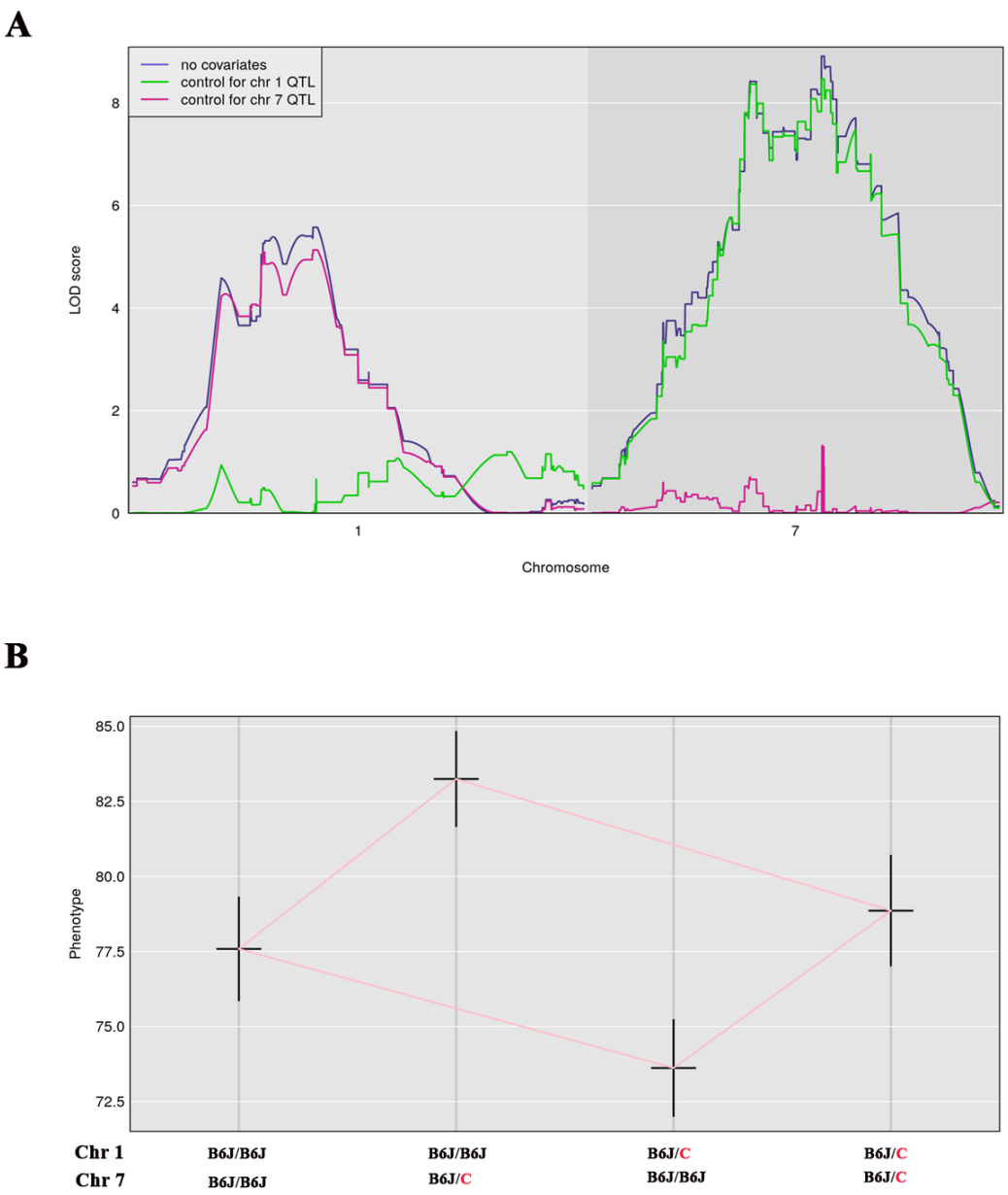


Figure 4.11 Effects and interactions between QTLs (Chromosome 1 & 7). A) When controlling for chromosome 1 (green), no additional QTLs are found within the same chromosome. The same results are shown for chromosome 7 (pink line). **B)** Plot of the estimated effects in each of the four genotype groups, showing the averages ± 2 SEs. The effect of chromosome 1 QTL is similar, regardless of the genotype at the QTL on chromosome 7 (B6J/B6J or B6J/C), and *vice versa* (the shape formed by the pink line segments is very nearly a parallelogram), indicating additivity. B6J=C57BL/6J, C=BALB/cJ.

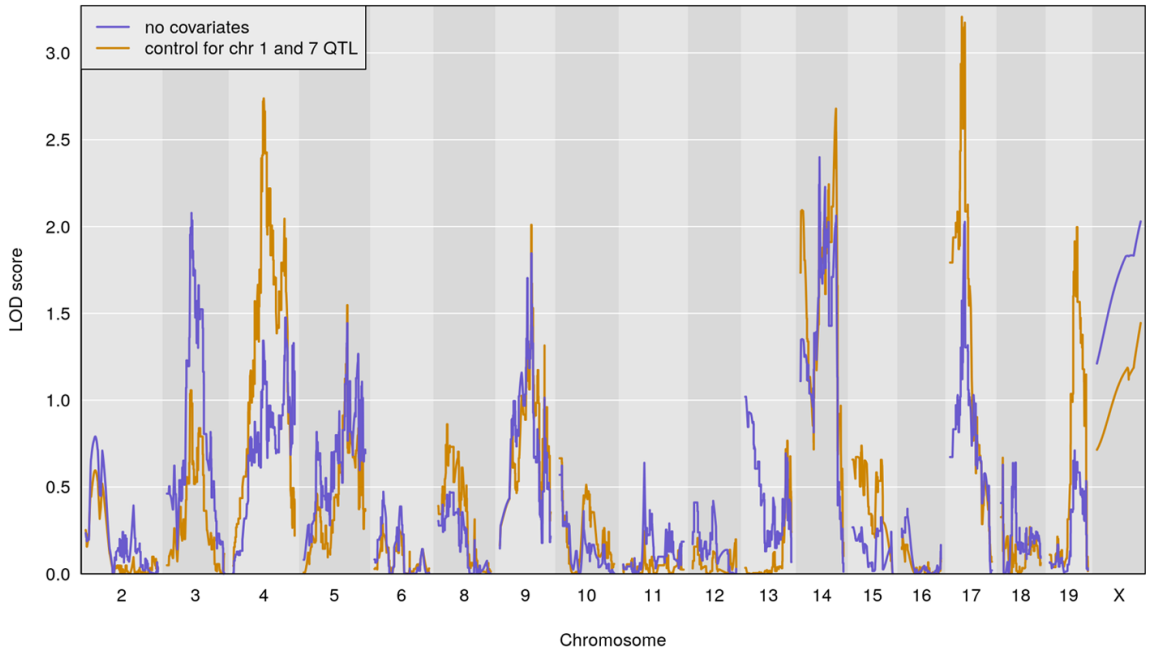


Figure 4.12 An additional QTL on chromosome 17. When controlling for the genotypes of both chromosomes 1 & 7 (orange) there is significant linkage (LOD>3) detected on chromosome 17.

Identifying candidate genetic variants and genes within the QTL regions on chromosome 1 and 7:

In order to establish the boundaries for our regions of interest, we used a region defined by ±1.5 LOD score from the region/marker with the highest score (peak) as a cut-off, as previously recommended [108]. The QTL intervals for chromosomes 1 and 7 were flanked by the following markers: chromosome 1: UNC484527 (17.241 cM; 38,919,200bp) to UNC112857 (45.334 cM; 92,082,500bp) and chromosome 7: UNC12909197 (33.483 cM; 63,988,100bp) to UNCHS020933 (55.703 cM; 117,71000bp). Thus, the two intervals spanned 78.9Mbp for chromosome 1 and 92.6Mbp for chromosome 7.

Next, we used the Mouse Genomes Project (Sanger; Rel1303-GCRm38) and performed a SNP inquiry between C57BL6/J and BALB/cJ filtering for the variants predicted to impact coding sequences as described in Materials & Methods section (Table 4.1). SNPs were then further analyzed for predicted consequences using both PROVEAN and SIFT scores [109,110] (Tables 4.2 to 4.4). A total of 32 candidate variants for chromosome 1 and 36 variants for chromosome 7 were obtained that were classified as deleterious/damaging from both PROVEAN and SIFT scores (Fig. 4.13) These variants spanned 15 and 24 candidate genes in chromosome 1 and 7, respectively (Fig. 4.14 & 4.15).

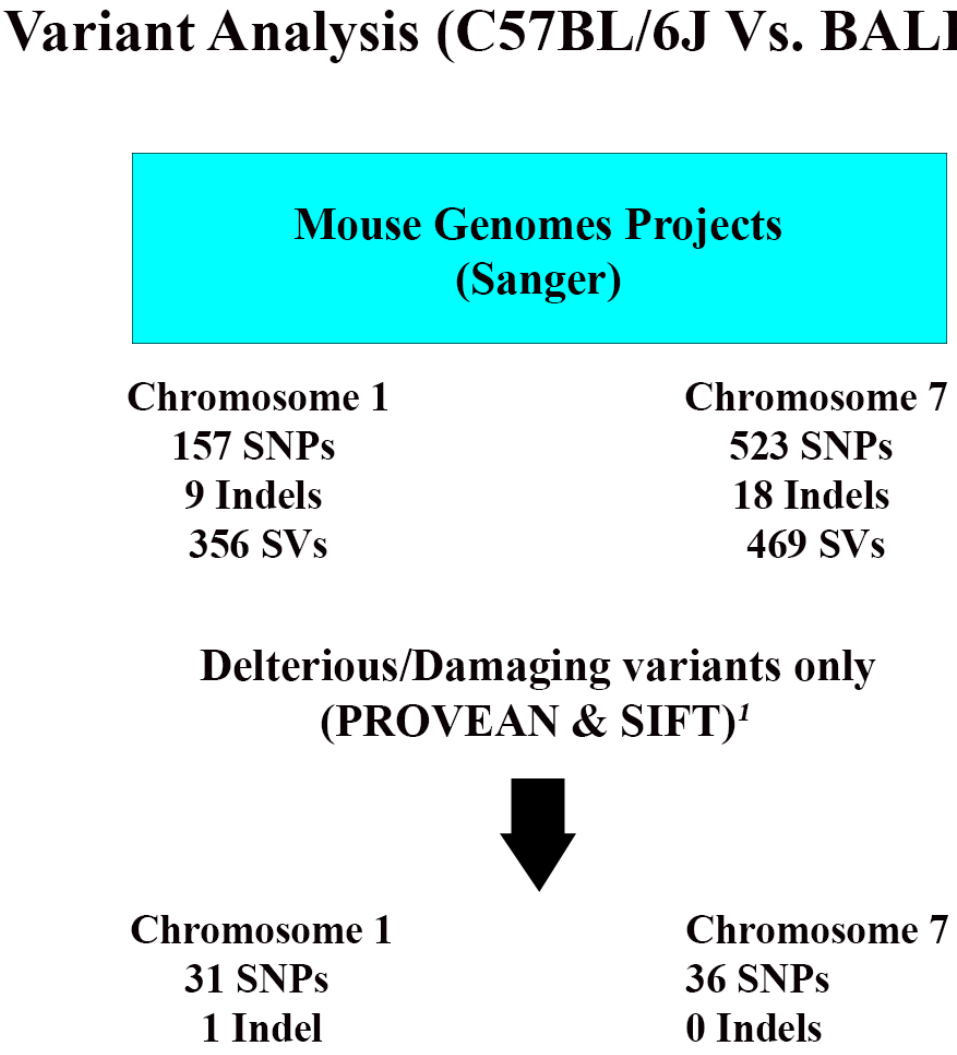


Figure 4.13. Workflow for variant analysis for both QTLs (chromosome 1 & 7). Genetic variants obtained from the Mouse Genomes Project (Sanger Institute) between C57BL/6J and BALB/cJ were obtained for both QTL regions in chromosome 1 & 7. These variants were scored by their predicted protein function using both PROVEAN and SIFT scores. The number of variants shown at the bottom were both scored as deleterious/damaging for both PROVEAN and SIFT scores. Only coding regions were analyzed.

[1]SIFT algorithms are unable to categorize structural variants.

Table. 4.1 Summary of strain-specific genetic variants between C57BL/6J and BALB/cJ retrieved from the Mouse Genomes Project (Sanger)

SNPs

	Missense	*Splice region*	*Splice donor*	*Splice acceptor*	*Stop gained*	*Stop loss*	***Total***
Chromosome 1	116	38	1	1	0	0	156
Chromosome 7	429	85	2	2	3	2	523

Insertions/Deletions

	Splice region	*Splice donor*	*Missense*	***Total***
Chromosome 1	8	1	0	9
Chromosome 7	17	0	1	18

Structural Variants

	Deletion	*Insertion*	*Inversion*	*Complex events*	*Copy number gain*	***Total***
Chromosome 1	211	138	5	1	1	356
Chromosome 7	276	189	0	2	2	469

Table 4.2 List of candidate variants from QTL in chromosome 1 (PROVEAN score)

Gene Symbol	Chr1 location (bp)[1]	dbSNP ID[2]	AA change	PROVEAN Score[3]
Myo1b	51770845	rs33820710	R/W	-3.61
Myo1b	51770845	rs33820710	R/W	-3.81
Myo1b	51770845	rs33820710	R/W	-3.88
Myo1b	51770845	rs33820710	R/W	-3.88
Gm8420	51940777	rs37214932	R/H	-4.61
Gm8420	51940975	rs36835684	R/Q	-3.52
G730003C15Rik	59120170	rs47107794	G/R	-8
G730003C15Rik	59120234	rs215544630	Q/P	-6
Mpp4	59146397	rs37608343	T/M	-3.98
Mpp4	59146397	rs37608343	T/M	-3.85
Mpp4	59146397	rs37608343	T/M	-3.89
Mogat1	78537971	***	T/I	-3.71
Mogat1	78537971	***	T/I	-3.71
Ugt1a6a	88218146	rs47490282	R/S	-3.47
Ugt1a2	88218146	rs47490282	R/S	-3.75
Ugt1a7c	88218146	rs47490282	R/S	-3.57
Ugt1a1	88218146	rs47490282	R/S	-3.58
Ugt1a9	88218146	rs47490282	R/S	-3.29
Ugt1a5	88218146	rs47490282	R/S	-3.64
Ugt1a6a	88218146	rs47490282	R/S	-3.47
Ugt1a6a	88218146	rs47490282	R/S	-3.47
Ugt1a6b	88218146	rs47490282	R/S	-3.47
Ugt1a6b	88218146	rs47490282	R/S	-3.47
Ugt1a8	88218146	rs47490282	R/S	-3.57
Ugt1a10	88218146	rs47490282	R/S	-3.6
Mroh2a	88232324	rs49941474	R/C	-5.9
Mroh2a	88232324	rs49941474	R/C	-5.91
Mroh2a	88235442	rs51702482	R/H	-3.95
Mroh2a	88235442	rs51702482	R/H	-4.02
Mroh2a	88248621	rs50937237	L/F	-3.37
Mroh2a	88248621	rs50937237	L/F	-3.31
Rbm44	91153115	rs47700383	R/G	-2.51
Rbm44	91153385	rs51878992	A/P	-2.62
Rbm44	91153473	rs48720285	T/I	-3.75
Rbm44	91164929	rs51150674	E/G	-3.4
Traf3ip1	91500846	rs47229691	T/M	-2.76
Hdac4	91930104	rs31771459	A/T	-4

Table 4.3 List of candidate variants from QTL in chromosome 1 (SIFT score)

Gene Symbol	Chr1 location (bp)[1]	dbSNP ID[2]	AA change	SIFT Score[3]
Myo1b	51770845	rs33820710	R/W	0.006
Myo1b	51770845	rs33820710	R/W	0.014
Myo1b	51770845	rs33820710	R/W	0.021
Myo1b	51770845	rs33820710	R/W	0.02
Gm8420	51940777	rs37214932	R/H	0.004
Gm8420	51940975	rs36835684	R/Q	0.005
Mpp4	59146397	rs37608343	T/M	0.016
Mpp4	59146397	rs37608343	T/M	0.018
Mpp4	59146397	rs37608343	T/M	0.016
Ugt1a6a	88218146	rs47490282	R/S	0.001
Ugt1a2	88218146	rs47490282	R/S	0.002
Ugt1a7c	88218146	rs47490282	R/S	0.002
Ugt1a1	88218146	rs47490282	R/S	0.002
Ugt1a9	88218146	rs47490282	R/S	0.001
Ugt1a5	88218146	rs47490282	R/S	0.001
Ugt1a6a	88218146	rs47490282	R/S	0.001
Ugt1a6a	88218146	rs47490282	R/S	0.001
Ugt1a6b	88218146	rs47490282	R/S	0.001
Ugt1a6b	88218146	rs47490282	R/S	0.001
Ugt1a8	88218146	rs47490282	R/S	0.002
Ugt1a10	88218146	rs47490282	R/S	0.001
Mroh2a	88232324	rs49941474	R/C	0
Mroh2a	88232324	rs49941474	R/C	0
Mroh2a	88235442	rs51702482	R/H	0.036
Mroh2a	88235442	rs51702482	R/H	0.036
Mroh2a	88248621	rs50937237	L/F	0.006
Mroh2a	88248621	rs50937237	L/F	0.006
Rbm44	91153473	rs48720285	T/I	0.04
Rbm44	91164929	rs51150674	E/G	0.043
Traf3ip1	91500846	rs47229691	T/M	0.022
Gm8420	51940697	rs241958794	S/C	0.002
Gm8420	51941132	rs218371581	Q/E	0.001
Casp8	58824229	rs3022794	A/V	0.046
Casp8	58824229	rs3022794	A/V	0.046
Tmem237	59119707	rs32076693	P/L	0.018
Als2	59170467	rs45938263	S/L	0.012
Als2	59170467	rs45938263	S/L	0.012

Table 4.3 Continued from previous page

Gene Symbol	Chr1 location (bp)[1]	dbSNP ID[2]	AA change	SIFT Score[3]
Carf	60109225	rs265545046	R/W	0.001
Carf	60109225	rs265545046	R/W	0.001
Ugt1a1	88212392	rs46698966	H/Y	0.019
Mroh2a	88240149	rs48472294	A/V	0.016
Mroh2a	88240149	rs48472294	A/V	0.016
Lrrfip1	91115186	rs30758374	E/K	0.008
Lrrfip1	91115352	rs13468217	P/L	0.001
Lrrfip1	91115366	rs13468220	A/T	0.008
Lrrfip1	91115378	rs13468216	P/A	0.013
Lrrfip1	91115900	rs50809069	E/Q	0
Lrrfip1	91115920	rs240300165	Q/H	0.001
Lrrfip1	91115934	rs48118798	A/E	0.001
Asb1	91540832	rs262615334	G/D	0.032

[1]Genome build: GRCm38/mm10
[2] Duplicated dbSNP IDs are due to one SNP impacting multiple transcripts.
[3] Only deleterious/damaging variants are shown (PROVEAN Score cutoff <-2.5, SIFT <0.05)
*** Not available

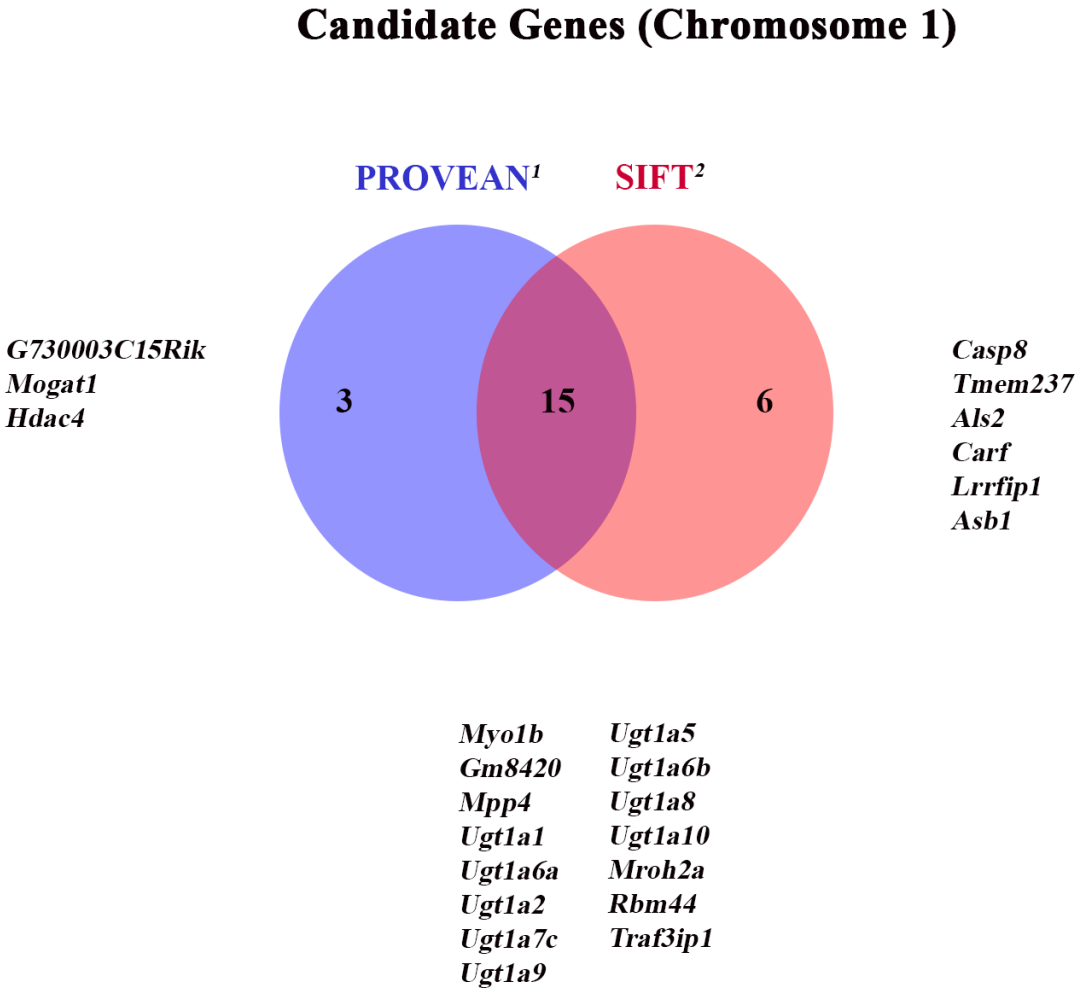


Figure 4.14. Candidate genes from damaging/deleterious variants located on chromosome 1. A total of 15 candidate genes (intersection) have both deleterious PROVEAN (blue circle) and damaging SIFT (red circle) scores.

Table 4.4 List of candidate variants from QTL on chromosome 7 (PROVEAN score)

Gene symbol	Chr7 location (bp)[1]	dbSNP ID[2]	AA change	PROVEAN Score[3]
Gm10974	66386302	***	T/R	-6
Gm10974	66386308	***	T/R	-6
Synm	67735410	rs37590652	P/S	-3.8
Synm	67735410	rs37590652	P/S	-4.22
A830073O21Rik	73740522	rs13470811	W/G	-13
9330171B17Rik	79711040	rs50900959	R/K	-3
Unc45a	80329025	rs32045096	P/L	-3.21
Crtc3	80605815	rs32475809	P/L	-3.66
Slc28a1	81126219	rs49575399	V/A	-3.68
Slc28a1	81126219	rs49575399	V/A	-3.68
3110040N11Rik	81786157	rs13470874	E/Q	-2.59
A530021J07Rik	83148663	rs51433812	D/G	-7
Vmn2r74	85952706	rs32515334	T/A	-3.01
Olfr297	86527184	rs51987439	M/I	-3.64
Tyr	87493043	rs31191169	C/S	-9.54
Gm9934	93079925	rs32299346	H/L	-5.5
Gm9934	93080156	rs31093296	V/D	-7
Gm9966	95958669	rs31480902	H/D	-9
Gm9966	95958777	rs31481725	A/T	-4
Gm9966	95958858	rs6184441	T/A	-5
Gucy2d	98443851	rs31487759	N/S	-4.26
A630091E08Rik	98543945	rs45930425	H/Q	-8
Olfr552	102604533	rs31272864	P/T	-7.44
Olfr566	102856376	rs226082030	S/N	-2.72
Olfr573-ps1	102941735	rs45658471	P/T	-7.8
Olfr573-ps1	102941764	rs48355779	L/P	-5.56
Olfr573-ps1	102942088	rs32023793	P/R	-4.2
Olfr573-ps1	102942187	rs31187061	S/F	-3.63
Olfr592	103186733	rs13479437	G/V	-8.06
Olfr592	103186733	rs13479437	G/V	-8.06
Olfr597	103320869	rs48774455	R/G	-6.63
Olfr597	103320869	rs48774455	R/G	-6.63
Olfr605	103442570	rs36399940	M/I	-3.9
Olfr608	103470113	rs47878607	H/Y	-4.96
Olfr609	103491967	rs47449309	R/C	-3.6
Olfr611	103517928	rs46654534	V/G	-4.29

Table 4.4 Continued from previous page

Gene Symbol	Chr7 location (bp)[1]	dbSNP ID[2]	AA change	PROVEAN Score[3]
Olfr611	103518013	rs49727287	R/W	-7.74
Olfr616	103564887	rs31658137	P/S	-7.94
Olfr620	103611997	rs31212976	A/T	-2.81
Olfr625-ps1	103683111	rs46507835	A/V	-3.95
Olfr69	103767894	rs31230898	R/C	-6.54
Olfr69	103767894	rs31230898	R/C	-6.54
Olfr66	103881449	rs260303701	H/N	-4.27
Olfr66	103881577	rs3704489	T/K	-3.54
Olfr64	103892941	rs256112789	H/N	-4.17
Trim6	104228351	rs31279657	Q/R	-2.63
Trim6	104228351	rs31279657	Q/R	-2.63
Trim12c	104347976	rs13479442	H/Q	-6.53
Trim12c	104347976	rs13479442	H/Q	-7.41
Trim30b	104357269	rs238022483	P/T	-4.41
Trim30b	104357376	rs232998358	M/T	-3.46
Trim30b	104357568	***	I/T	-3.96
Trim30b	104357583	***	L/R	-5.67
Trim30b	104363706	rs235264603	W/S	-12.24
Trim30b	104363706	rs235264603	W/S	-7.09
Olfr652	104564437	rs49472235	A/D	-4.5
Olfr652	104564437	rs49472235	A/D	-4.5
Olfr655	104596555	rs13479443	D/N	-4.94
Olfr698	106752668	rs48391359	T/I	-5.6

[1]Genome build: GRCm38/mm10
[2] Duplicated dbSNP IDs are due to one SNP impacting multiple transcripts.
[3] Only deleterious/damaging variants are shown (PROVEAN Score cutoff <-2.5, SIFT <0.05)
*** Not available

Table 4.5 List of candidate variants from QTL on chromosome 7 (SIFT score)

Gene Symbol	Chr7 location (bp)[1]	dbSNP ID[2]	AA change	SIFT Score[3]
Synm	67735410	rs37590652	P/S	2.97
Unc45a	80329025	rs32045096	P/L	3.5
3110040N11Rik	81786157	rs13470874	E/Q	2.85
Olfr297	86527184	rs51987439	M/I	2.76
Tyr	87493043	rs31191169	C/S	2.79
Gucy2d	98443851	rs31487759	N/S	2.83
Olfr552	102604533	rs31272864	P/T	2.9
Olfr566	102856376	rs226082030	S/N	2.9
Olfr573-ps1	102941735	rs45658471	P/T	2.92
Olfr573-ps1	102941764	rs48355779	L/P	2.92
Olfr573-ps1	102942088	rs32023793	P/R	2.92
Olfr573-ps1	102942187	rs31187061	S/F	2.92
Olfr592	103186733	rs13479437	G/V	3.19
Olfr592	103186733	rs13479437	G/V	3.19
Olfr597	103320869	rs48774455	R/G	2.92
Olfr597	103320869	rs48774455	R/G	2.95
Olfr605	103442570	rs36399940	M/I	2.96
Olfr608	103470113	rs47878607	H/Y	2.92
Olfr609	103491967	rs47449309	R/C	2.84
Olfr611	103518013	rs49727287	R/W	2.84
Olfr616	103564887	rs31658137	P/S	2.84
Olfr625-ps1	103683111	rs46507835	A/V	2.99
Olfr69	103767894	rs31230898	R/C	2.96
Olfr69	103767894	rs31230898	R/C	2.96
Olfr66	103881577	rs3704489	T/K	2.98
Trim12c	104347976	rs13479442	H/Q	2.82
Trim12c	104347976	rs13479442	H/Q	2.8
Trim30b	104357269	rs238022483	P/T	3.22
Trim30b	104357376	rs232998358	M/T	3.12
Trim30b	104357568	rs387877122	I/T	3.12
Trim30b	104357583	***	L/R	3.12
Trim30b	104363706	rs235264603	W/S	2.8
Trim30b	104363706	rs235264603	W/S	2.85
Olfr652	104564437	rs49472235	A/D	2.96
Olfr652	104564437	rs49472235	A/D	2.97
Olfr655	104596555	rs13479443	D/N	2.86

Table 4.5 Continued from previous page

Gene Symbol	Chr7 location (bp)[1]	dbSNP ID[2]	AA change	SIFT Score[3]
Olfr698	106752668	rs48391359	T/I	2.84
Ticrr	79694677	rs32245103	G/D	3.64
Blm	80502586	rs8248433	V/M	3.49
Blm	80502586	rs8248433	V/M	3.5
Crtc3	80595808	rs263953509	T/M	4.32
Crtc3	80605815	rs32475809	P/L	2.9
Zfp592	81029509	rs48393927	I/V	2.83
Alpk3	81092427	rs241844687	T/K	3.93
Vmn2r66	85006874	rs31145000	I/M	2.77
Vmn2r66	85007780	rs32390969	I/T	2.77
Vmn2r67	85155856	rs31962674	M/T	2.78
Vmn2r68	85237658	***	M/T	2.77
Myo7a	98091054	rs47996688	I/V	2.85
Myo7a	98091054	rs47996688	I/V	2.85
Myo7a	98091054	rs47996688	I/V	2.87
Plekhb1	100645652	rs31050068	R/H	3.22
Arhgef17	100931423	rs31826724	C/F	4.32
Numa1	101998679	rs31836421	A/V	3.3
Olfr549	102555231	rs48094146	C/R	3.53
Olfr613	103552060	rs48607273	D/N	2.79
Olfr629	103740826	rs48565329	T/M	2.9
Hbb-bs	103827815	***	A/S	3.91
Hbb-bh2	103839224	***	S/N	3.73
Hbb-bh2	103840096	***	H/N	3.73
Hbb-bh2	103840111	***	S/P	3.73
Hbb-bh2	103840162	***	L/M	3.73
Olfr66	103881970	rs51907985	A/V	2.98
Ubqlnl	104149022	rs13479441	G/R	2.83
Trim30b	104356896	rs241369322	N/T	3.37
Trim30b	104358509	rs49115340	K/N	2.8
Trim30b	104362921	rs31933093	S/N	2.8
Trim30c	104382387	rs47054326	H/R	2.79
Usp17le	104768417	rs13479444	T/M	3.01
Olfr714	107074254	rs31980856	R/H	2.88

[1]Genome build: GRCm38/mm10
[2] Duplicated dbSNP IDs are due to one SNP impacting multiple transcripts.
[3] Only deleterious/damaging variants are shown (PROVEAN Score cutoff <-2.5, SIFT <0.05)
*** Not available

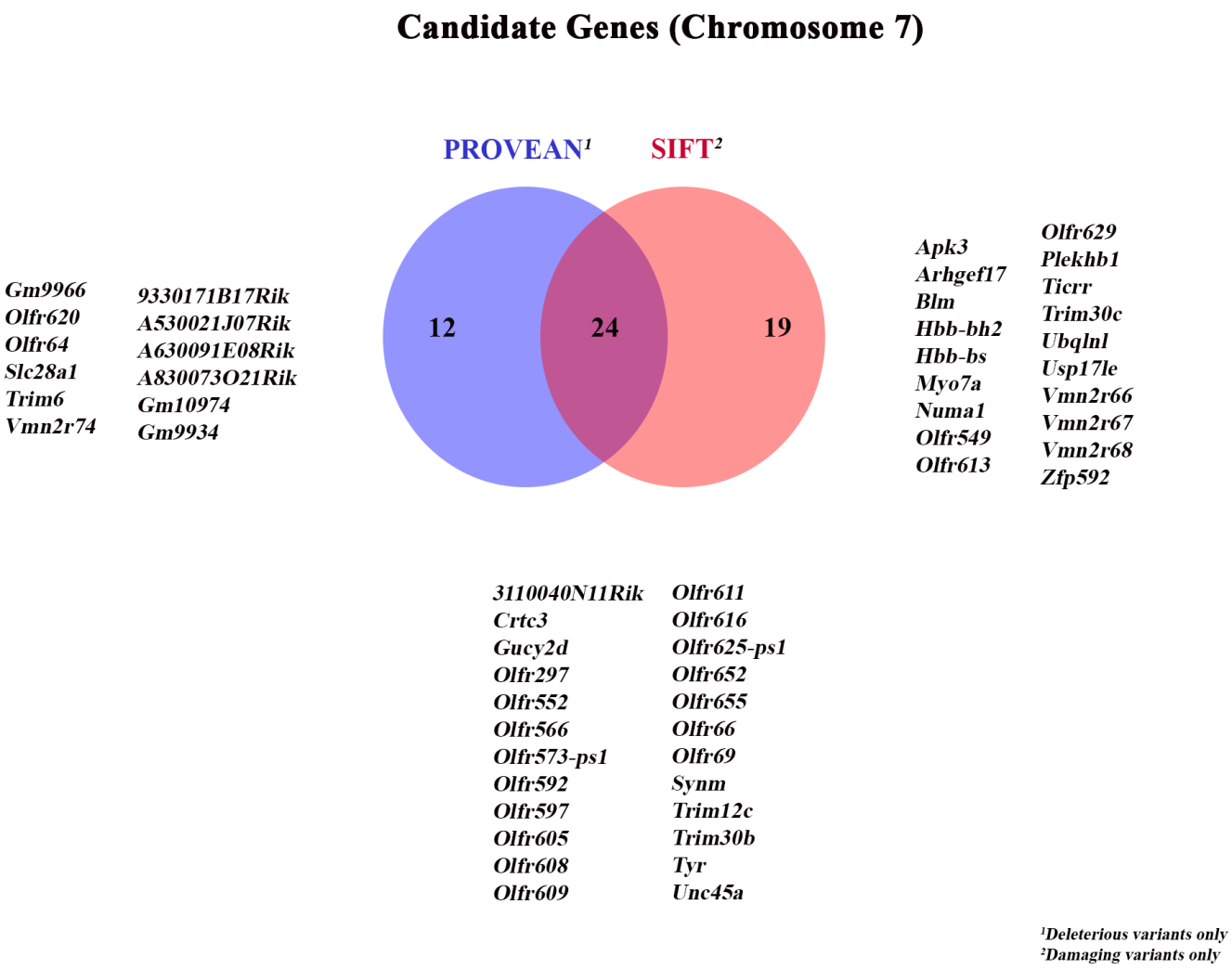


Figure 4.15. Candidate genes from damaging/deleterious variants located on chromosome 7. A total of 24 candidate genes (intersection) have both deleterious PROVEAN (blue circle) and damaging SIFT (red circle) scores.

Severity of visceral pathology in *Npc1*^{em1Pav} mutants is modified by genetic background.

To determine if the severity of other phenotypes associated with NPC were also affected by changes in genetic background, we analyzed the presence of foam cells in the liver of *Npc1*^{em1Pav} mutants as previously described in Chapter III (Fig. 3.4 & 3.5).

We hypothesized that similar to lifespan, a more severe phenotype, in this case a greater accumulation of CD68(+) foam cells would be present in *Npc1*^{em1Pav} mutants with a C57BL/6J genetic background. Liver tissues from age-matched *Npc1*^{em1Pav} mutants (P21) with either a C57BL/6J genetic background or a BALB/cJ (N6 intercross) background were analyzed for the presence of CD68(+) signal. Figure 4.16A shows accumulation of foam cells was significantly greater in *Npc1*^{em1Pav} mutants with a C57BL/6J genetic background vs. a BALB/cJ, CB6J(B6JC)N6 x C(B6JC)N6 background . Quantification of percentage area of CD68(+) signal (brown) in multiple *Npc1*^{em1Pav} mutants confirmed that a more severe storage phenotype was present in *Npc1*^{em1Pav} mutants with a C57BL/6J genetic background (Fig. 4.16 B). These results indicated that underlying cellular pathologies such as immune-mediated responses due to lipid accumulation are dependent on strain-specific changes. Furthermore, these cellular processes could have an impact on lifespan thus supporting our results of differences in survival between the two strains in the context of NPC.

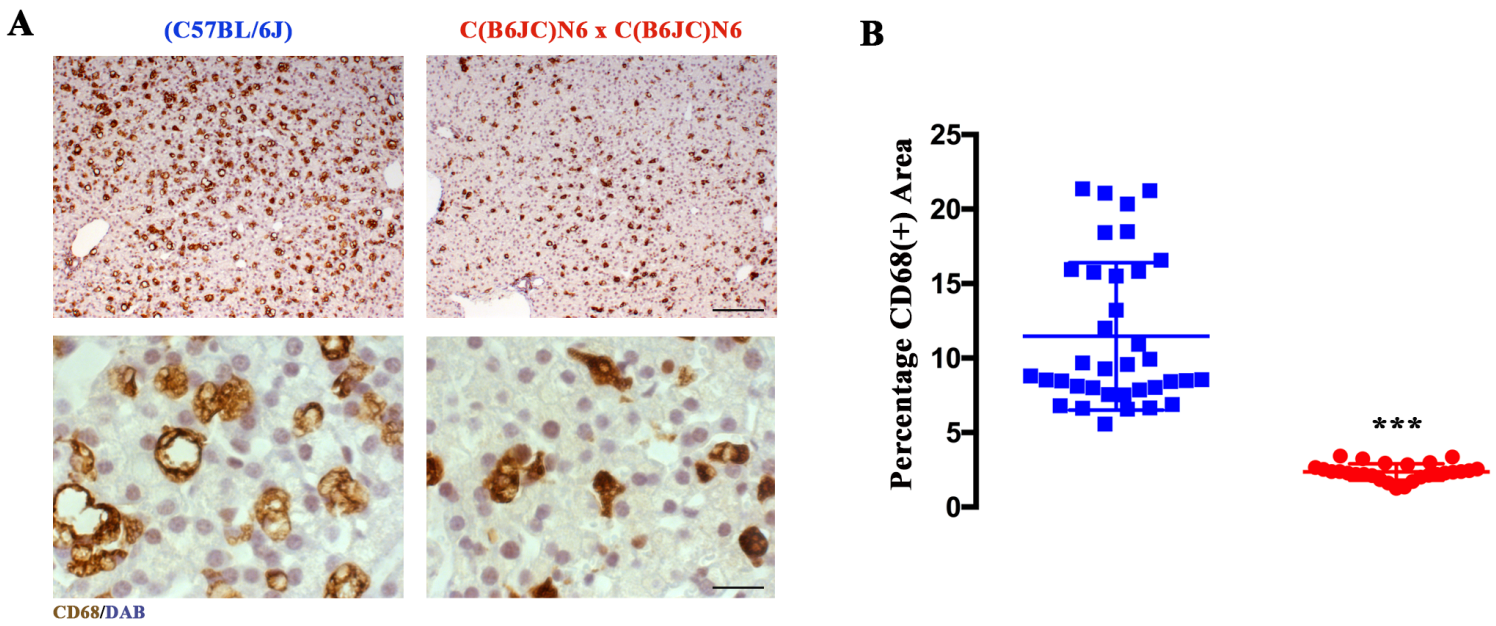


Figure 4.16 Visceral pathology in *Npc1*^{em1Pav} mutants varies with genetic background. A) Liver tissues from age-matched *Npc1*^{em1Pav} mutants (P21) on a C57BL6/J genetic background (blue) or a BALB/cJ (N6 intercross) genetic background (red). Tissues were stained with anti-CD68 (brown), a macrophage marker. *Npc1*^{em1Pav} mutants on a C57BL6/J genetic background showed a greater accumulation of foam cells compared to *Npc1*^{em1Pav} mutants with a BALB/cJ (N6 intercross) genetic background. Foam cells appeared bigger in size due to lipid storage (bottom row). **B)** Quantification of CD68(+) signal showed a significant difference between the two groups ($p<0.0001$). Each dot represents the averaged count and nine counts were performed for each animal. C57BL/6J (n=4), BALB/cJ (n=3). Top scalebar equals 200µm. Bottom scale bar equals 10µm.

Discussion

With new advances in human genome sequencing technology, many causative genes have been identified in Mendelian disorders [111]. In many cases, phenotypic variation still exists even when accounting for the "causative" gene, thus casting doubt whether these cases are truly monogenic diseases [74,112]. The discovery of genetic modifiers has uncovered important pathogenic pathways leading to new diagnostic and treatment approaches in many of these disorders [74,112]. For rare diseases such as NPC, using model organisms has been essential to this process [96,113]. Current NPC mouse models have been able to recapitulate many of the hallmarks of the natural history of the disease as presented by NPC patients [59,61,62]. Previous evidence has shown strain-specific differences in survival [62,78,80] and disease onset [79]. While these results suggest there is a genetic component responsible for these phenotypic variations, the identification of these modifier genes is still unknown. Consequently, our goal was to discover genetic modifiers of NPC by using naturally-occurring genetic differences found in different mouse strains.

In order to do this, we generated the first NPC mouse model harboring an in-frame deletion by using CRISPR/Cas9: *Npc1*^{em1Pav} (Chapter II). This new hypomorphic allele was created on a C57BL/6J genetic background allowing us to compare survival differences between this strain and others such as BALB/cJ and C57BL/6N. By using marker-assisted speed congenics we were able to quickly establish *Npc1*^{em1Pav} mutants with a greater percentage of BALB/cJ homozygosity and showed that this strain is associated with a longer lifespan when compared to C57BL/6J. We then measured the lifespan from a genetically mixed N2 backcross generation (B6J(B6JCF1)) and observed a multimodal distribution suggesting the presence of multiple modifier genes. At the same time, we performed a similar analysis using C57BL/6N, a sub-strain of C57BL/6J, and showed there were no differences in lifespan between the two strains.

In order to identify genetic modifiers, we performed QTL analysis from N2 backcross *Npc1*^{em1Pav} mutants between C57BL/6J and BALB/cJ (n=202) using lifespan as a quantitative trait. Our results showed two significant QTLs located on chromosome 1 (LOD=5.57) and chromosome 7 (LOD=8.91). Further analysis revealed an additive effect on lifespan between these two regions, weakening the argument of a possible epistatic interaction. An additional QTL region was also identified in chromosome 17 (LOD>3) when controlling for the effects of chromosome 1 and 7. These results differ from the ones previously published by Zhang and colleagues [79]. In this study, the authors used the age of onset of tremor as their phenotype in *Npc1* mutant mice from a mixed (BALB/cJ and DBA2/J) N2 generation with a smaller sample size (N=82). Linkage analysis detected weak linkage on chromosome 19 (LOD=2.24). The differences between QTL regions on our study and the results from Zhang and colleagues [79] could be due to different phenotypes measured (age of onset vs. lifespan) and also the different genetic strains used. Nevertheless, these previously published results suggested, as in our case, the presence of multiple genetic modifiers based on the distribution of the N2 generation. Thus, to our knowledge, our results are the first to identify genomic regions in *Npc1* mutant mice having potential modifier variants associated with changes in lifespan. We also showed these genetic modifiers can have independent effects as well as interact with each other in a synergistic fashion.

Our analysis suggests heterozygosity for BALB/cJ in the chromosome 7 QTL will result in increased lifespan. This phenomenon fits in part with previous reports showing a BALBc/J genetic background increases lifespan in both Npc1^{nih} and Npc1^{I1061T} mice compared to C57BL/6J mutants [62,80]. Interestingly, we showed C57BL/6J homozygosity on chromosome 1 also contributes to increased survival. Furthermore, we also identified another potential QTL on

chromosome 17. These results underscore the complexity and multifactorial nature of the genetic architecture of NPC.

In order to generate a list of candidate genes, we obtained strain-specific genetic variants between C57BL/6J and BALB/cJ. By using two different algorithm scores for predicting protein function (PROVEAN and SIFT) we selected the most deleterious and damaging genetic variants as candidates for validation (Figures 4.14 & 4.15).

For example, in the QTL region of chromosome 1 several genes were identified such as the genes belonging to the *Ugt1* family. These genes are known to be key enzymes in the metabolism of Phase II drugs as well as endogenous substances such as bilirubin [114]. Expression of these genes has been mainly found in the liver, small intestine and kidneys, although recent studies have shown expression in different parts of the brain such as the cerebellum [115]. Clinically, mutations in the UGT1A1 gene are known to be responsible for accumulation of unconjugated bilirubin. This results in a range of clinical presentations from mild disorders such as Gilbert's syndrome [116] to more severe disorders like Crigler-Najjar syndrome, seen in neonates [117]. Previous studies have also shown strain-specific differences in enzyme activity for these genes [118], reporting C57BL/6J as having a significantly lower enzymatic activity than BALB/cJ in the small intestine (duodenum). In the case of NPC, several *Ugt*-family genes have been shown to be significantly reduced in *Npc1* mutants ($Npc1^{nih}$) including one of our candidates: *Ugt1a9* [119]. Another candidate gene identified in chromosome 1: *Myo1b* (MGI ID:107752) is part of the myosin motor protein family (Class I) [120]. These proteins have been well-studied in terms of their motor function in muscles. Recent studies suggest they are also involved in the immune response [121] Interestingly, Myo1b has been associated with vesicular trafficking localizing to multivesicular sorting bodies, endosomes

and lysosomes which may have a relevance to trafficking in NPC. [122,123]. Myo1b is also expressed in neurons and regulates axon formation [124].

We were also able to identify a number of candidate genes from the QTL region located in chromosome 7. Major strain-specific metabolic differences have been characterized between C57BL/6J and BALB/cJ [125]. In general, C57BL/6J mice are more susceptible to obesity and metabolic syndrome-related phenotypes [125]. One of our candidate genes: *Crtc3* (MGI: 1917711), is associated with obesity in both mice [126] and humans [126,127]. In fact, characterization of the mouse null allele (*Crtc3*$^{-/-}$) showed mutant mice are resistant to obesity [126]. This is partly due to higher sensitivity to insulin, a faster metabolic rate and a greater susceptibility to beta-adrenergic receptor signaling. *Crtc3*$^{-/-}$ mice also showed decreased fatty acid levels in their livers resulting in a protective effect against hepatic steatosis. This gene also plays a role in the production of regulatory macrophages, which have an essential role in the anti-inflammatory immune response [128-130].

NPC is characterized by accumulation of lipids in visceral organs such as the liver [14]. Early-onset NPC patients typically present with hepatomegaly, which could range from a transient presentation to liver failure [26]. The reasons of why this phenotype is only present in a subset of patients is still unknown, and it is a major contributor to the heterogeneity of NPC clinical presentation. A number of metabolic dysfunctions have also been reported in NPC patients, such as: decreased levels of total cholesterol and elevated triglycerides compared to healthy controls [131]. When analyzing obesity risk, decreased NPC1 function (haploinsufficiency) has also been associated with obesity in both mice [132,133] and humans [134]. These results suggest an underlying metabolic dysfunction as part of NPC pathophysiology. Interestingly, these metabolic differences in the context of decreased NPC1 are shown to be strain-specific [132,135].

C57BL6/J *Npc1*$^{+/-}$ mice on a low-fat diet showed glucose intolerance compared with BALB/cJ *Npc1*$^{+/-}$ mice independent of body weight.

Our results in the chromosome 7 region showed increased survival was associated with heterozygosity of BALB/cJ. Thus, we can hypothesize that the potential genetic modifier located in this region could have an effect with a single BALB/cJ allele being sufficient to improve lifespan. Interestingly, *Crtc3*$^{+/-}$ mice showed an intermediate phenotype [126] fitting with our model. Based on this information we can speculate that *Crtc3* as a metabolic and immune regulator may play a role in the visceral pathology of NPC by having a protective effect in BALB/cJ *Npc1*^{em1Pav} resulting in increased survival. Furthermore, as we showed strain-specific differences based on the severity of visceral pathology this could also fit with our hypothesis. Further validation will be needed in order to support this idea.

Strengths and limitations:

Our results show that an underlying genetic component contributes to part of the phenotypic variation in survival in *Npc1* mutant mice. By using a new *Npc1* mouse model, *Npc1*^{em1Pav}, we were able to quickly assess strain-specific differences found in *Npc1*^{em1Pav} mutants. In general, sample size is considered one of the main limiting factors when conducting QTL analysis. While we believe that additional QTL regions could potentially be identified with a greater sample size, the number of *Npc1*^{em1Pav} mutants from the N2 generation (n=202) in this study is significantly larger than previous studies attempting to map genetic modifiers in NPC (n=82) [79]. These promising results also have a number of limitations. For example, in our candidate gene analysis for genetic modifiers we only included coding regions. During the past few years we have learned non-coding regions play an important regulatory role in the genome [136]. We hope that

as new technological advances are developed in predicting consequences from non-coding variants, future studies will be able to dissect further their role in phenotypic variance.

Future work.

In order to identify modifier genes in both QTLs located on chromosome 1 and 7, we will validate our candidate variants by taking different approaches. For example: we can analyze the predicted deleterious effects of these variants at the mRNA level between C57BL/6J and BALB/cJ. One challenge in this approach is the fact that NPC is a multisystemic disease and changes in survival could be due to effects from multiple organ systems. Thus, tissue-specific expression analysis could limit our results. However, we will prioritize genes expressed in known NPC affected organs such as the brain, liver, spleen and lungs as we have shown strain-specific differences in the accumulation of foam cells in the liver. An alternative approach would be to further define the linkage region by fine-mapping. This could be accomplished by using established consomic strains (inbred strain containing a single chromosome from another strain: https://www.jax.org/research-and-faculty/resources/special-mouse-strains-resource) or by selecting for these two regions in our *Npc1*^{em1Pav} mutants. For example, by repeatedly backcrossing to C57BL6/J we can selectively retain BALB/cJ heterozygosity in our candidate region of chromosome 7 while the rest of their genome would be homozygous for C57BL/6J. This will allow us to narrow down the region and reduce the number of candidate genes. Ultimately the most promising candidates will be tested *in-vivo* by using CRISPR/Cas9 to generate mutant mouse strains for each candidate. These variants can be introduced separately in *Npc1*^{em1Pav} mutant alleles as their phenotypic effect on survival can be characterized. We also hope to combine these results with other datasets generated from NPC patients (see Chapter VI) in order to translate them to the clinic.

Chapter V: Characterizing Neonatal Lethality in *Npc1^{em1Pav}*

Introduction

As previously mentioned in Chapter I, Niemann-Pick Disease Type C has an extremely variable clinical presentation [14,137]. The age of onset also ranges from *in-utero* to well into adulthood [14,27]. While most of the literature has described the most common ages of onset: infantile and juvenile, very few studies have been focused on the pre/perinatal cases [27]. NPC patients suffering from this earlier presentation are characterized by more visceral clinical findings such as splenomegaly and/or hepatomegaly as well as ascites [138,139]. In fact, the presence of isolated fetal splenomegaly has been described as a strong predictor of NPC diagnosis [140]. This is in contrast to the classical neurodegenerative symptoms shown by later onset patients. Based on the very few cases described, the outcome for fetal/neonatal NPC is very poor with patients dying from cholestatic liver disease within the first few weeks after birth [14]. Most recently, several reports have also described respiratory complications as the main cause of mortality in NPC1 neonatal patients [28,29].

During the introductory chapter (Chapter I), we also described a number of current mouse models originated in order to study NPC. While these models are able to recapitulate features seen in infantile and adult onset patients [49], there is a need for additional animal models in order to study the more severe pre/perinatal presentation of NPC. In this chapter, we characterize for the first time a novel neonatal lethality phenotype associated with NPC by using our new mouse model: *Npc1^{em1Pav}*. In addition, we also show there is a potential genetic component related to this lethality seen in *Npc1^{em1Pav}* mutants shortly after birth.

Materials and Methods

Mouse Genetic Strains and *Npc1* Alleles.

BALB/cJ, FBV/NJ and C57BL/6J control mice were imported from Jackson Laboratories (ME, USA). B6.C-*Npc1*^{m1N}/GarvJ was imported directly from the University of New Mexico (Dr. William S. Garver). Currently, they are available at Jackson Laboratories (stock number: 030097). These mice were backcrossed from their original strain (BALB/cNctr) to C57BL/6J for over thirty generations prior to import (personal communication). BALB/cNctr-*Npc1*^{m1N}/J (stock number: 003092) was imported from Jackson Laboratories. B6.129-*Npc1*^{tm1Dso}/J (I1061T allele) was imported directly from Washington University School of Medicine in St. Louis (Dr. Daniel S. Ory), currently deposited in Jackson Laboratories (stock number: 027704).

Colonies Genotyping and Management:

The *Npc1*^{nih} allele, also known as *Npc1*^{m1N} (JAX Mice 003092), was genotyped by using the following PCR primers: (F: GGTGCTGGACAGCCAAGTA and R: GATGGTCTGTTCTCCCATG). For *Npc1*^{I1061T}, we designed a real-time SNP genotyping assay (Custom Taqman Assay Design Tool; Thermo Fisher Scientific). Samples were amplified with primers and probes (Probes: FAM: TTACTGGCTGTTAGCCG-MGBNFQ, VIC: ATGTTACTGGCTATTAGCCG-MGBNFQ, F: GCTGACTATACTGATGCCATGAAGA, R: CCCTTAGAACGCATGGTTTCC) using a universal 2x Taqman master mix (Thermo Fisher Scientific) and an ABI 7500 instrument for thermocycling and detection. *Npc1*^{em1Pav} were genotyped as previously described in Chapter II. In addition to the tails, the yolk sacs were also collected for embryos and newborn pups. All colonies were maintained by following the

standard protocol of Animal Care and Use Committee, (ACUC) from the NHGRI. Heterozygotes were mated to generate homozygote mice for analysis.

Organ Weights and Dissections:

Dissections were performed under a stereomicroscope (Carl Zeiss AG Discovery V12) in order to remove organs after C-section. Briefly, a midline incision was made into the abdomen in order to expose the xiphoid process. The thoracic cavity was exposed and the thymus, heart, trachea and all lung lobes were removed *en bloc*. Each organ was immersed in 1X Phosphate-buffered saline (PBS) and dissected using forceps. All organs were weighed using a digital scale (Sartorius, CPA225D Semimicro Balance).

Embryo and Tissue Histology/Staining and Immunohistochemistry:

All embryos and tissues were harvested and fixed overnight at 4˚C in 4% paraformaldehyde (Ted Pella). Tissues were then washed twice with 1X PBS before storage in 70% ethanol at 4˚C until histology processing (Histoserv Inc, Germantown MD). Briefly, samples were dehydrated through graded alcohols, cleared in xylene, and infiltrated with paraffin. After processing, all tissues were embedded in paraffin. The paraffin blocks were cut on a microtome at 5 μm

Hematoxylin and Eosin (H&E) Staining:

The unstained slides were deparaffinized through xylene and graded alcohols to water, stained in hematoxylin, then rinsed again in water. The slides were then placed in 95% ethanol before staining with eosin and dehydrating through graded alcohols to xylene. The stained H&E slides were then mounted with permount.

Skeletal Preparations:

E18.5 embryos were collected, and an alcian blue/alizarin red staining was performed using previously published skeletal preparation protocol [141].

Cesarean Delivery and Fostering Experiments:

Timed mattings were set up by crossing heterozygote *Npc1*$^{+/em1Pav}$ females with *Npc1*$^{+/em1Pav}$ males. The identification of a vaginal plug was considered as half an embryonic day (E0.5). All females were separated and housed individually after a vaginal plug was identified. A non-recovery C-section was performed at E19.5. Briefly, embryos were carefully removed out of the uterine tube using blunt forceps. The placenta was also removed, and umbilical cords were cut. Newborn pups were placed on a warmed surface and stimulated with a clean Q-tip soaked in warmed PBS. Pups were introduced to foster FVB/NJ mothers with biological newborns between 1-2 days old. Newborn pups were monitored regularly for the first ten days after birth. Fostered pups were immediately recognizable due to the black coat color of the *Npc1*^{em1Pav} background strain (C57BL/6J) compared to albino FVB/NJ pups.

Medroxyprogesterone Injections:

Pregnant females were injected with pharmaceutical-grade medroxyprogesterone acetate (Depo-Provera), Pfizer (NY, USA) 50mg/ml subcutaneously at E16.5 and E18.5 in order to prevent parturition as previously described [142].

Dexamethasone injections:

Dexamethasone (VetOne) or saline solution was administered by intraperitoneal (IP) injections (0.4mg/kg) as previously described [142-144] at E16.5 and E.18.5.

Light Microscopy:

Embryo images were taken using a Stereo Discovery V12 microscope (Carl Zeiss AG) with a Z-stack feature. Immuno-histochemical images were collected using a Zeiss AxioScan.Z1 slide scanning microscope system (Carl Zeiss Inc., Thornwood, NY, USA) with a Plan-Apochromat 20x/0.8 objective lens. All images were acquired using a Hitachi HV-F202 SCL camera. Zeiss ZEN blue 2.3 software package was used for image processing and stitching.

Transmission Electron Microscopy:

Lung tissues (1 mm^3) were taken immediately following C-section and fixed for 48 hours at 4˚C in 0.1M cacodylate buffer (pH 7.4) containing 2% glutaraldehyde and 1% paraformaldehyde before being washed with cacodylate buffer three times. Tissues were then fixed with 1% OsO_4 for two hours, washed with 0.1M cacodylate buffer three times, washed with water and placed in 1% uranyl acetate for one hour at room temperature. Samples were subsequently serially dehydrated in ethanol and propylene oxide and embedded in EMBed 812 resin (Electron Microscopy Sciences, Hatfield, PA, USA). Thin sections, approximately 80 nm, were obtained by utilizing the Leica ultracut-UCT ultramicrotome (Leica, Deerfield, IL, USA) and placed onto 300 mesh copper grids and stained with saturated uranyl acetate in 50% methanol and then with lead citrate. The grids were viewed in the JEM-1200EXII electron microscope (JEOL Ltd, Tokyo, Japan) at 80kV and images were recorded on the XR611M, mid mounted, 10.5M pixel, CCD camera (Advanced Microscopy Techniques Corp, Danvers, MA, USA).

DNA Extraction:

DNA for genotyping was obtained from tail biopsies or from embryonic yolk sac. DNA was purified as previously described in Chapter IV.

Genotype of Samples Used for Genetic Mapping:

DNA samples were shipped to Neogen (NE, USA) for genotyping with the Giga Mouse Universal Genotyping Array (GigaMUGA) as previously discussed (Chapter IV).

Genotype Data Analysis:

Analysis was performed as previously described (Chapter IV). A total of 29,451 informative markers were obtained between the two strains (C57BL/6J and BALB/cJ).

QTL linkage Analysis:

Linkage analysis was performed as previously described (Chapter IV). In this case the phenotype used was the percentage of homozygous offspring (segregation ratios). A permutation test (10,000 permutations) was done to obtain a 5% significance threshold (LOD = 3.09).

Statistical Analysis:

Statistical analyses were done using Prism software (GraphPad). All survival analyses were done using the log-rank test (Mantel-Cox). For figure 5.4, 5.7 and 5.10, a one-way ANOVA test was completed. A Bonferroni correction for multiple comparisons was performed comparing to the control group (*Npc1*$^{+/+}$). All Chi-squared tests were performed using two degrees of freedom based on the expected number of animals per genotype. In all figures *$p<0.05$, **$p<0.001$, ***$p<0.0001$.

Results:

Reduced postnatal viability of *Npc1*$^{em1Pav/em1Pav}$ offspring.

The segregation ratios observed from mating *Npc1*^{em1Pav} heterozygous parents (Table 5.1) showed a reduction of homozygous offspring at postnatal day 10 (P10) (10.5%, N=88/841), which is significantly different than the expected ratio of 25% (n=210 /841 $p<0.0001$). This reduction of *Npc1* mutants is not specific to *Npc1*^{em1Pav}. For example, similar ratios are observed in *Npc1*^{nih}, 10.5% (n=18/163, p<0.001). The reduction seems to be less pronounced in *Npc1*^{I1061T} with 18% (n=74/410) but still significantly different than the expected ratios ($p=0.027$). Previous reports have also shown the presence of sub-mendelian ratios in *Npc1*^{em1Pav}mutants from other *Npc1* alleles [59,64]. These results indicate the presence of an uncharacterized lethal phenotype in *Npc1* homozygotes prior to P10.

Table 5.1 Reduction of *Npc1*$^{em1Pav/em1Pav}$ offspring at P10 in several *Npc1* alleles.

Allele & Strain	Age	Control (%)	Het (%)	Mutant (%)	Total	Chi Square P value[1]
Npc1^{em1Pav} C57BL/6J	P10	249 (29.6%)	504 (59.9)	88 **(10.5%)**	N=841	***p<0.0001***
Npc1^{nih} C57BL/6J	P10	53 (32.5%)	92 (56.4%)	18 **(11.1%)**	N=163	***p<0.0001***
Npc1^{I1061T} C57BL/6J	P10	117 (28.5%)	219 (53.5%)	74 (**18%**)	N=410	***p=0.027***

[1] Compared to expected ratios 1:2:1

Fetal growth restriction and low birth weight in *Npc1*$^{em1Pav/em1Pav}$:

In order to further characterize the lethality responsible for a reduction of *Npc1* mutants at P10 we performed embryonic dissections at E14.5, E16.5 and E18.5. *Npc1* ^{em1Pav} mutants showed normal organogenesis at E18.5 (Fig. 5.1), with no gross morphological defects identified in younger embryos (Fig. 5.2 & Fig. 5.3). However, starting from E16.5, *Npc1* ^{em1Pav} mutants showed reduced size and weight compared to controls (*Npc1*$^{+/+}$) and *Npc1* $^{em1Pav/+}$ littermates (Fig. 5.4). This lower weight was even more significant as embryogenesis progressed: E16.5 ($p<0.05$), E18.5 ($p<0.0001$) and also at birth (P0) ($p<0.0001$) (Fig. 5.7). The small body size is present throughout the lifespan of the few *Npc1* ^{em1Pav} mutants that survive beyond the postnatal period (Chapter IV).

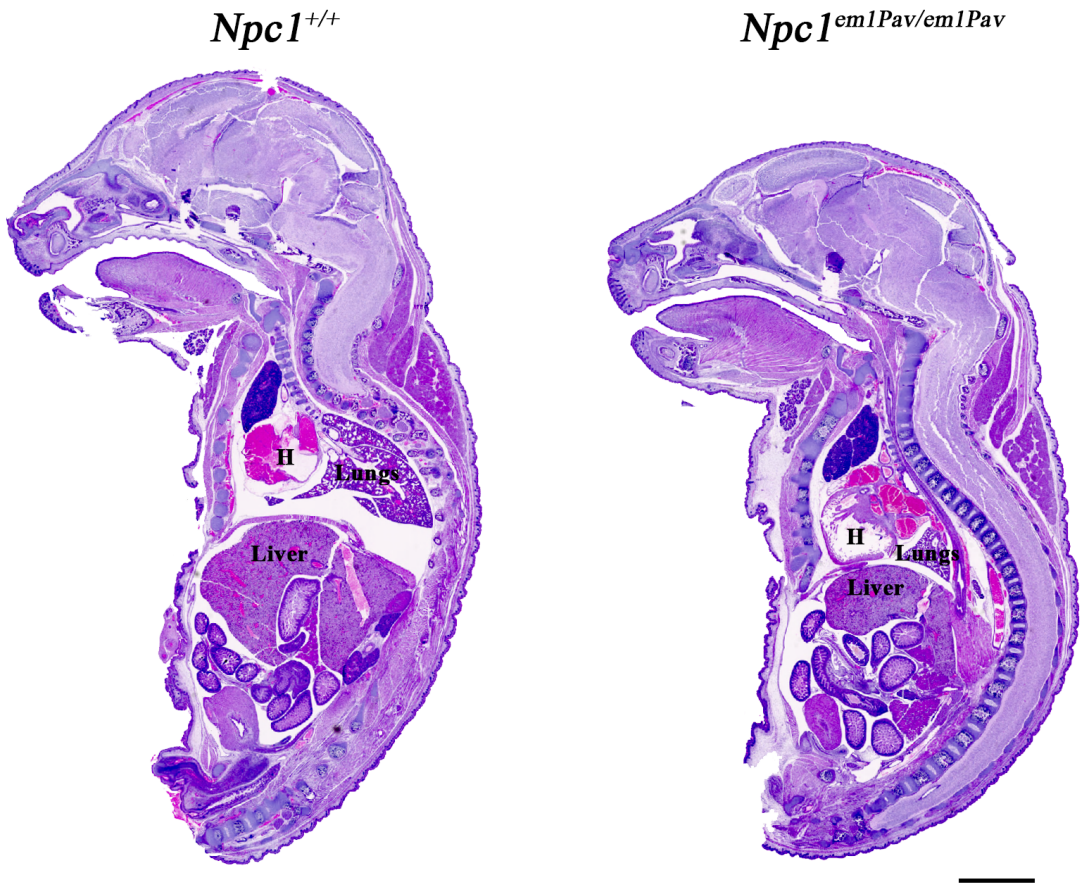


Figure 5.1 Gross anatomy of *Npc1*^{em1Pav} embryos. Sagittal section of E18.5 *Npc1*^{em1Pav} mutant (**left**) compared to control littermate (**right**). Both sections were stained with Hematoxylin and Eosin (H&E) and analyzed for gross morphological changes. *Npc1*^{em1Pav} mutants displayed normal organogenesis and cellular differentiation compared to control littermates. As previously mentioned, *Npc1*^{em1Pav} mutants are noticeably smaller than their control (*Npc1*$^{+/+}$) littermates. H= heart. Bar scale = 200μm.

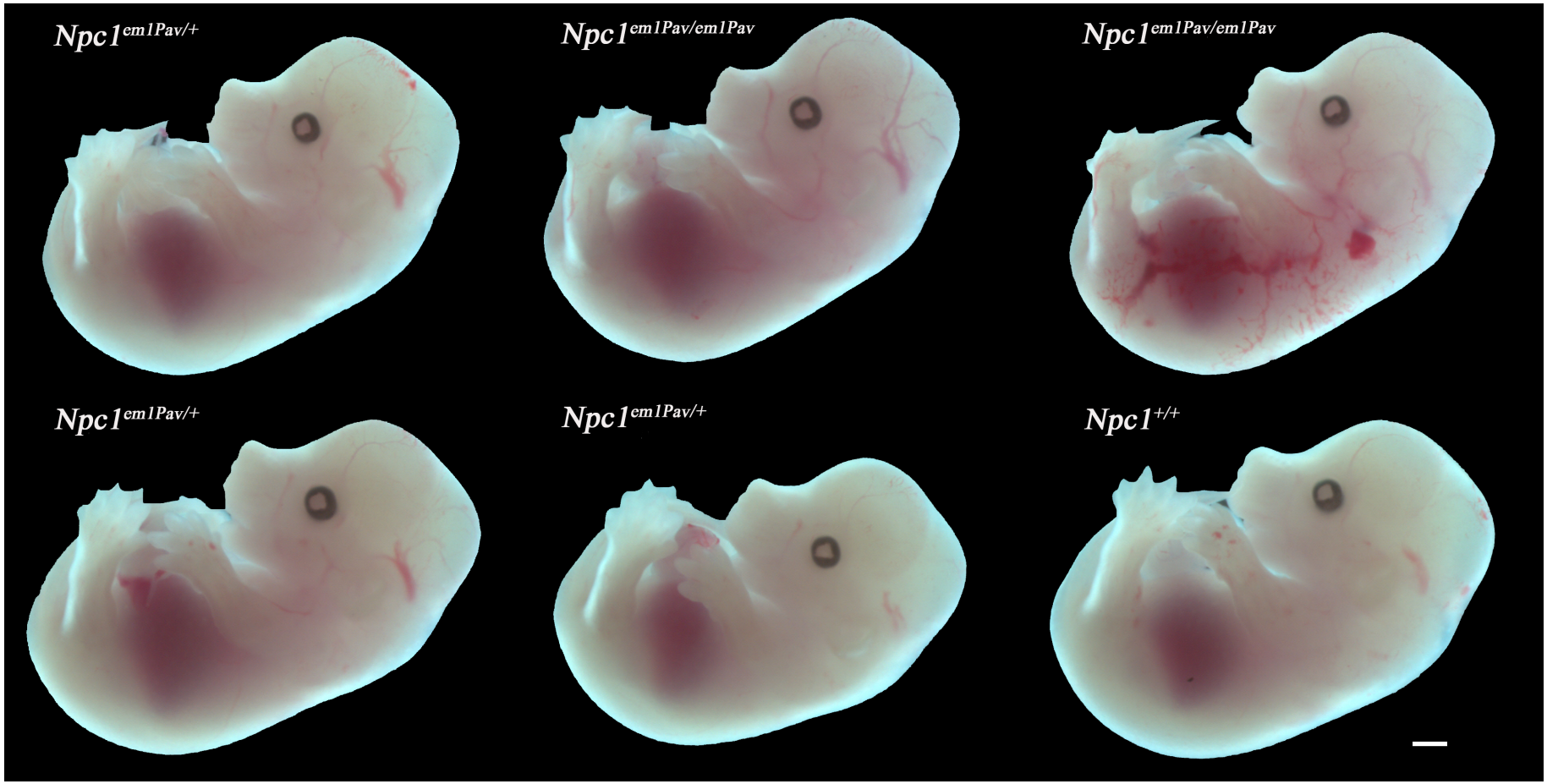


Figure 5.2 *Npc1*^{em1Pav} embryonic development (E14.5). Lateral view of littermates with their indicated individual genotype in the upper left side. No gross morphological defects were observed. *Npc1*$^{em1Pav/em1Pav}$ mutants are indistinguishable from heterozygous *Npc1*$^{em1Pav/+}$ and control (*Npc1*$^{+/+}$) littermates at this embryonic age. Scale bar =100μm

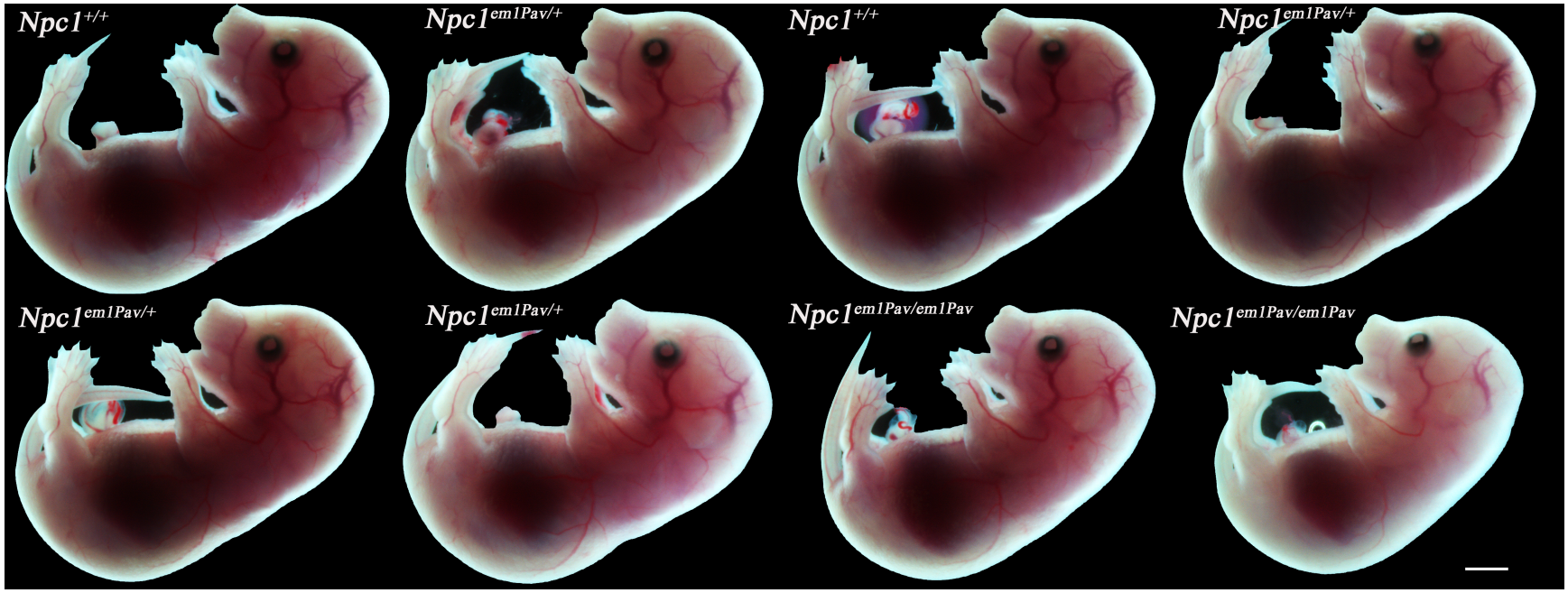


Figure 5.3 *Npc1^{em1Pav}* embryonic development (E16.5). Lateral view of littermates with their indicated individual genotype in the upper left side. Similarly, to E14.5 no specific morphological abnormalities were observed other than *Npc1^{em1Pav}* mutants were smaller in size compared to heterozygous (*Npc1$^{+/em1Pav}$*) and control (*Npc1$^{+/+}$*) littermates. Scale bar =200µm.

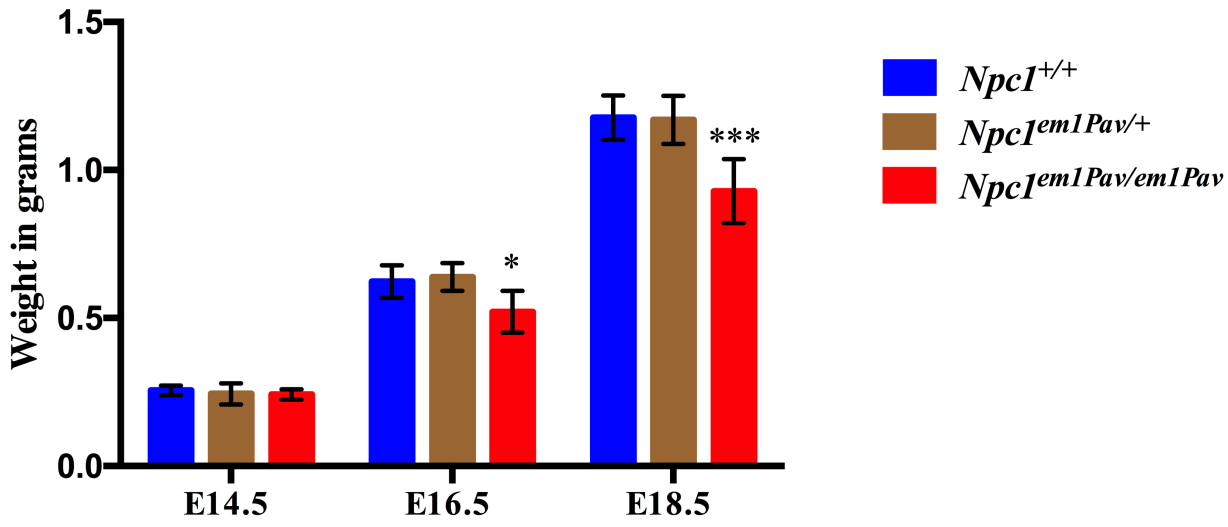


Figure 5.4 Growth restriction distribution during embryogenesis in *Npc1*^{em1Pav} mutants.

Npc1^{em1Pav} mutants have a lower weight compared to age-matched controls starting at E16.5 ($p<0.05$) and more pronounced by E18.5 ($p<0.0001$). *Npc1*$^{em1Pav/+}$ embryos are indistinguishable from controls. E14.5: *Npc1*$^{+/+}$ (n=4), *Npc1*$^{em1Pav/+}$ (n=7), *Npc1*$^{em1Pav/em1Pav}$ (n=3). E16.5: *Npc1*$^{+/+}$ (n=3), *Npc1*$^{em1Pav/+}$ (n=10), *Npc1*$^{em1Pav/em1Pav}$ (n=4). E18.5: *Npc1*$^{+/+}$ (n=6), *Npc1*$^{em1Pav/+}$ (n=20), *Npc1*$^{em1Pav/em1Pav}$ (n=6).

Npc1 mutation leads to neonatal lethality in the majority of _Npc1_$^{em1Pav/em1Pav}$:

Segregation ratios were analyzed for _Npc1_^{em1Pav} at E18.5 and E19.5 (Table 5.2). The observed number of _Npc1_^{em1Pav} homozygous mutants (26.5%, N=112/422) was not significantly different than the expected ratio (25%; p=0.341), suggesting the reduction of mutant offspring seen at P10 was due to a lethal phenotype after birth and not during embryogenesis. This also fits with our observation of the absence of gross morphological anomalies in _Npc1_^{em1Pav} mutants during embryogenesis.

In order to further characterize this lethal phenotype, we performed cesarean deliveries accompanied by maternal fostering (Fig. 5.5). Monitoring of newborn pups revealed the majority of _Npc1_^{em1Pav} mutants (55 %, n=16/29) died within the first 24 hours after birth while all of the controls and _Npc1_^{em1Pav} heterozygotes survived (Fig. 5.6A). The overall survival status post-cesarean deliveries at P10 was only 28% (n=8/29) for the _Npc1_^{em1Pav} mutants, similar to the sub-mendelian ratios observed at P10 following natural birth (Table 5.1). These results show for the first time that the majority of _Npc1_^{em1Pav} mutants die during the neonatal period, explaining the reduced homozygous ratios in this allele and potentially other _Npc1_ mouse models.

Table 5.2 Normal Mendelian ratios of *Npc1*$^{em1Pav/em1Pav}$ offspring during embryogenesis.

Allele & Strain	Age	Control (%)	Het (%)	Mutant (%)	Total	Chi Square P value[1]
Npc1^{em1Pav} C57BL/6J	P10	249 (29.6%)	504 (59.9)	88 **(10.5%)**	n=841	***p<0.0001***
	E18.5-E19.5	114 (27.0%)	196 (46.5%)	112 **(26.5%)**	n=422	p=0.341

[1] Compared to expected ratios 1:2:1

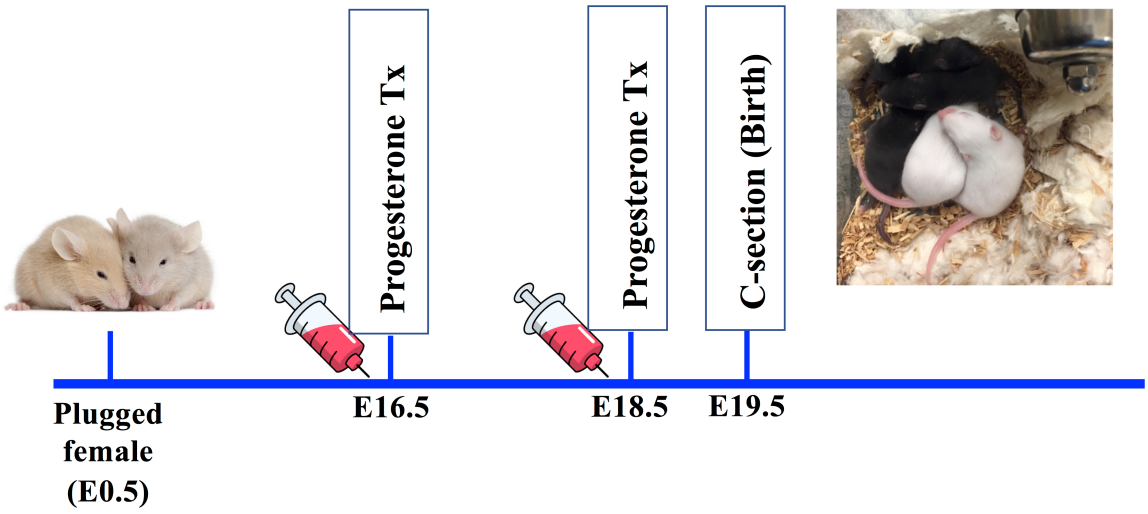


Figure 5.5. Timeline for Cesarean deliveries and maternal fostering of *Npc1*^{em1Pav}. Pregnant *Npc1*$^{em1Pav/+}$ females were identified by the presence of a vaginal plug (E0.5). In order to prevent spontaneous vaginal birth so we could time our C-sections and monitor the newborns we performed subcutaneous injections of medroxyprogesterone acetate (Depo-Provera) at two timepoints: E16.5 and E1.8.5, as previously described [142,145]. Cesarean deliveries were performed (E19.5) and newborn pups were immediately fostered with FVB/NJ mothers and monitored. Maternal fostering also served to rule out C57BL/6J maternal behavior as a possible cause of lethality following *Npc1*^{em1Pav} natural births.

Respiratory insufficiency as a potential cause of neonatal lethality in *Npc1$^{em1Pav/em1Pav}$*:

Monitoring of newborn pups shortly after birth revealed the presence of cyanosis in *Npc1^{em1Pav}* mutants (Fig. 5.6B) suggesting lack of proper oxygenation due to circulatory or respiratory dysfunction. *Npc1^{em1Pav}* mutants also showed increased respiratory effort evident from visible gasping and subcoastal retractions (video not shown). Based on these results, we analyzed the main organ systems predicted to cause neonatal lethality. For example, in order to rule out heart malformations and respiratory obstruction we analyzed the heart and the ribcage structure of *Npc1^{em1Pav}* mutants and did not find any morphological abnormalities (Fig. 5.8. & 5.9). Normalized organ weights of both lungs and heart from *Npc1^{em1Pav}* mutants were similar to control littermates (Fig. 5.10), ruling out hypoplasia of these organs at birth.

Given the well-studied role of surfactant function and neonatal mortality [146,147], we further analyzed lung tissues from *Npc1^{em1Pav}* newborn pups using electron microscopy (EM). Type II alveolar cells (T2C) from the *Npc1^{em1Pav}* newborn mutants contained abnormal accumulation of lipids droplets within their cytoplasm (Fig. 5.11). Furthermore, lamellar-like surfactant particles accumulated in the air-space (Fig. 5.12) resulting in enlarged alveolar macrophages compared to control littermates (Fig. 5.13) Additionally, we detected alveolar lipidosis prior to birth in E.165 *Npc1^{em1Pav}* mutants (Fig. 5.14) These results indicate *Npc1^{em1Pav}* newborn mutants display labored breathing at birth accompanied by abnormal lipidosis and surfactant accumulation in the lung's alveolar space, strongly suggesting the cause of *Npc1* neonatal lethality is linked to respiratory insufficiency.

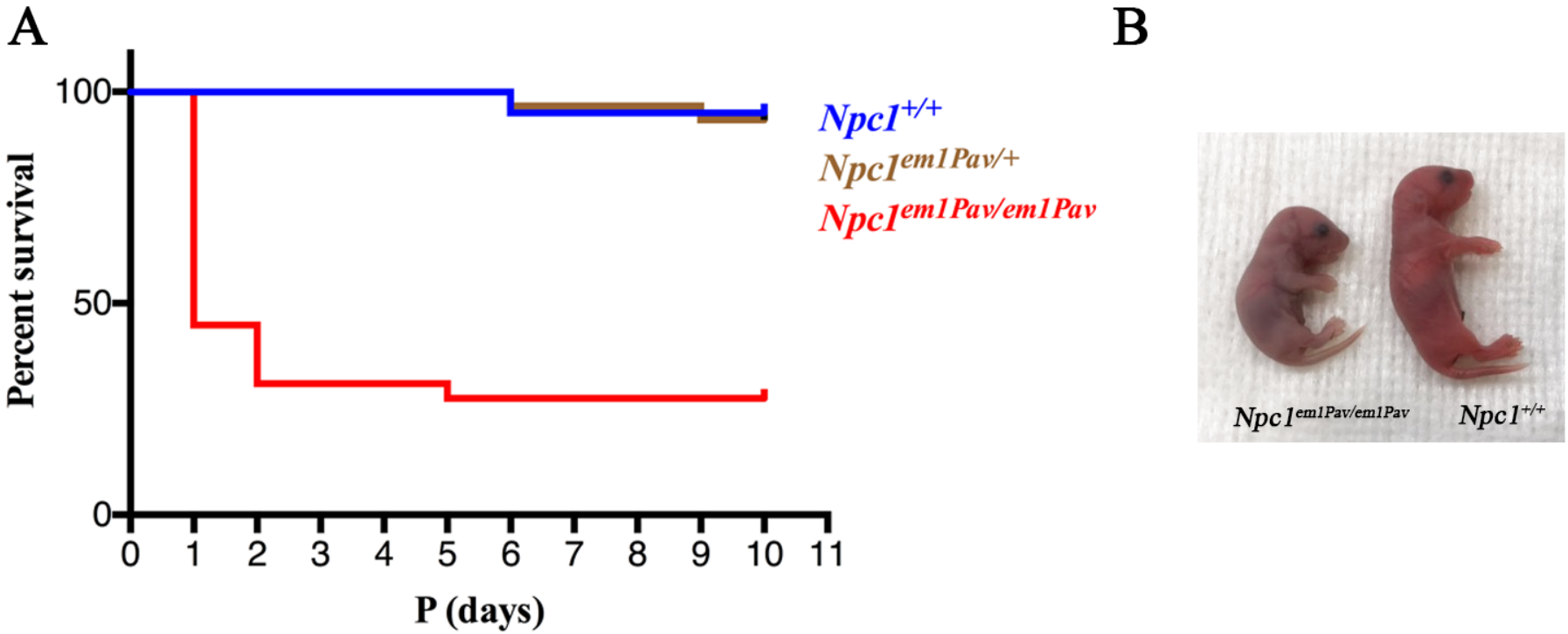


Figure 5.6. Neonatal lethality in *Npc1*$^{em1Pav/em1Pav}$. A) Survival of *Npc1*^{em1Pav} after cesarean delivery. During the first 24 hours after birth, the majority of *Npc1*^{em1Pav} mutants died (n=16) while all the heterozygous and control littermates survived ($p<0.0001$). Overall survival at P10 was 95% for controls, 93% for *Npc1*^{em1Pav} heterozygous and 28% for *Npc1*^{em1Pav} mutants ($p<0.0001$). Control (blue, n=20), heterozygous (brown, n=30), mutants (red, n=29). **B)** Representative picture of cyanosis in *Npc1*^{em1Pav} mutant (**left**) compared to control littermate (**right**) immediately after birth.

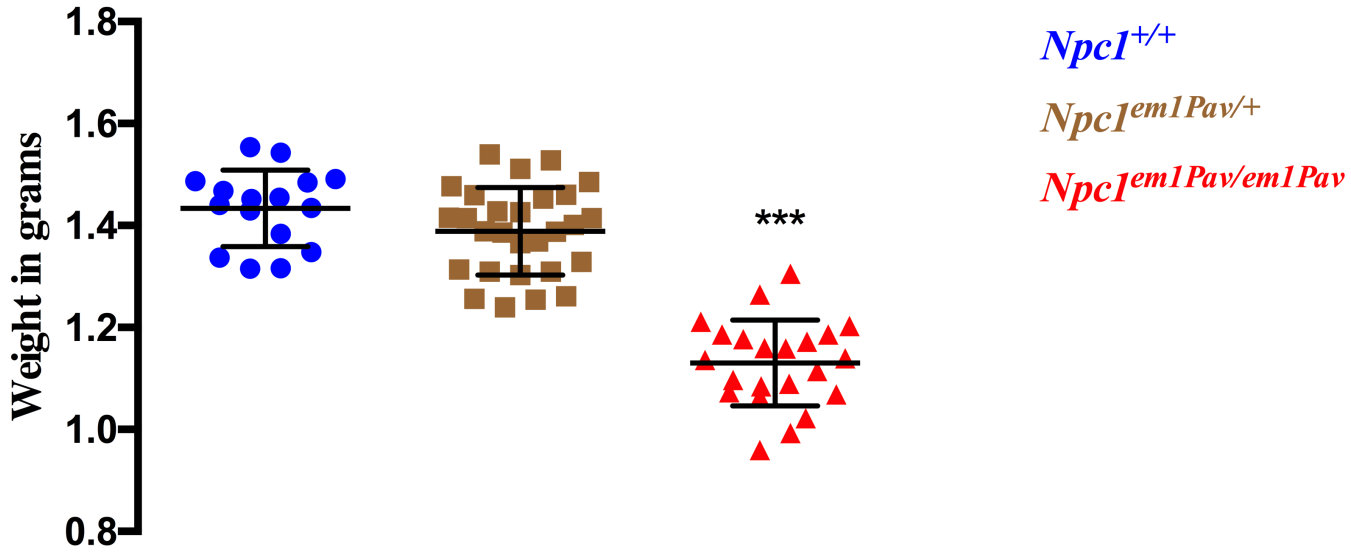


Figure 5.7 Low birth weight in *Npc1*^{em1Pav} mutants. Weights were recorded immediately after cesarean delivery. As previously observed during the last period of embryogenesis, *Npc1*^{em1Pav} mutants had a lower birth weight (red triangles, n=22) compared to controls (blue dots, n=16) and *Npc1*^{em1Pav} heterozygous (brown squares n=28) $p<0.0001$. Each dot represents an individual newborn.

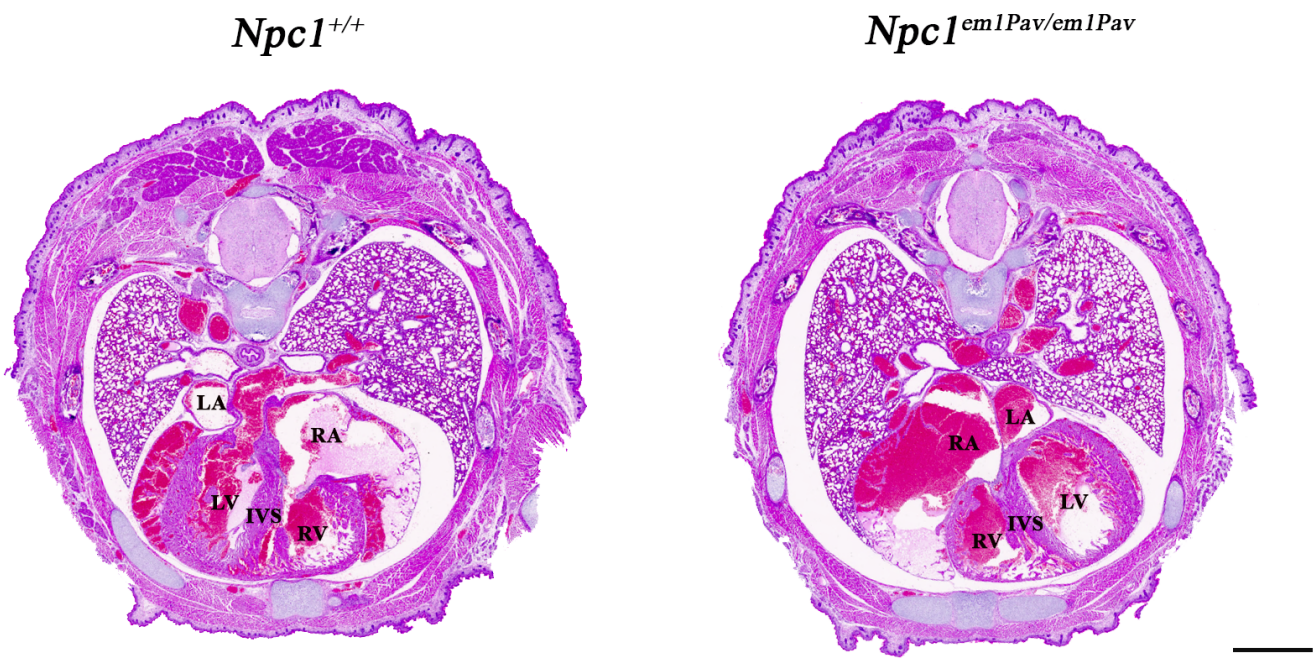


Figure 5.8 Crossed-sectional examination of thoracic cavity from *Npc1*^{em1Pav}. H&E staining at the cardiopulmonary level of control (left) and *Npc1*^{em1Pav} mutant (right) at P0, shows normal heart morphology as well as no structural defects in the intercostal muscles. Gross lung morphology also appears normal. RA= right atrium, RV= right ventricle, IVS= interventricular septum, LA= left atrium, LA= left atrium. Scale bar = 1mm.

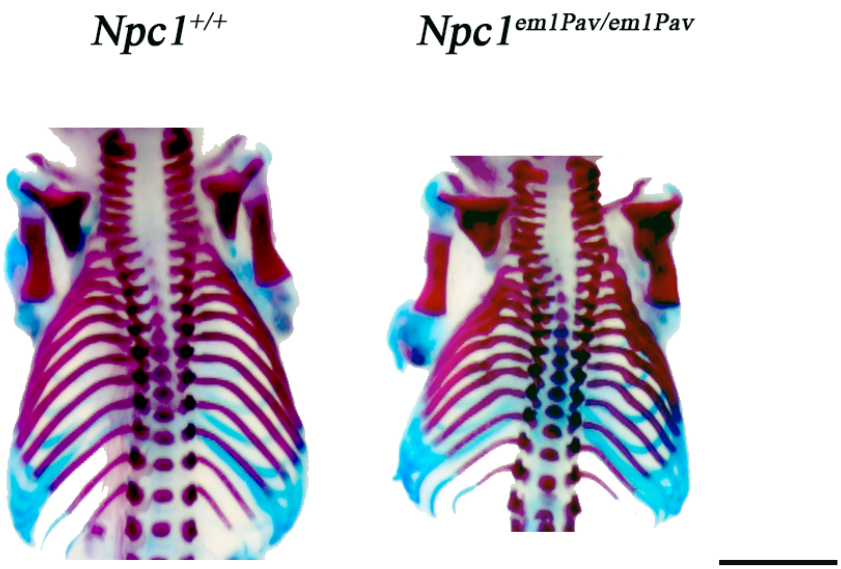


Figure 5.9 Skeletal preparation of *Npc1*^{em1Pav} mutants at birth. Dorsal view of ribcage and thoracic spine with alizarin red (bone) and alcian blue (cartilage). *Npc1*^{em1Pav} mutant (**right**) showed normal number of ribs (12) and thoracic vertebrae (13) without any abnormal restrictive structures that could interfere with normal respiration. Although occasional differences in the rib arch angle were observed between individual newborns, these differences did not segregate with genotype and were likely due to variation in the dissection and staining protocol. Control littermate (**left**) is shown for comparison. Scale bar = 500um.

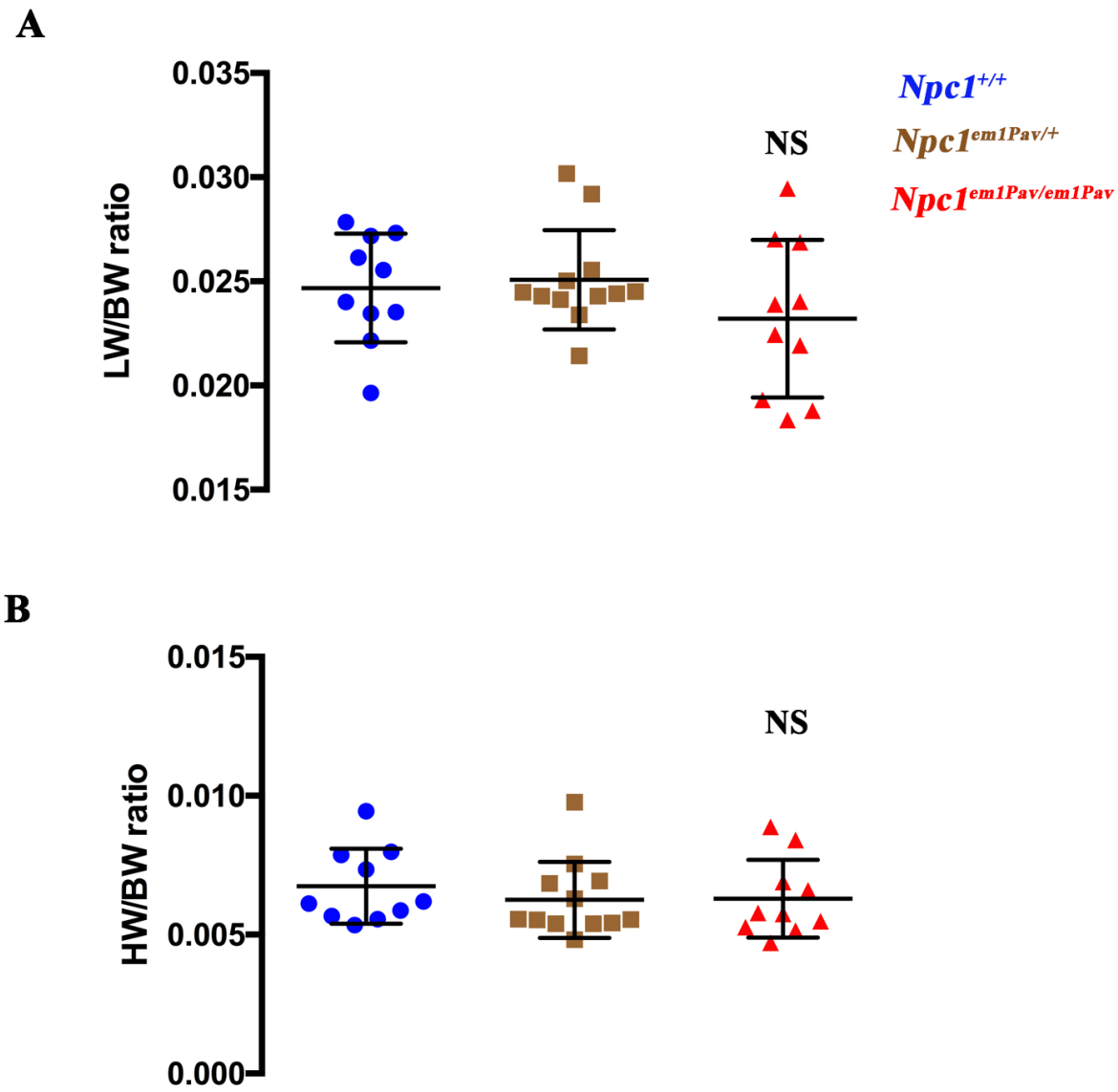


Figure 5.10 Normalized weight of lung and heart in *Npc1*^{em1Pav} mutants. Wet-weights of both lungs and heart were analyzed at birth. Weights of the lung **(A)** and heart **(B)** were normalized to body weight. There were no significant differences between the three genotypes for either lung or heart (p>0.05). LW=absolute lung weight, HW= absolute heart weigh, BW= body weight. All weights were measured in milligrams. Each dot represents an individual newborn.

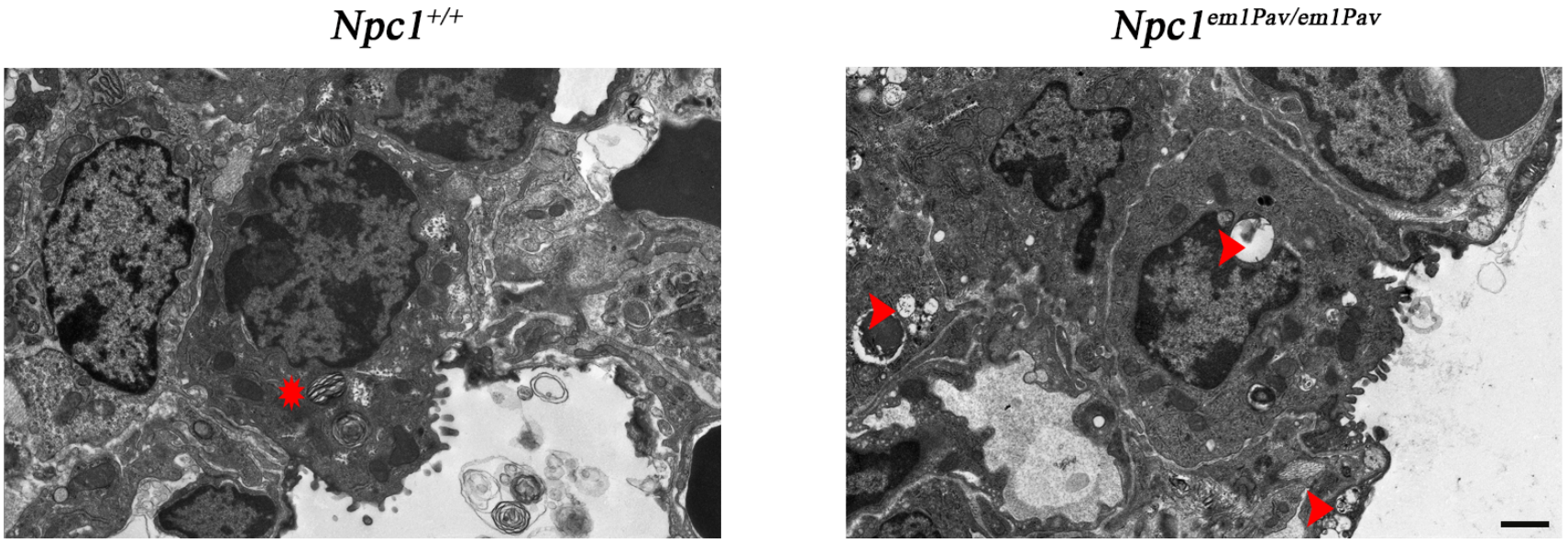


Figure 5.11. Alveolar lipidosis in *Npc1*^{em1Pav} newborn mutants. Control (**left**) lung section with representative normal AT2 cells. Notice the microvilli extrusions into the alveolar space. Lamellar body (LB) is indicated (red star). *Npc1*^{em1Pav} mutant (**right**) with general lipidosis present in the lung tissue including AT2 cells (red arrowheads). Scale bar = 1μm.

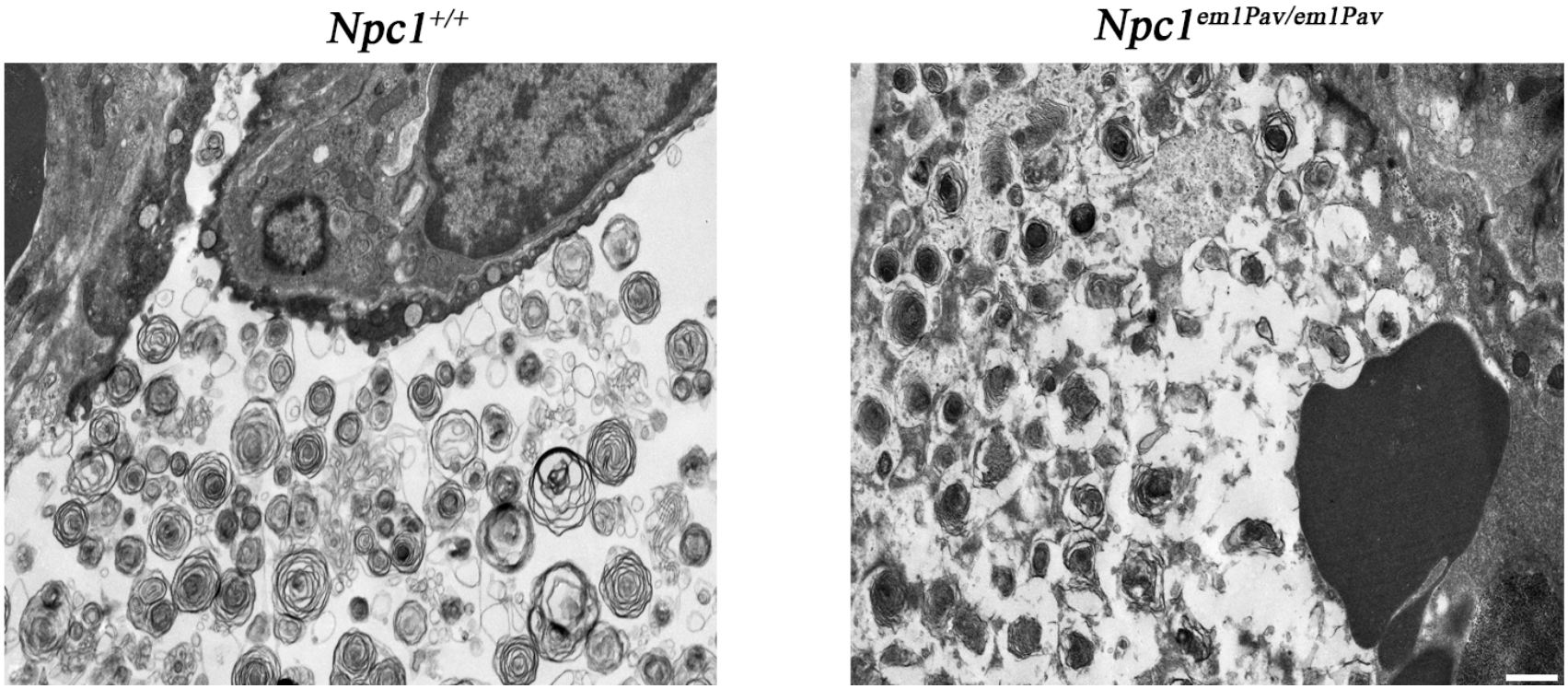


Figure 5.12 Abnormal intra-alveolar surfactant accumulation in *Npc1*^{em1Pav} newborn mutants. Control (**left**) shows lamellar-body like surfactant particles being secreted from AT2 cells into the air space with their classical "onion ring" structure. *Npc1*^{em1Pav} mutants (**right**) show and accumulation of abnormal lamellar-body like surfactant with an amorphous extracellular material occupying the air space. Scale bar =1μm.

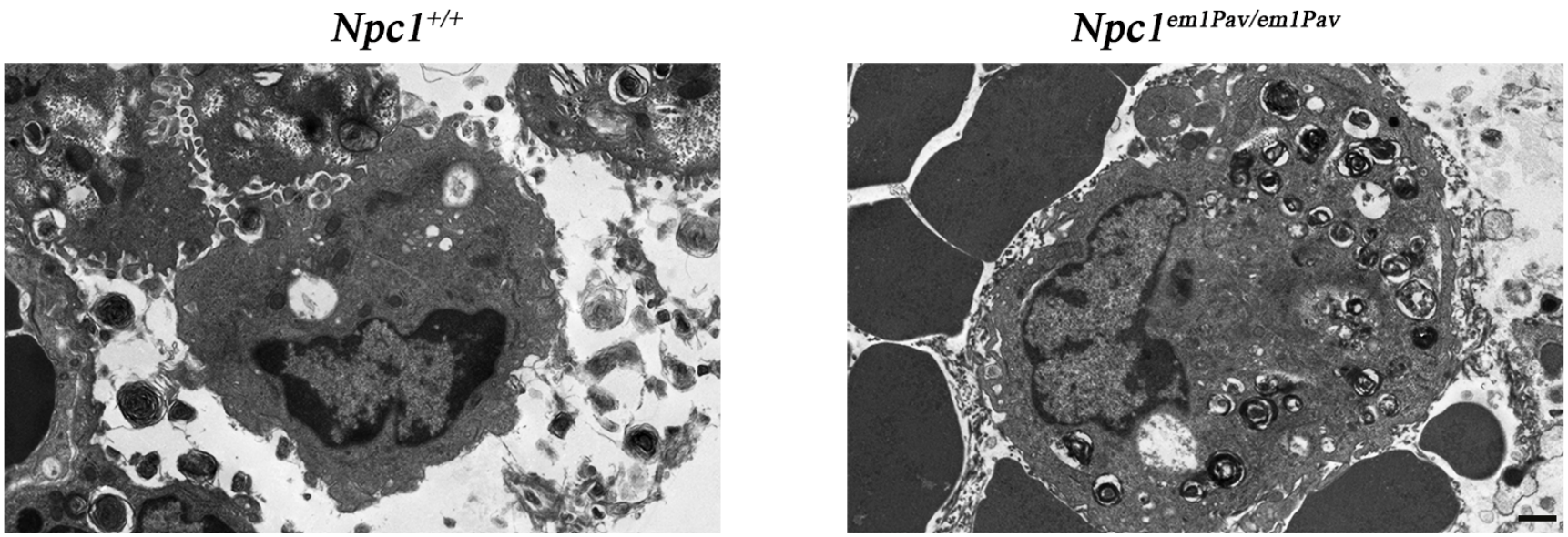


Figure 5.13 Enlarged alveolar macrophages are present in in *Npc1*^{em1Pav} newborn mutants. Foamy enlarged macrophages filled with vacuole-like particles are present in *Npc1*^{em1Pav} newborn mutants (**right**) compared to control littermates (**left**). Macrophages were identified by their lack of microvilli and their non-polymorphic oblong shaped nucleus. Scale bar =1μm.

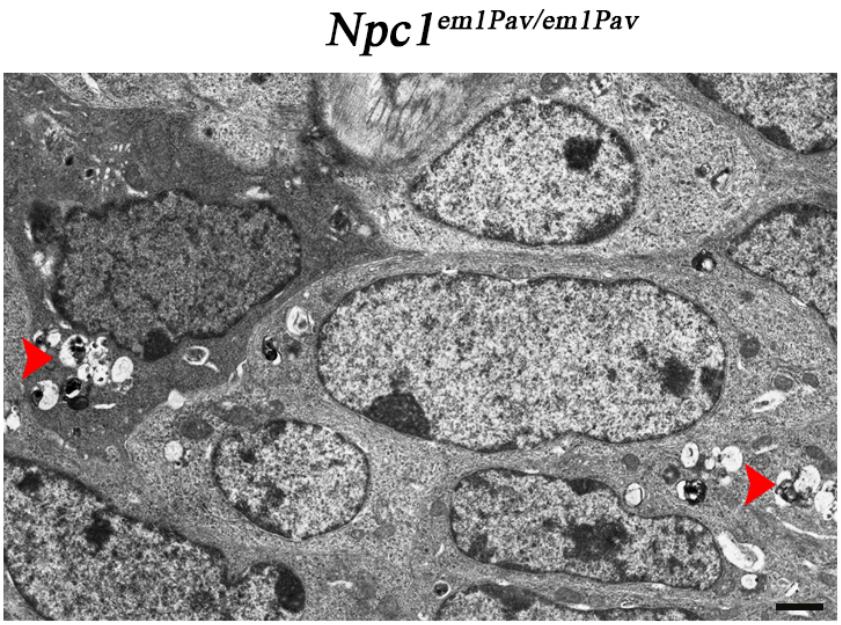


Figure 5.14 Alveolar lipidosis in *Npc1*^{em1Pav} during embryogenesis. General lipidosis (red arrowhead) within the lung tissue is seen in *Npc1*^{em1Pav} mutant embryos at E16.5. Scale bar =1μm.

Antenatal corticosteroid therapy does not increase neonatal survival in *Npc1*$^{em1Pav/em1Pav}$:

Corticosteroid administration has been shown to accelerate fetal lung maturation and decrease atelectasis at birth due to reduced pulmonary surfactant [145,148,149]. In order to test if the neonatal lethality observed in *Npc1*^{em1Pav} mutants was linked to lung immaturity affecting surfactant function, we treated pregnant *Npc1*$^{em1Pav/+}$ with dexamethasone (corticosteroid) as previously described [144]. There was no significant increase in the overall survival at birth when comparing the treated group to the untreated group (p=0.6895) (Figure 5.15). These results suggest that the neonatal respiratory dysfunction seen in *Npc1*^{em1Pav} mutants is not due to immaturity of the respiratory system and antenatal corticosteroid therapy may not be a valid approach to increase their survival.

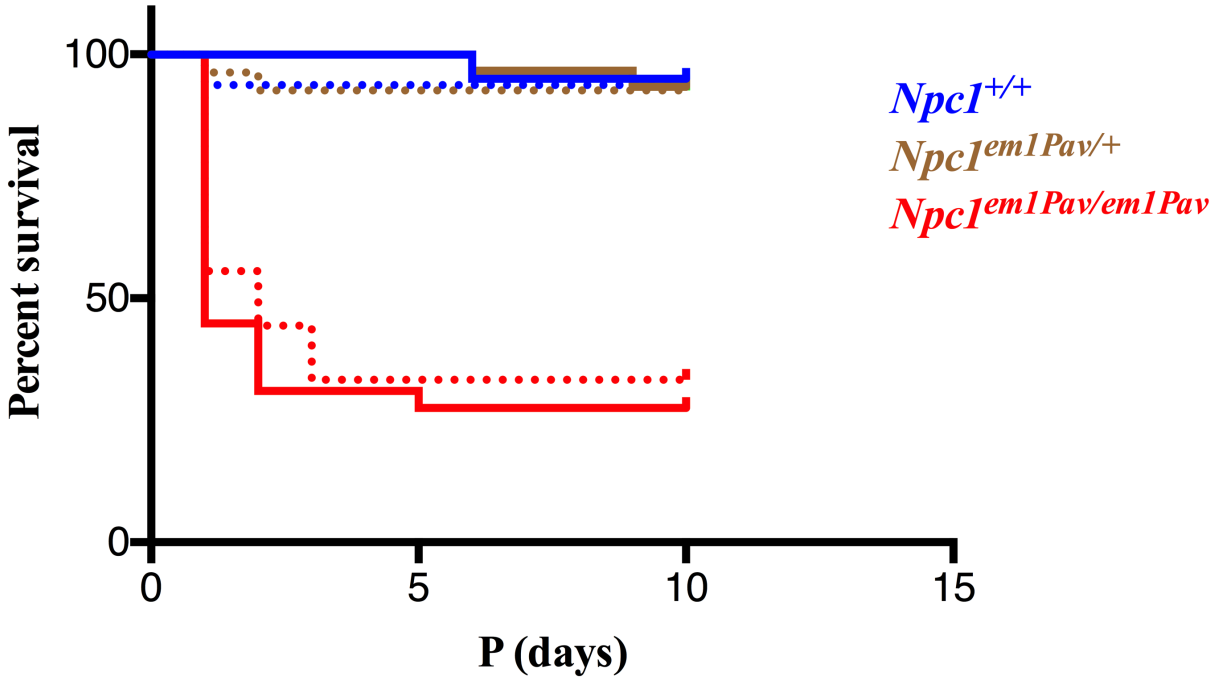


Figure 5.15 Overall survival of *Npc1*^{em1Pav} after Dexamethasone treatment *in-utero*. Survival was measured in *Npc1*^{em1Pav} newborns after administration of dexamethasone *in-utero* (dashed lines) control (n=16), *Npc1*$^{em1Pav/+}$ (n=27), *Npc1*$^{em1Pav/em1Pav}$ (n=9). There was not a significant improvement in survival of *Npc1*^{em1Pav} mutants compared to the untreated group (solid lines) control (n =20), *Npc1*$^{em1Pav/+}$ (n =30), *Npc1*$^{em1Pav/em1Pav}$ (n =29) p=0.6895.

Severity of neonatal lethality in *Npc1*^{em1Pav} mutants depends on genetic background.

As previously discussed in Chapter IV, we showed strain-specific differences in the overall survival of *Npc1*^{em1Pav} mutants and identified two QTLs with significant linkage to lifespan as a phenotype. When analyzing the percentage of *Npc1*^{em1Pav} mutants being born from our genetically mixed N2 generation (B6J(B6JCF1), we noticed a significant increase of homozygous offspring (21.2%, n=220) compared to the number observed in the C57BL/6J colony (10.5%, n=88) $p<0.0001$ (Table 5.3). This increase in neonatal survival was also observed when comparing *Npc1*^{em1Pav} BALB/cJ (N6 generation) (18%, n=161) to C57BL/6J ($p=0.0072$). This phenomenon is not unique to our newly generated allele (*Npc1*^{em1Pav}) as the null allele: *Npc1*^{nih}, also showed an increase in neonatal survival of homozygous offspring on a BALB/cJ background (18.3%, n=669) compared to a C57BL/6J background (11.1%, n =163) ($p<0.0001$). However, this increase in neonatal survival is still significantly lower than the expected mendelian ratio of homozygotes (25%) for both *Npc1*^{em1Pav} ($p<0.072$), and *Npc1*^{nih} ($p<0.0001$) suggesting that the BALB/cJ genetic background is not sufficient to fully rescue the neonatal lethality observed in *Npc1*. Taken all together, these results suggest there is a genetic component modifying the severity of neonatal lethality associated with NPC in these two alleles. One potential explanation would be the presence of genetic modifiers specifically affecting survival at birth (neonatal onset) independent of the lifespan (adult phenotype) QTLs described in Chapter IV.

Table 5.3 Strain-specific differences in neonatal lethality from *Npc1* mouse models.

Allele & Strain	Age	Control (%)	Het (%)	Mutant (%)	Total	Chi Square P value[1]	Chi Square P value[2]
Npc1^{em1Pav} C57BL/6J	P10	249 (29.6%)	504 (59.9)	88 **(10.5)**	n=841	***p<0.0001***	
Npc1^{em1Pav} B6J(B6JCF1)[3]	P10	288 (27.7)	529 (51.1)	220 **(21.2)**	n=1,037	***p=0.0094***	***p<0.0001***
Npc1^{em1Pav} BALB/cJ[4]	P10	41 (25.5)	91 (56.5)	29 **(18.0)**	n=161	***p=0.0016***	***p=0.0072***
Npc1^{nih} C57BL/6J	P10	53 (32.5%)	92 (56.4%)	18 **(11.1)**	n=163	***p<0.0001***	
Npc1^{nih} BALB/cJ	P10	201 (30%)	345 (51.5%)	123 **(18.3)**	n=669	***p<0.0001***	***p<0.0001***

[1] Compared to expected ratios 1:2:1, [2] Compared to expected ratios based on C57BL/6J ratios, [3] N2 generation used for mapping in chapter IV.[4] From BALB/cJ N6 generation presented in Chapter IV.

Using genetic test-crosses in order to map genetic modifiers of neonatal lethality in *Npc1^{em1Pav}*:

In order to discover genetic variants associated with strain-specific changes in the severity of neonatal lethality in NPC, we performed genetic test crosses. These crosses were set-up by using a *Npc1$^{em1Pav/+}$* male from the N2 generation (Chapter IV). As previously discussed, this genetically mixed generation showed a significant increase in homozygous offspring survival suggesting that heterozygosity for BALB/cJ was associated with increased survival at birth. We hypothesized that the proportion of homozygotes surviving the neonatal period would be determined by the genotype of individual breeders at unknown modifiers affecting neonatal lethality. Breeders that were homozygous C57BL/6J at the unknown QTLs would have a higher rate of neonatal lethality in their progeny than breeders that were heterozygous for BALB/cJ alleles at the unknown QTLs. And therefore, individual N2 male breeders could be test crossed with C57BL/6J females and the rate of neonatal lethality observed in the offspring would provide a phenotype for QTL mapping (Fig. 5.16).

Table 5.4 shows the results obtained from 13 different *Npc1$^{em1Pav/+}$* N2 males that were test crossed to determine the segregation ratios observed in their offspring at P10. The observed ratio of *Npc1^{em1Pav}* mutants surviving from each test cross male ranged from 11.5% to 22.6% overlapping with the ratios we observed from the C57BL/6J and BALB/cJ colonies. These 13 *Npc1$^{em1Pav/+}$* males were genotyped using the previously described GigaMUGA array from Neogen (Chapter IV) using the observed ratios as a quantitative phenotype to map QTLs affecting neonatal lethality. QTL analysis of only these 13 samples revealed one promising QTL located on chromosome 16 (LOD=1.60). Although this was below the statistical significance threshold, we believe by increasing the number of *Npc1$^{em1Pav/+}$* male breeders we will be able to

further define significant QTL regions. These promising results demonstrate the presence of genetic factors affecting our novel phenotype of neonatal lethality associated with NPC.

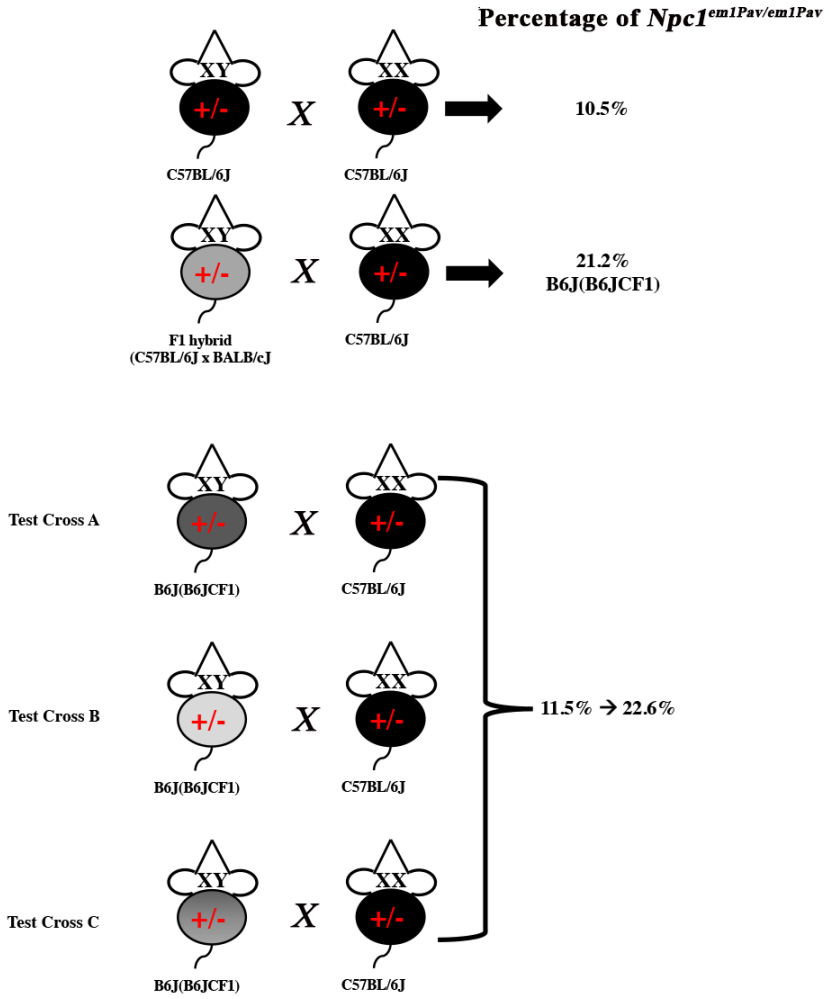


Figure 5.16 Using genetic test crosses in order to discover genetic modifiers of neonatal survival in *Npc1*^{em1Pav}. Observed percentage of *Npc1* mutants present at P10 is indicated in the right side of the figure from the expected 25% percent between heterozygous crosses. When both parents have a C57BL/6J genetic background the percentage of viable homozygous is only 10.5%. This percentage increases to 21.5% as BALB/cJ heterozygosity is introduced. By using different males from this mixed genetic background, their offspring will inherit specific genetic variants that will modify the neonatal lethality observed in their offspring as indicated by the range of percentages. +/- = *Npc1*$^{em1Pav/+}$, +/+ = control. Shading color is a representation of genetic background.

Table 5.4 Variation in *Npc1* mutant survival in progeny of individual genetic test crosses.

Male ID	Control		Heterozygous		Mutant		Total
	N	(%)	N	(%)	N	(%)	N
TC #1	67	29.9	118	52.6	39	**17.4**	224
TC #2	65	32.8	107	54.0	26	**13.1**	198
TC #3	50	25.5	117	59.6	29	**14.7**	196
TC #4	50	32.0	88	56.4	18	**11.5**	156
TC #5	52	25.3	110	53.6	43	**20.9**	205
TC #6	47	31.1	70	46.3	34	**22.5**	151
TC #7	46	25	111	60.3	27	**14.6**	184
TC #8	29	25	67	57.7	20	**17.2**	116
TC #9	43	30.4	66	46.8	32	**22.6**	141
TC #10	38	26.0	77	52.7	31	**21.2**	146
TC #11	44	28.5	79	51.2	31	**20.1**	154
TC #12	40	32.2	69	55.6	15	**12.0**	124
TC#13	45	31.0	77	53.1	23	**15.86**	102

TC= test cross.

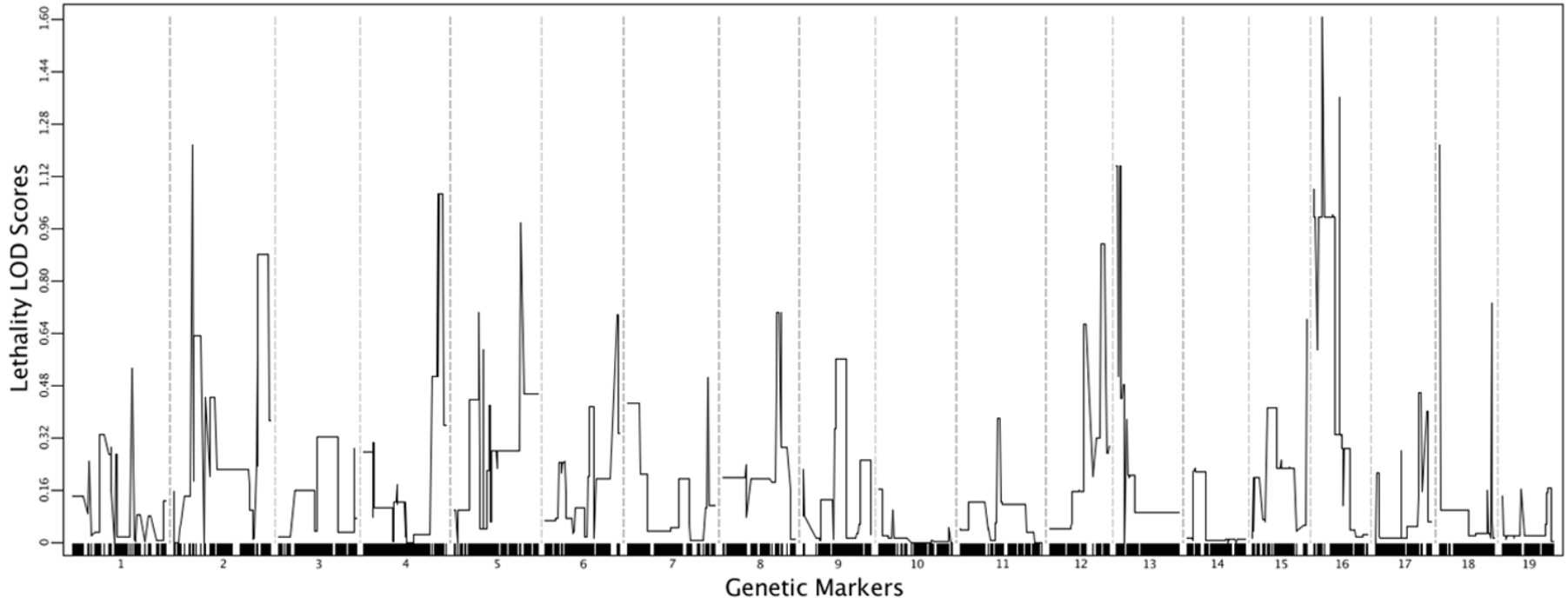


Figure. 5.17 Genetic linkage results for neonatal lethality in *Npc1^{em1Pav}* from test crosses. Genome scan results from 13 *Npc1$^{em1Pav/+}$* breeder males used for genetic test crosses. The QTL region with the highest LOD score was on Chromosome 16 (Marker ID: UNC26404275, 10.90cM, LOD=1.60).

Discussion

The earliest presentation of NPC occurs *in-utero* followed by complications during the neonatal period accompanied by a high mortality rate within the first few weeks after birth [138]. The majority of these patients develop splenomegaly and/or hepatomegaly as well as ascites detected during gestation or the neonatal period [24]. As previously outlined in Chapter I, several NPC animal models have been developed including different *Npc1* mouse alleles. While most of these have been shown to successfully exhibit features from both infantile and juvenile presentations [49], there remains a need for animal models appropriate to study the most severe presentation of the disease during the pre/perinatal period. By using our new *Npc1* mouse allele: $Npc1^{em1Pav}$, we were able to characterize for the first time a neonatal lethality phenotype in $Npc1^{em1Pav}$ mutants resulting in a reduction of viable homozygous after birth and associated with abnormal lung pathology.

The gene(s) modifying neonatal lethality observed in NPC are unknown, however can we begin to speculate on what pathways could impact the severity of this neonatal phenotype. Sequence homology between the sterol sensing domain of NPC1 and Patched1 receptor (*Ptch1*) has been identified [150]. This receptor is involved in the Sonic hedgehog (*Shh*) pathway, a well-known regulator of embryonic development [151]. Alterations based on cholesterol homeostasis have also been linked to this pathway [152]. For example in Smith-Lemli-Opitz (SLO), a disorder characterized by defects in cholesterol biosynthesis [153] patients display an array of birth defects associated with abnormal *Shh* signaling such as holoprosencephaly [154]. Additionally, the Shh-*Ptch1*-*Gli* pathway is abnormally expressed in the cerebellum of *Npc1* mutant mice at P14 as well as NPC1 patient-derived fibroblasts [155]. Interestingly, NPC patients do not display any *Shh*-associated birth defects. This also fits our results showing $Npc1^{em1Pav}$ mutants exhibited normal organogenesis. While $Npc1^{em1Pav}$ mutants showed normal gross morphology and cellular

differentiation, they presented with fetal growth restriction and lower birth weight compared to controls and *Npc1*^{em1Pav} heterozygous littermates starting at E16.5. Intrauterine growth restriction (IUGR) has also been described in NPC patients with fetal-onset [140]. One possible cause for this would be the presence of placental insufficiency [156]. Spiegel and colleagues [24], reported the presence of abnormal placental pathology including foamy cells in the villous stroma from an NPC patient with fetal-onset. Abnormal placental changes such as the presence of vacuolated cells is also highly associated with other lysosomal storage disorders [157].

NPC patients with pre/perinatal-onset develop cholestatic liver disease ultimately leading to liver failure [26, 27]. While the presence of hepatomegaly seems to be a common clinical presentation, a subgroup of patients is able to recover with only transient symptoms. These patients usually have only persistent splenomegaly until they develop NPC-related neurological symptoms later in life [26]. The reason for this difference in clinical prognosis and survival is still poorly understood. A similar phenomenon was observed in our new *Npc1* allele: *Npc1*^{em1Pav}, with decreased number of viable *Npc1*^{em1Pav} mutants (10% vs. the expected 25%) surviving up to P10. By performing C-sections and maternal fostering experiments we were able to determine more than half of the *Npc1*^{em1Pav} mutants died during the first 24 hours after birth. Those that survived, developed neurological symptoms as previously described in Chapter III. Thus, for the first time we were able to show that the reduction of *Npc1* mutants in *Npc1*^{em1Pav} and potentially other *Npc1* alleles is due to lethality specifically during the neonatal period. *Npc1*^{em1Pav} mutants were shown to be cyanotic and displayed increased respiratory effort suggesting a lack of proper oxygenation at birth. Most recently, pulmonary complications have been described as more common than previously thought in NPC patients with pre/perinatal onset. For example, Gumus

and colleagues [28] reported that pulmonary complication was considered the main cause of death for the majority of their neonatal NPC1 cohort (n =6) compared to liver failure (n =2). Another group also reported similar findings where the majority of patients (nine out of twelve) developed pulmonary manifestations [29]. When analyzing common features between these two cohorts based on clinical presentation and radiological findings, we find that NPC1 patients with pre/perinatal onset tend to develop pulmonary complications that are consistent with interstitial lung disease. This suggests the affected lung parenchyma is unable to performed adequate gas exchange leading to hypoxic features seen in neonatal NPC patients such as cyanosis, tachypnea and nail clubbing [28,29,158]. This is consistent with our observation in newborn *Npc1*^{em1Pav} mutants (Fig. 5.6B). Both reports also showed relevant lung pathology featuring the accumulation of alveolar foam macrophages as a common finding. In fact, when analyzing the lung postmortem tissues from an affected NPC1 patient by EM, the images were strikingly similar to the ones we obtained from *Npc1*^{em1Pav} mutants showing both the presence of alveolar lipidosis (Fig 5.10) as well as foam alveolar macrophages (Fig. 5.12). Collectively, these observations indicate that newborn *Npc1*^{em1Pav} mutants are able to recapitulate important pulmonary features associated with NPC patients with pre/perinatal onset and thus provide a valid model to study this phenomenon.

In order to further characterize newborn *Npc1*^{em1Pav} mutants we also performed targeted pathology work-up. For example, we were able to rule out cardiac malformations as well as some obstructive respiratory causes of death. Interestingly, we did not observe any morphological or histological abnormalities in the liver or spleen, perhaps due to interspecies differences in hepatic development between mouse and human [159,160]. We are in the process performing a more detailed work-up for these tissues that may yet reveal abnormalities in the

newborn liver or spleen.

Lung surfactant reduces the alveoli's surface tension in order to perform essential gas exchange [161]. Due to this and other properties, surfactant plays a major role in survival at birth [146]. Type II pneumocytes or Type II cells (T2C) are responsible for the synthesis, assembly and exocytosis of surfactant into the alveolar air space [162]. Surfactant is also stored in cytoplasmic lysosome-like organelles called lamellar bodies in T2C [163]. The molecular composition of surfactant is complex, as it is mainly comprised of proteins and lipids [164]. As a main component, cholesterol is the most abundant neutral lipid [165]. The amount of cholesterol present in surfactant been shown to play a role in its stability and proper function [166]. In fact, increased amounts of cholesterol have been linked to pulmonary dysfunction [167]. NPC1 function has been associated with accumulation of cholesterol within the lamellar body where it is also expressed [168]. Furthermore, abnormal surfactant composition has been reported in both *Npc1* adult mice at end-stage [169]. Similarly, our newborn $Npc1^{em1Pav}$ mutants displayed abnormal surfactant accumulation in the alveolar air space. Although this is a different phenotype than the one described in adult *Npc1* mice, we hypothesize that NPC1 dysfunction could potentially result in altering the composition of pulmonary surfactant such as increased cholesterol thus interfering with proper alveolar gas exchange at birth. We also showed antenatal treatment with corticosteroids does not improve survival at birth suggesting the pulmonary phenotype is not due to immaturity of the respiratory system.

Alveolar macrophages play an essential role in immune-response as well as processing and recycling surfactant components [164,172]. Foam alveolar macrophages are present in our $Npc1^{em1Pav}$ mutants, at birth (Fig. 5.12) this is also the case for adult $Npc1^{-/-}$ mice [169].

Additionally, more recent studies have shown the role of surfactant as in innate immunity as an anti-microbial agent [173,174].

Recurrent pneumonia is a common presentation in NPC patients suffering from neurological symptoms and has been reported as the main cause of mortality in different patient cohorts [26,170]. Dysphagia is also a common presentation seen in NPC patients and it is considered a major risk factor for aspiration-induced pneumonia [171]. Patients with an earlier non-neurological presentation of NPC also develop pneumonia [26]. In this case, risks factors seem less apparent. Based on these results we can argue that the presence of foam alveolar macrophages as well as abnormal surfactant composition are potentially risk factors for the development of pneumonia in NPC patients.

Lastly, we also showed strain-specific differences in the severity of our newly characterized neonatal lethality phenotype in *Npc1*^{em1Pav} mutants. When analyzing the percentage difference of *Npc1*^{em1Pav} mutants surviving the neonatal period between two genetic strains: C57BL/6J and BALB/cJ we showed that heterozygosity for BALB/cJ increases survival at birth. This is also present in the null allele: *Npc1*^{nih}, with an increase of more than half of the mutants surviving birth with a BALB/cJ genetic background. These results also indicated the presence of a genetic component such as genetic modifiers for this phenotype. Furthermore, our QTL analysis also showed promising linkage results to chromosome a region located in chromosome 16.

Strength and limitations:

Our results showed for the first time, the presence of a neonatal lethality phenotype associated with NPC. With C-section and maternal fostering experiments, we demonstrated the presence of

respiratory dysfunction in *Npc1*^{em1Pav} mutants validated by abnormal surfactant and foam macrophages accumulation into the air space. While these results support pulmonary abnormalities as the cause of this early lethality, further characterization is needed for confirmation. For example, we are currently analyzing the liver and spleen of *Npc1*^{em1Pav} in order to determine if splenomegaly and/or hepatomegaly results in cholestatic disease as seen in NPC patients. Additionally, neuromuscular or CNS-driven abnormalities can contribute to abnormal respiratory function. Regarding our QTL analysis, a larger sample size is needed in order to validate the QTL region in chromosome 16.

Future work:

In order to further characterize the role T2Cs such as surfactant stability and function in the setting of NPC1 we are crossing a T2C-cre mouse model (B6.129S-*Sftpc*$^{tm1(cre/ERT2)Blh}$/J) and a conditional floxed NPC1 allele *Npc1*$^{tm1.1Apl}$. This will allow us to determine if the neonatal lethality still present only when T2C are affected with NPC. Additionally, we will perform a more detail analysis of surfactant components.

Chapter VI: Conclusion

Niemann-Pick Disease Type C (NPC) is a rare and fatal neurodegenerative disorder [14]. Most of the identified mutations occur in the *NPC1* gene (95%) while the remainder occur in *NPC2* (5%) (Fig. 1.2). These two genes encode for lysosomal proteins responsible for the transport and export of cholesterol and other lipids out the lysosome (Fig. 1.4). Loss of function for either protein results in abnormal accumulation of these metabolites leading to a complex clinical picture affecting multiple organ systems [21]. The clinical presentation of NPC patients is highly heterogenous in both symptoms and age of onset [11,27]. For example, patients with pre/perinatal onset develop more visceral symptoms including hepatomegaly and/or splenomegaly sometimes resulting in fatal cholestatic disease [24]. Later onset patients tend to present with neurological symptoms such as cerebellar ataxia, dystonia and dysphagia [21]. And the least severely affected adult patients are most likely to suffer from schizophrenia-like symptoms and depressive mood disorder [31]. Miglustat (Zavesca), a glucosylceramide synthase inhibitor, is the only drug approved for the treatment of NPC in Europe [35,38] though it has not yet been FDA-approved in the United States. While miglustat and other experimental therapies have shown promising results reducing symptoms in clinical trials, they do not stop the progression of the disease resulting in early mortality [175]

Animal models have been essential in evaluating rare disorders such as NPC because the size of the patient populations are often not sufficient to power conventional clinical trials [49]. In the case of NPC, several mouse models have been generated that begin to replicate the heterogeneity seen in this patient population (Table 1.1) While these models are able to recapitulate some aspects of the disease, other NPC-associated phenotypes such as pre/perinatal onset have not been described (Chapter I). Furthermore, additional animal models are needed that harbor specific types of mutations that are common in patients in order to fully test current experimental

treatments [43,50,90]. In order to address this need, we described the generation of a new mouse model (*Npc1*^{em1Pav}), carrying a novel *Npc1* allele (Fig 2.6). This mutation causes a reduction of NPC1 protein compared to controls (Fig. 3.1). In order to validate this new *Npc1* allele, we performed histological analysis to confirm the presence of known pathological features associated with NPC. For example, we showed *Npc1*^{em1Pav} mutants developed foam cells in both the liver (Fig. 3.4) and the spleen (Fig. 3.5) as well as Purkinje cell loss (Fig 3.6). In addition, *Npc1*^{em1Pav} mutants showed progressive weight loss and motor impairment consistent with neurodegeneration (Fig. 3.9).

Identifying Genetic Modifiers in NPC Affecting Lifespan

Several animal studies have shown that changes in genetic background can modify NPC onset [79], severity [62,80] and treatment response [81]. This phenotypic variation is also observed in patients with similar *NPC1* genotypes, such as siblings, or patients with the same biochemical phenotype that can present with noticeably different clinical manifestations and disease progression [75-77]. These results strongly suggest the presence of unidentified genetic modifiers in NPC. Thus, we hypothesize that by using our new *Npc1*^{em1Pav} mouse model in combination with newly developed genomic tools we could potentially identify these modifying variants.

In Chapter IV we showed how different genetic backgrounds resulted in changes in lifespan measured in *Npc1*^{em1Pav} mutants (Fig. 4.5). QTL analysis of over 200 *Npc1*^{em1Pav} mutants with a mixed genetic background: B6J(B6JCF1) detected significant linkage to markers on chromosome 1 and chromosome 7 (Fig. 4.10). Further analysis of these two QTLs showed they contribute to lifespan changes in an additive manner (Fig. 4.11). With the help of publicly available genomic databases, such as the Mouse Genomes Project (Wellcome Sanger Institute,

UK), we were able to identify strain-specific sequence variants and rank them by their predicted deleterious effects (SIFT, PROVEAN) to generate a short list of candidate genes for both chromosomes (Fig. 4.13, 4.14 & 4.15). In order to further prioritize these candidate genes, we will combine this information with datasets from a number of different genomic platforms (Fig. 6.1). For example, we have completed an extensive transcriptomic analysis of more than 40 NPC1 patient-derived fibroblast cell lines. Additionally, Whole Exome Sequencing (WES) data has been obtained from the same patient group. As part of a collaborative effort we are also developing a CRISPR/Cas9 based genome-wide screen in order to identify genetic modifiers *in-vitro*. We hypothesize that by combining all these datasets from patient populations and humanized models will be able to prioritize candidate genes that are relevant in NPC patients and thus, have the potential to modulate the disease. As many of these pathogenic pathways are common to other LSDs [1], the identification of these genetic modifiers can also be applicable to other rare disorders.

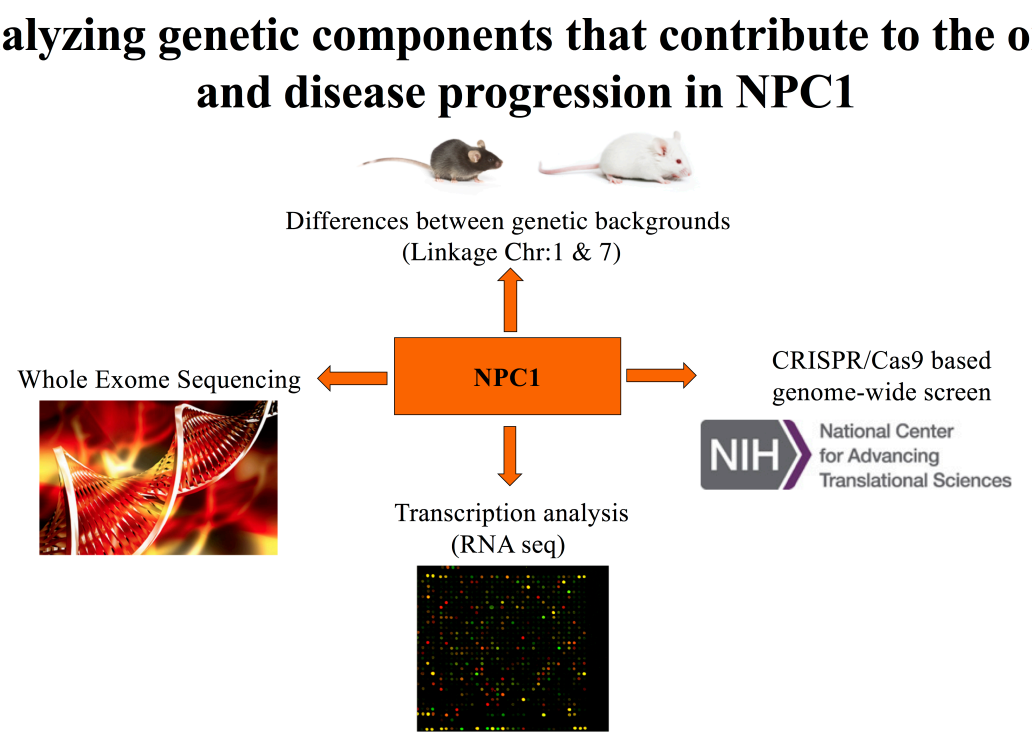


Figure 6.1 Dissecting the Genetic Architecture of NPC. In order discover and validate new genes and pathways associated with phenotypic variation in NPC we will integrate the candidate genes identified using mouse models (Chapter IV) with exome sequencing data from patients, transcript expression (RNA seq) data from patient fibroblasts and also with results from an *in-vitro* CRISPR/Cas9 screen for genes that can alter the severity of a cellular phenotype in the context of NPC.

Neonatal Lethality in *Npc1*^{em1Pav}: a new NPC mouse model of pre/perinatal onset

As mentioned in Chapter I and V, the earliest and most severe manifestation of NPC affects patients *in-utero* or shortly after birth. The most common cause of death at this age is liver failure, though recent reports seem to contradict this idea with the evidence that with most patients die from pulmonary complications instead [28,29]. After realizing a significant number of *Npc1*^{em1Pav} mutants were absent after birth (Table 5.1), we decided to further characterize this lethal phenotype as there are no current animal models available for the study of NPC with pre/perinatal onset. Embryonic dissections revealed grossly normal morphogenesis in *Npc1*^{em1Pav} mutants though they were smaller (IUGR) than their control littermates beginning at age E16.5 (Fig. 5.4). This is similar to reports indicating NPC patients are affected by IUGR. This embryonic phenotype was not enough to cause lethality during development as a normal ratio of *Npc1*^{em1Pav} mutants (26.5% vs. 25%) was observed right before birth (Table 5.2). These results suggested *Npc1*^{em1Pav} mutant were dying postnatally. C-section accompanied by maternal fostering (Fig. 5.5) confirmed that the majority of *Npc1*^{em1Pav} mutants died shortly after birth (Fig. 5.6) showing signs of respiratory insufficiency such as labored breathing and cyanosis. Subsequent electron microscopy analysis of lung tissues indicated abnormal alveolar pathology, including lipidosis of Type II pneumocytes resulting in atypical surfactant morphology. A similar phenomenon has been described in NPC patients with pre/perinatal onset [28,29] indicating *Npc1*^{em1Pav} may be a valid model of this severely affected group.

Relevance:

Identification of genetic modifiers is necessary to improve our understanding of the highly variable phenotype observed in NPC patients and to advance options for patient diagnosis and

therapy. Furthermore, use of this unique NPC mouse model to further study the role of lung pathology in pre/perinatal onset will enable us to assess new interventions desperately needed for this fatal disease.

References:

1. Platt FM, d'Azzo A, Davidson BL, Neufeld EF, Tifft CJ. Lysosomal storage diseases. Nat Rev Dis Primers 2018;4:27.

2. Schultz ML, Tecedor L, Chang M, Davidson BL. Clarifying lysosomal storage diseases. Trends Neurosci 2011;34:401–410.

3. Ferreira CR, Gahl WA. Lysosomal storage diseases. Transl Sci Rare Dis 2017;2:1–71.

4. Meikle PJ, Hopwood JJ, Clague AE, Carey WF. Prevalence of lysosomal storage disorders. JAMA 1999;281:249–254.

5. Biffi A. Gene therapy for lysosomal storage disorders: a good start. Human Molecular Genetics 2016;25:R65–75.

6. Christensen CL, Choy FYM. A Prospective Treatment Option for Lysosomal Storage Diseases: CRISPR/Cas9 Gene Editing Technology for Mutation Correction in Induced Pluripotent Stem Cells. Diseases 2017;5:6.

7. Platt FM. Emptying the stores: lysosomal diseases and therapeutic strategies. Nat Rev Drug Discov 2018;17:133–150.

8. A. Niemann:Ein unbekanntes Krankheitsbild. Jahrbuch für Kinderheilkunde, Berlin, N F, 1914. Volume 79: 1-109.

9. L. Pick: Der Morbus Gaucher und die ihm ähnlichen Krankheiten (die lipoidzellige Splenohepatomegalie Typus Niemann und die diabetische Lipoidzellenhypoplasie der Milz). Ergebnisse der Inneren Medizin und Kinderheilkunde, Berlin, 1926, 29: 519-627).

10. Schuchman EH, Desnick RJ. Types A and B Niemann-Pick disease. 2017.

11. Vanier MT, Millat G. Niemann-Pick disease type C. Clinical Genetics 2003;64:269–281.

12. Loftus SK, Morris JA, Carstea ED, Gu JZ, Cummings C, Brown A, Ellison J, Ohno K, Rosenfeld MA, Tagle DA, Pentchev PG, Pavan WJ. Murine model of Niemann-Pick C disease: mutation in a cholesterol homeostasis gene. Science 1997;277:232–235.

13. Naureckiene S, Sleat DE, Lackland H, Fensom A, Vanier MT, Wattiaux R, Jadot M, Lobel P. Identification of HE1 as the second gene of Niemann-Pick C disease. Science 2000;290:2298–2301.

14. Vanier MT. Niemann-Pick disease type C. Orphanet J Rare Dis 2010;5:16.

15. Millat G, Marçais C, Rafi MA, Yamamoto T, Morris JA, Pentchev PG, Ohno K, Wenger DA, Vanier MT. Niemann-Pick C1 disease: the I1061T substitution is a frequent mutant

allele in patients of Western European descent and correlates with a classic juvenile phenotype. Am J Hum Genet 1999;65:1321–1329.

16. Stenson PD, Ball EV, Mort M, Phillips AD, Shiel JA, Thomas NST, Abeysinghe S, Krawczak M, Cooper DN. Human Gene Mutation Database (HGMD): 2003 update. Hum Mutat 2003;21:577–581.

17. Li X, Saha P, Li J, Blobel G, Pfeffer SR. Clues to the mechanism of cholesterol transfer from the structure of NPC1 middle lumenal domain bound to NPC2. Proceedings of the National Academy of Sciences 2016;113:10079–10084.

18. Greer WL, Dobson MJ, Girouard GS, Byers DM, Riddell DC, Neumann PE. Mutations in NPC1 highlight a conserved NPC1-specific cysteine-rich domain. Am J Hum Genet 1999;65:1252–1260.

19. Peake KB, Vance JE. Defective cholesterol trafficking in Niemann-Pick C-deficient cells. FEBS Letters 2010;584:2731–2739.

20. Rodriguez-Lafrasse C, Rousson R, Pentchev PG, Louisot P, Vanier MT. Free sphingoid bases in tissues from patients with type C Niemann-Pick disease and other lysosomal storage disorders. Biochim Biophys Acta 1994;1226:138–144.

21. Patterson MC, Hendriksz CJ, Walterfang M, Sedel F, Vanier MT, Wijburg F, Group OBOTN-CGW. Recommendations for the diagnosis and management of Niemann–Pick disease type C: An update. Molecular Genetics and Metabolism 2012;106:330–344.

22. NP-C Guidelines Working Group, Wraith JE, Baumgartner MR, Bembi B, Covanis A, Levade T, Mengel E, Pineda M, Sedel F, Topçu M, Vanier MT, Widner H, Wijburg FA, Patterson MC. Recommendations on the diagnosis and management of Niemann-Pick disease type C. Molecular Genetics and Metabolism. 2009;98:152–165.

23. Wijburg FA, Sedel F, Pineda M, Hendriksz CJ, Fahey M, Walterfang M, Patterson MC, Wraith JE, Kolb SA. Development of a suspicion index to aid diagnosis of Niemann-Pick disease type C. Neurology 2012;78:1560–1567.

24. Spiegel R, Raas Rothschild A, Reish O, Regev M, Meiner V, Bargal R, Sury V, Meir K, Nadjari M, Hermann G, Iancu TC, Shalev SA, Zeigler M. The clinical spectrum of fetal Niemann–Pick type C. American Journal of Medical Genetics Part A 149A:446–450.

25. Louwette S, Régal L, Wittevrongel C, Thys C, Vandeweeghde G, Decuyper E, Leemans P, De Vos R, Van Geet C, Jaeken J, Freson K. NPC1 defect results in abnormal platelet formation and function: studies in Niemann-Pick disease type C1 patients and zebrafish. Human Molecular Genetics 2013;22:61–73.

26. Kelly DA, Portmann B, Mowat AP, Sherlock S, Lake BD. Niemann-Pick disease type C: diagnosis and outcome in children, with particular reference to liver disease. J Pediatr 1993;123:242–247.

27. Geberhiwot T, Moro A, Dardis A, Ramaswami U, Sirrs S, Marfa MP, Vanier MT, Walterfang M, Bolton S, Dawson C, Héron B, Stampfer M, Imrie J, Hendriksz C, Gissen P, Crushell E, Coll MJ, Nadjar Y, Klünemann H, Mengel E, Hrebicek M, Jones SA, Ory D, Bembi B, Patterson M, International Niemann-Pick Disease Registry (INPDR). Consensus clinical management guidelines for Niemann-Pick disease type C. Orphanet J Rare Dis 2018;13:50.

28. Gumus E, Haliloglu G, Karhan AN, Demir H, Gurakan F, Topçu M, Yuce A. Niemann-Pick disease type C in the newborn period: a single-center experience. Eur J Pediatr 2017;

29. Staretz-Chacham O, Aviram M, Morag I, Goldbart A, Hershkovitz E. Pulmonary involvement in Niemann-Pick C type 1. 2018;:1–7.

30. Sheth J, Joseph JJ, Shah K, Muranjan M, Mistri M, Sheth F. Pulmonary manifestations in Niemann-Pick type C disease with mutations in NPC2 gene: case report and review of literature. BMC Med Genet 2017;18:5.

31. Sevin M, Lesca G, Baumann N, Millat G, Lyon-Caen O, Vanier MT, Sedel F. The adult form of Niemann-Pick disease type C. Brain 2006;130:120–133.

32. Imrie J, Vijayaraghaven S, Whitehouse C, Harris S, Heptinstall L, Church H, Cooper A, Besley GTN, Wraith JE. Niemann-Pick disease type C in adults. J Inherit Metab Dis 2002;25:491–500.

33. Di Lazzaro V, Marano M, Florio L, De Santis S. Niemann-Pick type C: focus on the adolescent/adult onset form. Int J Neurosci 2016;126:963–971.

34. Pineda M, Walterfang M, Patterson MC. Miglustat in Niemann-Pick disease type C patients: a review. Orphanet J Rare Dis 2018;13:140.

35. Platt FM, Neises GR, Dwek RA, Butters TD. N-butyldeoxynojirimycin is a novel inhibitor of glycolipid biosynthesis. J Biol Chem 1994;269:8362–8365.

36. Platt FM. Sphingolipid lysosomal storage disorders. Nature 2014;510:68–75.

37. Lloyd-Evans E, Morgan AJ, He X, Smith DA, Elliot-Smith E, Sillence DJ, Churchill GC, Schuchman EH, Galione A, Platt FM. Niemann-Pick disease type C1 is a sphingosine storage disease that causes deregulation of lysosomal calcium. Nat Med 2008;14:1247–1255.

38. Patterson MC, Vecchio D, Prady H, Abel L, Wraith JE. Miglustat for treatment of Niemann-Pick C disease: a randomised controlled study. Lancet Neurol 2007;6:765–772.

39. Bradbury A, Bagel J, Sampson M, Farhat N, Ding W, Swain G, Prociuk M, O'Donnell P, Drobatz K, Gurda B, Wassif C, Remaley A, Porter F, Vite C. Cerebrospinal Fluid Calbindin D Concentration as a Biomarker of Cerebellar Disease Progression in Niemann-Pick Type C1 Disease. J Pharmacol Exp Ther 2016;358:254–261.

40. Davidson CD, Ali NF, Micsenyi MC, Stephney G, Renault S, Dobrenis K, Ory DS, Vanier MT, Walkley SU. Chronic cyclodextrin treatment of murine Niemann-Pick C disease ameliorates neuronal cholesterol and glycosphingolipid storage and disease progression. PLoS ONE 2009;4:e6951.

41. Vite CH, Bagel JH, Swain GP, Prociuk M, Sikora TU, Stein VM, O'Donnell P, Ruane T, Ward S, Crooks A, Li S, Mauldin E, Stellar S, De Meulder M, Kao ML, Ory DS, Davidson C, Vanier MT, Walkley SU. Intracisternal cyclodextrin prevents cerebellar dysfunction and Purkinje cell death in feline Niemann-Pick type C1 disease. Science Translational Medicine 2015;7:276ra26–276ra26.

42. Ory DS, Ottinger EA, Farhat NY, King KA, Jiang X, Weissfeld L, Berry-Kravis E, Davidson CD, Bianconi S, Keener LA, Rao R, Soldatos A, Sidhu R, Walters KA, Xu X, Thurm A, Solomon B, Pavan WJ, Machielse BN, Kao M, Silber SA, McKew JC, Brewer CC, Vite CH, Walkley SU, Austin CP, Porter FD. Intrathecal 2-hydroxypropyl-beta-cyclodextrin decreases neurological disease progression in Niemann-Pick disease, type C1: a non-randomised, open-label, phase 1-2 trial. Lancet 2017;390:1758–1768.

43. Kirkegaard T, Gray J, Priestman DA, Wallom K-L, Atkins J, Olsen OD, Klein A, Drndarski S, Petersen NHT, Ingemann L, Smith DA, Morris L, Bornæs C, Jørgensen SH, Williams I, Hinsby A, Arenz C, Begley D, Jäättelä M, Platt FM. Heat shock protein-based therapy as a potential candidate for treating the sphingolipidoses. Science Translational Medicine 2016;8:355ra118–355ra118.

44. Ohashi T. Gene therapy for lysosomal storage diseases and peroxisomal diseases. Journal of Human Genetics 2019;64:139–143.

45. Chandler RJ, Williams IM, Gibson AL, Davidson CD, Incao AA, Hubbard BT, Porter FD, Pavan WJ, Venditti CP. Systemic AAV9 gene therapy improves the lifespan of mice with Niemann-Pick disease, type C1. Human Molecular Genetics 2017;26:52–64.

46. Hughes MP, Smith DA, Morris L, Fletcher C, Colaco A, Huebecker M, Tordo J, Palomar N, Massaro G, Henckaerts E, Waddington SN, Platt FM, Rahim AA. AAV9 intracerebroventricular gene therapy improves lifespan, locomotor function and pathology in a mouse model of Niemann-Pick type C1 disease. Human Molecular Genetics 2018;27:3079–3098.

47. Barré-Sinoussi F, Montagutelli X. Animal models are essential to biological research: issues and perspectives. Future Sci OA 2015;1:FSO63.

48. Miller F, Zohar S, Stallard N, Madan J, Posch M, Hee SW, Pearce M, Vågerö M, Day S. Approaches to sample size calculation for clinical trials in rare diseases. Pharm Stat 2018;17:214–230.

49. Fog CK, Kirkegaard T. Animal models for Niemann-Pick type C: implications for drug discovery & development. Expert Opin Drug Discov 2019;:1–11.

50. Rinaldi C, Wood MJA. Antisense oligonucleotides: the next frontier for treatment of neurological disorders. Nat Rev Neurol 2018;14:9–21.

51. Malathi K, Higaki K, Tinkelenberg AH, Balderes DA, Almanzar-Paramio D, Wilcox LJ, Erdeniz N, Redican F, Padamsee M, Liu Y, Khan S, Alcantara F, Carstea ED, Morris JA, Sturley SL. Mutagenesis of the putative sterol-sensing domain of yeast Niemann Pick C-related protein reveals a primordial role in subcellular sphingolipid distribution. The Journal of Cell Biology 2004;164:547–556.

52. Berger AC, Hanson PK, Wylie Nichols J, Corbett AH. A yeast model system for functional analysis of the Niemann-Pick type C protein 1 homolog, Ncr1p. Traffic 2005;6:907–917.

53. Sym M, Basson M, Johnson C. A model for niemann-pick type C disease in the nematode Caenorhabditis elegans. Curr Biol 2000;10:527–530.

54. Huang X, Suyama K, Buchanan J, Zhu AJ, Scott MP. A Drosophila model of the Niemann-Pick type C lysosome storage disease: dnpc1a is required for molting and sterol homeostasis. Development 2005;132:5115–5124.

55. Tseng W-C, Loeb HE, Pei W, Tsai-Morris C-H, Xu L, Cluzeau CV, Wassif CA, Feldman B, Burgess SM, Pavan WJ, Porter FD. Modeling Niemann-Pick disease type C1 in zebrafish: a robust platform for in vivo screening of candidate therapeutic compounds. Disease Models \& Mechanisms 2018;11:dmm034165.

56. Lowenthal AC, Cummings JF, Wenger DA, Thrall MA, Wood PA, de Lahunta A. Feline sphingolipidosis resembling Niemann-Pick disease type C. Acta Neuropathologica 1990;81:189–197.

57. Kuwamura M, Awakura T, Shimada A, Umemura T, Kagota K, Kawamura N, Naiki M. Type C Niemann-Pick disease in a boxer dog. Acta Neuropathologica 1993;85:345–348.

58. Elrick MJ, Pacheco CD, Yu T, Dadgar N, Shakkottai VG, Ware C, Paulson HL, Lieberman AP. Conditional Niemann-Pick C mice demonstrate cell autonomous Purkinje cell neurodegeneration. Human Molecular Genetics 2010;19:837–847.

59. Maue RA, Burgess RW, Wang B, Wooley CM, Seburn KL, Vanier MT, Rogers MA, Chang CC, Chang T-Y, Harris BT, Graber DJ, Penatti CAA, Porter DM, Szwergold BS, Henderson LP, Totenhagen JW, Trouard TP, Borbon IA, Erickson RP. A novel mouse model of Niemann-Pick type C disease carrying a D1005G-Npc1 mutation comparable to commonly observed human mutations. Human Molecular Genetics 2012;21:730–750.

60. Miyawaki S, Mitsuoka S, Sakiyama T, Kitagawa T. Sphingomyelinosis, a new mutation in the mouse: a model of Niemann-Pick disease in humans. J Hered 1982;73:257–263.

61. Pentchev PG, Gal AE, Booth AD, Omodeo-Sale F, Fouks J, Neumeyer BA, Quirk JM, Dawson G, Brady RO. A lysosomal storage disorder in mice characterized by a dual deficiency of sphingomyelinase and glucocerebrosidase. Biochim Biophys Acta 1980;619:669–679.

62. Praggastis M, Tortelli B, Zhang J, Fujiwara H, Sidhu R, Chacko A, Chen Z, Chung C, Lieberman AP, Sikora J, Davidson C, Walkley SU, Pipalia NH, Maxfield FR, Schaffer

JE, Ory DS. A murine Niemann-Pick C1 I1061T knock-in model recapitulates the pathological features of the most prevalent human disease allele. Journal of Neuroscience 2015;35:8091–8106.

63. Xie X, Brown MS, Shelton JM, Richardson JA, Goldstein JL, Liang G. Amino acid substitution in NPC1 that abolishes cholesterol binding reproduces phenotype of complete NPC1 deficiency in mice. Proceedings of the National Academy of Sciences 2011;108:15330–15335.

64. Gómez-Grau M, Albaigès J, Casas J, Auladell C, Dierssen M, Vilageliu L, Grinberg D. New murine Niemann-Pick type C models bearing a pseudoexon-generating mutation recapitulate the main neurobehavioural and molecular features of the disease. Sci Rep 2017;7:41931.

65. Shio H, Fowler S, Bhuvaneswaran C, Morris MD. Lysosome lipid storage disorder in NCTR-BALB/c mice. II. Morphologic and cytochemical studies. The American Journal of Pathology 1982;108:150–159.

66. Morris MD, Bhuvaneswaran C, Shio H, Fowler S. Lysosome lipid storage disorder in NCTR-BALB/c mice. I. Description of the disease and genetics. The American Journal of Pathology 1982;108:140–149.

67. Gelsthorpe ME, Baumann N, Millard E, Gale SE, Langmade SJ, Schaffer JE, Ory DS. Niemann-Pick type C1 I1061T mutant encodes a functional protein that is selected for endoplasmic reticulum-associated degradation due to protein misfolding. J Biol Chem 2008;283:8229–8236.

68. Lipinski P, Jankowska I, Lugowska A, Musielak M, Pronicki M, Tylki-Szymanska A. Newborn presentation of Niemann-Pick disease type C - Difficulties and limitations of diagnostic methods. Pediatrics and Neonatology 2018;59:317–318.

69. Bamshad MJ, Ng SB, Bigham AW, Tabor HK, Emond MJ, Nickerson DA, Shendure J. Exome sequencing as a tool for Mendelian disease gene discovery. Nat Rev Genet 2011;12:745–755.

70. Scriver CR, Waters PJ. Monogenic traits are not simple: lessons from phenylketonuria. Trends Genet 1999;15:267–272.

71. Dipple KM, McCabe ER. Phenotypes of patients with “simple” Mendelian disorders are complex traits: thresholds, modifiers, and systems dynamics. Am J Hum Genet 2000;66:1729–1735.

72. Talbot B, Chen T-W, Zimmerman S, Joost S, Eckert AJ, Crow TM, Semizer-Cuming D, Seshadri C, Manel S. Combining Genotype, Phenotype, and Environment to Infer Potential Candidate Genes. J Hered 2017;108:207–216.

73. Shields PG, Harris CC. Cancer risk and low-penetrance susceptibility genes in gene-environment interactions. J Clin Oncol 2000;18:2309–2315.

74. Riordan JD, Nadeau JH. From Peas to Disease: Modifier Genes, Network Resilience, and the Genetics of Health. Am J Hum Genet 2017;101:177–191.

75. Vanier MT, Wenger DA, Comly ME, Rousson R, Brady RO, Pentchev PG. Niemann-Pick disease group C: clinical variability and diagnosis based on defective cholesterol esterification. A collaborative study on 70 patients. Clinical Genetics 1988;33:331–348.

76. Vanier MT, Rodriguez-Lafrasse C, Rousson R, Gazzah N, Juge MC, Pentchev PG, Revol A, Louisot P. Type C Niemann-Pick disease: spectrum of phenotypic variation in disruption of intracellular LDL-derived cholesterol processing. Biochim Biophys Acta 1991;1096:328–337.

77. Walterfang M, Fietz M, Abel L, Bowman E, Mocellin R, Velakoulis D. Gender dimorphism in siblings with schizophrenia-like psychosis due to Niemann-Pick disease type C. J Inherit Metab Dis 2009;32 Suppl 1:S221–6.

78. Miyawaki S, Yoshida H, Mitsuoka S, Enomoto H, Ikehara S. A mouse model for Niemann-Pick disease. Influence of genetic background on disease expression in spm/spm mice. J Hered 1986;77:379–384.

79. Zhang J, Erickson RP. A modifier of Niemann Pick C 1 maps to mouse chromosome 19. Mamm Genome 2000;11:69–71.

80. Parra J, Klein AD, Castro J, Morales MG, Mosqueira M, Valencia I, Cortés V, Rigotti A, Zanlungo S. Npc1 deficiency in the C57BL/6J genetic background enhances Niemann-Pick disease type C spleen pathology. Biochemical and Biophysical Research Communications 2011;413:400–406.

81. Calderon JF, Klein AD. Controversies on the potential therapeutic use of rapamycin for treating a lysosomal cholesterol storage disease. Molecular Genetics and Metabolism Reports 2018;15:135–136.

82. Behringer R, Gertsenstein M, Nagy KV, Nagy A. Manipulating the Mouse Embryo. 2014.

83. Yamamoto T, Feng J-H, Higaki K, Taniguchi M, Nanba E, Ninomiya H, Ohno K. Increased NPC1 mRNA in skin fibroblasts from Niemann-Pick disease type C patients. Brain and Development 2004;26:245–250.

84. Wangler MF, Yamamoto S, Chao H-T, Posey JE, Westerfield M, Postlethwait J, UDN MOTUDN, Hieter P, Boycott KM, Campeau PM, Bellen HJ. Model Organisms Facilitate Rare Disease Diagnosis and Therapeutic Research. Genetics 2017;207:9–27.

85. Bothwell LE, Greene JA, Podolsky SH, Jones DS. Assessing the Gold Standard--Lessons from the History of RCTs. N Engl J Med 2016;374:2175–2181.

86. Zervas M, Somers KL, Thrall MA, Walkley SU. Critical role for glycosphingolipids in Niemann-Pick disease type C. Curr Biol 2001;11:1283–1287.

87. Chung C, Elrick MJ, Dell'Orco JM, Qin ZS, Kalyana-Sundaram S, Chinnaiyan AM, Shakkottai VG, Lieberman AP. Heat Shock Protein Beta-1 Modifies Anterior to Posterior Purkinje Cell Vulnerability in a Mouse Model of Niemann-Pick Type C Disease. PLoS Genet 2016;12:e1006042.

88. Ko DC, Milenkovic L, Beier SM, Manuel H, Buchanan J, Scott MP. Cell-autonomous death of cerebellar purkinje neurons with autophagy in Niemann-Pick type C disease. PLoS Genet 2005;1:81–95.

89. Guyenet SJ, Furrer SA, Damian VM, Baughan TD, La Spada AR, Garden GA. A simple composite phenotype scoring system for evaluating mouse models of cerebellar ataxia. J Vis Exp 2010;:e1787.

90. Pipalia NH, Cosner CC, Huang A, Chatterjee A, Bourbon P, Farley N, Helquist P, Wiest O, Maxfield FR. Histone deacetylase inhibitor treatment dramatically reduces cholesterol accumulation in Niemann-Pick type C1 mutant human fibroblasts. Proceedings of the National Academy of Sciences 2011;108:5620–5625.

91. Sopher BL, Thomas PS, LaFevre-Bernt MA, Holm IE, Wilke SA, Ware CB, Jin L-W, Libby RT, Ellerby LM, La Spada AR. Androgen receptor YAC transgenic mice recapitulate SBMA motor neuronopathy and implicate VEGF164 in the motor neuron degeneration. Neuron 2004;41:687–699.

92. Thomas PS, Fraley GS, Damian V, Damien V, Woodke LB, Zapata F, Sopher BL, Plymate SR, La Spada AR. Loss of endogenous androgen receptor protein accelerates motor neuron degeneration and accentuates androgen insensitivity in a mouse model of X-linked spinal and bulbar muscular atrophy. Human Molecular Genetics 2006;15:2225–2238.

93. Davidson BA, Hassan S, Garcia EJ, Tayebi N, Sidransky E. Exploring genetic modifiers of Gaucher disease: The next horizon. Hum Mutat 2018;39:1739–1751.

94. Corvol H, Blackman SM, Boëlle P-Y, Gallins PJ, Pace RG, Stonebraker JR, Accurso FJ, Clement A, Collaco JM, Dang H, Dang AT, Franca A, Gong J, Guillot L, Keenan K, Li W, Lin F, Patrone MV, Raraigh KS, Sun L, Zhou Y-H, O'Neal WK, Sontag MK, Levy H, Durie PR, Rommens JM, Drumm ML, Wright FA, Strug LJ, Cutting GR, Knowles MR. Genome-wide association meta-analysis identifies five modifier loci of lung disease severity in cystic fibrosis. Nat Commun 2015;6:8382.

95. Venturini G, Rose AM, Shah AZ, Bhattacharya SS, Rivolta C. CNOT3 is a modifier of PRPF31 mutations in retinitis pigmentosa with incomplete penetrance. PLoS Genet 2012;8:e1003040.

96. Haider NB, Zhang W, Hurd R, Ikeda A, Nystuen AM, Naggert JK, Nishina PM. Mapping of genetic modifiers of Nr2e3 rd7/rd7 that suppress retinal degeneration and restore blue cone cells to normal quantity. Mamm Genome 2008;19:145–154.

97. He W, Bai G, Zhou H, Wei N, White NM, Lauer J, Liu H, Shi Y, Dumitru CD, Lettieri K, Shubayev V, Jordanova A, Guergueltcheva V, Griffin PR, Burgess RW, Pfaff SL,

Yang X-L. CMT2D neuropathy is linked to the neomorphic binding activity of glycyl-tRNA synthetase. Nature 2015;526:710–714.

98. Morse HCI. Origins of Inbred Mice. Elsevier; 1972.

99. Beck JA, Lloyd S, Hafezparast M, Lennon-Pierce M, Eppig JT, Festing MF, Fisher EM. Genealogies of mouse inbred strains. Nat Genet 2000;24:23–25.

100. Ulett GC, Ketheesan N, Hirst RG. Cytokine gene expression in innately susceptible BALB/c mice and relatively resistant C57BL/6 mice during infection with virulent Burkholderia pseudomallei. Infect Immun 2000;68:2034–2042.

101. Koo GC, Gan Y-H. The innate interferon gamma response of BALB/c and C57BL/6 mice to in vitro Burkholderia pseudomallei infection. BMC Immunol 2006;7:19.

102. Sellers RS, Clifford CB, Treuting PM, Brayton C. Immunological variation between inbred laboratory mouse strains: points to consider in phenotyping genetically immunomodified mice. Vet Pathol 2012;49:32–43.

103. Simon MM, Greenaway S, White JK, Fuchs H, Gailus-Durner V, Wells S, Sorg T, Wong K, Bedu E, Cartwright EJ, Dacquin R, Djebali S, Estabel J, Graw J, Ingham NJ, Jackson IJ, Lengeling A, Mandillo S, Marvel J, Meziane H, Preitner F, Puk O, Roux M, Adams DJ, Atkins S, Ayadi A, Becker L, Blake A, Brooker D, Cater H, Champy M-F, Combe R, Danecek P, di Fenza A, Gates H, Gerdin A-K, Golini E, Hancock JM, Hans W, Hölter SM, Hough T, Jurdic P, Keane TM, Morgan H, Müller W, Neff F, Nicholson G, Pasche B, Roberson L-A, Rozman J, Sanderson M, Santos L, Selloum M, Shannon C, Southwell A, Tocchini-Valentini GP, Vancollie VE, Westerberg H, Wurst W, Zi M, Yalcin B, Ramirez-Solis R, Steel KP, Mallon A-M, de Angelis MH, Herault Y, Brown SDM. A comparative phenotypic and genomic analysis of C57BL/6J and C57BL/6N mouse strains. Genome Biol 2013;14:R82.

104. Cox A, Ackert-Bicknell CL, Dumont BL, Ding Y, Bell JT, Brockmann GA, Wergedal JE, Bult C, Paigen B, Flint J, Tsaih S-W, Churchill GA, Broman KW. A new standard genetic map for the laboratory mouse. Genetics 2009;182:1335–1344.

105. Liu EY, Morgan AP, Chesler EJ, Wang W, Churchill GA, Pardo-Manuel de Villena F. High-resolution sex-specific linkage maps of the mouse reveal polarized distribution of crossovers in male germline. Genetics 2014;197:91–106.

106. Smith R, Sheppard K, DiPetrillo K, Churchill G. Quantitative trait locus analysis using J/qtl. Methods Mol Biol 2009;573:175–188.

107. Broman KW, Wu H, Sen S, Churchill GA. R/qtl: QTL mapping in experimental crosses. Bioinformatics 2003;19:889–890.

108. Manichaikul A, Dupuis J, Sen S, Broman KW. Poor performance of bootstrap confidence intervals for the location of a quantitative trait locus. Genetics 2006;174:481–489.

109. Eilbeck K, Quinlan A, Yandell M. Settling the score: variant prioritization and Mendelian disease. Nat Rev Genet 2017;18:599–612.

110. Choi Y, Sims GE, Murphy S, Miller JR, Chan AP. Predicting the functional effect of amino acid substitutions and indels. PLoS ONE 2012;7:e46688.

111. Landrum MJ, Lee JM, Benson M, Brown G, Chao C, Chitipiralla S, Gu B, Hart J, Hoffman D, Hoover J, Jang W, Katz K, Ovetsky M, Riley G, Sethi A, Tully R, Villamarin-Salomon R, Rubinstein W, Maglott DR. ClinVar: public archive of interpretations of clinically relevant variants. Nucleic Acids Res 2016;44:D862–8.

112. Nadeau JH. Modifier genes in mice and humans. Nat Rev Genet 2001;2:165–174.

113. Buchovecky CM, Turley SD, Brown HM, Kyle SM, McDonald JG, Liu B, Pieper AA, Huang W, Katz DM, Russell DW, Shendure J, Justice MJ. A suppressor screen in Mecp2 mutant mice implicates cholesterol metabolism in Rett syndrome. Nat Genet 2013;45:1013–1020.

114. Owens IS, Basu NK, Banerjee R. UDP-glucuronosyltransferases: gene structures of UGT1 and UGT2 families. Meth Enzymol 2005;400:1–22.

115. Kutsuno Y, Hirashima R, Sakamoto M, Ushikubo H, Michimae H, Itoh T, Tukey RH, Fujiwara R. Expression of UDP-Glucuronosyltransferase 1 (UGT1) and Glucuronidation Activity toward Endogenous Substances in Humanized UGT1 Mouse Brain. Drug Metab Dispos 2015;43:1071–1076.

116. Bosma PJ, Chowdhury JR, Bakker C, Gantla S, de Boer A, Oostra BA, Lindhout D, Tytgat GN, Jansen PL, Oude Elferink RP. The genetic basis of the reduced expression of bilirubin UDP-glucuronosyltransferase 1 in Gilbert's syndrome. N Engl J Med 1995;333:1171–1175.

117. CRIGLER JF, NAJJAR VA. Congenital familial nonhemolytic jaundice with kernicterus. PEDIATRICS 1952;10:169–180.

118. Shiratani H, Katoh M, Nakajima M, Yokoi T. Species differences in UDP-glucuronosyltransferase activities in mice and rats. Drug Metab Dispos 2008;36:1745–1752.

119. Nicoli E-R, Eisa Al N, Cluzeau CVM, Wassif CA, Gray J, Burkert KR, Smith DA, Morris L, Cologna SM, Peer CJ, Sissung TM, Uscatu C-D, Figg WD, Pavan WJ, Vite CH, Porter FD, Platt FM. Defective Cytochrome P450-Catalysed Drug Metabolism in Niemann-Pick Type C Disease. PLoS ONE 2016;11:e0152007.

120. McIntosh BB, Ostap EM. Myosin-I molecular motors at a glance. Journal of Cell Science 2016;129:2689–2695.

121. Santos-Argumedo L, Maravillas-Montero JL, López-Ortega O. Class I myosins in B-cell physiology: functions in spreading, immune synapses, motility, and vesicular traffic. Immunol Rev 2013;256:190–202.

122. Raposo G, Cordonnier MN, Tenza D, Menichi B, Dürrbach A, Louvard D, Coudrier E. Association of myosin I alpha with endosomes and lysosomes in mammalian cells. Mol Biol Cell 1999;10:1477–1494.

123. Cordonnier MN, Dauzonne D, Louvard D, Coudrier E. Actin filaments and myosin I alpha cooperate with microtubules for the movement of lysosomes. Mol Biol Cell 2001;12:4013–4029.

124. Iuliano O, Yoshimura A, Prospéri M-T, Martin R, Knölker H-J, Coudrier E. Myosin 1b promotes axon formation by regulating actin wave propagation and growth cone dynamics. The Journal of Cell Biology 2018;217:2033–2046.

125. Qiu J, Ogus S, Mounzih K, Ewart-Toland A, Chehab FF. Leptin-deficient mice backcrossed to the BALB/cJ genetic background have reduced adiposity, enhanced fertility, normal body temperature, and severe diabetes. Endocrinology 2001;142:3421–3425.

126. Song Y, Altarejos J, Goodarzi MO, Inoue H, Guo X, Berdeaux R, Kim J-H, Goode J, Igata M, Paz JC, Hogan MF, Singh PK, Goebel N, Vera L, Miller N, Cui J, Jones MR, CHARGE Consortium, GIANT Consortium, Chen Y-DI, Taylor KD, Hsueh WA, Rotter JI, Montminy M. CRTC3 links catecholamine signalling to energy balance. Nature 2010;468:933–939.

127. Ou Z, Wang G, Li Q, Ma Z, Dai M, Zou F. CRTC3 polymorphisms were associated with the plasma level of total cholesterol and the risks of overweight and hypertriglyceridemia in a Chinese Han population. Mol Biol Rep 2014;41:125–130.

128. MacKenzie KF, Clark K, Naqvi S, McGuire VA, Nöehren G, Kristariyanto Y, van den Bosch M, Mudaliar M, McCarthy PC, Pattison MJ, Pedrioli PGA, Barton GJ, Toth R, Prescott A, Arthur JSC. PGE(2) induces macrophage IL-10 production and a regulatory-like phenotype via a protein kinase A-SIK-CRTC3 pathway. J Immunol 2013;190:565–577.

129. Clark K, MacKenzie KF, Petkevicius K, Kristariyanto Y, Zhang J, Choi HG, Peggie M, Plater L, Pedrioli PGA, McIver E, Gray NS, Arthur JSC, Cohen P. Phosphorylation of CRTC3 by the salt-inducible kinases controls the interconversion of classically activated and regulatory macrophages. Proceedings of the National Academy of Sciences 2012;109:16986–16991.

130. Fleming BD, Mosser DM. Regulatory macrophages: setting the threshold for therapy. Eur J Immunol 2011;41:2498–2502.

131. Garver WS, Jelinek D, Meaney FJ, Flynn J, Pettit KM, Shepherd G, Heidenreich RA, Vockley CMW, Castro G, Francis GA. The National Niemann-Pick Type C1 Disease Database: correlation of lipid profiles, mutations, and biochemical phenotypes. The Journal of Lipid Research 2010;51:406–415.

132. Jelinek D, Castillo JJ, Garver WS. The C57BL/6J Niemann-Pick C1 mouse model with decreased gene dosage has impaired glucose tolerance independent of body weight. Gene 2013;527:65–70.

133. Lamri A, Pigeyre M, Garver WS, Meyre D. The Extending Spectrum of NPC1-Related Human Disorders: From Niemann-Pick C1 Disease to Obesity. Endocr Rev 2018;39:192–220.

134. Meyre D, Delplanque J, Chèvre J-C, Lecoeur C, Lobbens S, Gallina S, Durand E, Vatin V, Degraeve F, Proença C, Gaget S, Körner A, Kovacs P, Kiess W, Tichet J, Marre M, Hartikainen A-L, Horber F, Potoczna N, Hercberg S, Levy-Marchal C, Pattou F, Heude B, Tauber M, McCarthy MI, Blakemore AIF, Montpetit A, Polychronakos C, Weill J, Coin LJM, Asher J, Elliott P, Järvelin M-R, Visvikis-Siest S, Balkau B, Sladek R, Balding D, Walley A, Dina C, Froguel P. Genome-wide association study for early-onset and morbid adult obesity identifies three new risk loci in European populations. Nat Genet 2009;41:157–159.

135. Borbon I, Campbell E, Ke W, Erickson RP. The role of decreased levels of Niemann-Pick C1 intracellular cholesterol transport on obesity is reversed in the C57BL/6J, metabolic syndrome mouse strain: a metabolic or an inflammatory effect? J Appl Genet 2012;53:323–330.

136. Gloss BS, Dinger ME. Realizing the significance of noncoding functionality in clinical genomics. Exp Mol Med 2018;50:97.

137. Garver WS, Francis GA, Jelinek D, Shepherd G, Flynn J, Castro G, Walsh Vockley C, Coppock DL, Pettit KM, Heidenreich RA, Meaney FJ. The National Niemann-Pick C1 disease database: report of clinical features and health problems. American Journal of Medical Genetics Part A 2007;143A:1204–1211.

138. Maconochie IK, Chong S, Mieli-Vergani G, Lake BD, Mowat AP. Fetal ascites: an unusual presentation of Niemann-Pick disease type C. Arch Dis Child 1989;64:1391–1393.

139. Manning DJ, Price WI, Pearse RG. Fetal ascites: an unusual presentation of Niemann-Pick disease type C. Arch Dis Child 1990;65:335–336.

140. Colin E, Barth M, Boussion F, Latour P, Piguet-Lacroix G, Guichet A, Ziegler A, Triau S, Loisel D, Sentilhes L, Bonneau D. In Utero Diagnosis of Niemann-Pick Type C in the Absence of Family History. JIMD Rep 2016;28:105–110.

141. Ovchinnikov D. Alcian blue/alizarin red staining of cartilage and bone in mouse. Cold Spring Harb Protoc 2009;2009:pdb.prot5170.

142. Albert M, Schmitz SU, Kooistra SM, Malatesta M, Morales Torres C, Rekling JC, Johansen JV, Abarrategui I, Helin K. The histone demethylase Jarid1b ensures faithful mouse development by protecting developmental genes from aberrant H3K4me3. PLoS Genet 2013;9:e1003461.

143. Klinger S, Turgeon B, Lévesque K, Wood GA, Aagaard-Tillery KM, Meloche S. Loss of Erk3 function in mice leads to intrauterine growth restriction, pulmonary immaturity, and neonatal lethality. Proceedings of the National Academy of Sciences 2009;106:16710–16715.

144. Cuevas Guaman M, Sbrana E, Shope C, Showalter L, Hu M, Meloche S, Aagaard K. Administration of antenatal glucocorticoids and postnatal surfactant ameliorates respiratory distress syndrome-associated neonatal lethality in Erk3(-/-) mouse pups. Pediatr Res 2014;76:24–32.

145. Pew BK, Harris RA, Sbrana E, Guaman MC, Shope C, Chen R, Meloche S, Aagaard K. Structural and transcriptomic response to antenatal corticosteroids in an Erk3-null mouse model of respiratory distress. Am J Obstet Gynecol 2016;215:384.e1–384.e89.

146. Hamvas A, Cole FS, Nogee LM. Genetic disorders of surfactant proteins. Neonatology 2007;91:311–317.

147. Whitsett JA, Wert SE, Trapnell BC. Genetic disorders influencing lung formation and function at birth. Human Molecular Genetics 2004;13 Spec No 2:R207–15.

148. Liggins GC, Howie RN. A controlled trial of antepartum glucocorticoid treatment for prevention of the respiratory distress syndrome in premature infants. PEDIATRICS 1972;50:515–525.

149. Roberts D, Brown J, Medley N, Dalziel SR. Antenatal corticosteroids for accelerating fetal lung maturation for women at risk of preterm birth. Cochrane Database Syst Rev 2017;3:CD004454.

150. Carstea ED, Morris JA, Coleman KG, Loftus SK, Zhang D, Cummings C, Gu J, Rosenfeld MA, Pavan WJ, Krizman DB, Nagle J, Polymeropoulos MH, Sturley SL, Ioannou YA, Higgins ME, Comly M, Cooney A, Brown A, Kaneski CR, Blanchette-Mackie EJ, Dwyer NK, Neufeld EB, Chang TY, Liscum L, Strauss JF, Ohno K, Zeigler M, Carmi R, Sokol J, Markie D, O'Neill RR, van Diggelen OP, Elleder M, Patterson MC, Brady RO, Vanier MT, Pentchev PG, Tagle DA. Niemann-Pick C1 disease gene: homology to mediators of cholesterol homeostasis. Science 1997;277:228–231.

151. Villavicencio EH, Walterhouse DO, Iannaccone PM. The sonic hedgehog-patched-gli pathway in human development and disease. Am J Hum Genet 2000;67:1047–1054.

152. Pepinsky RB, Zeng C, Wen D, Rayhorn P, Baker DP, Williams KP, Bixler SA, Ambrose CM, Garber EA, Miatkowski K, Taylor FR, Wang EA, Galdes A. Identification of a palmitic acid-modified form of human Sonic hedgehog. J Biol Chem 1998;273:14037–14045.

153. Fitzky BU, Witsch-Baumgartner M, Erdel M, Lee JN, Paik YK, Glossmann H, Utermann G, Moebius FF. Mutations in the Delta7-sterol reductase gene in patients with the Smith-Lemli-Opitz syndrome. Proc Natl Acad Sci USA 1998;95:8181–8186.

154. Porter FD. Smith-Lemli-Opitz syndrome: pathogenesis, diagnosis and management. Eur J Hum Genet 2008;16:535–541.

155. Canterini S, Dragotto J, Dardis A, Zampieri S, De Stefano ME, Mangia F, Erickson RP, Fiorenza MT. Shortened primary cilium length and dysregulated Sonic hedgehog signaling in Niemann-Pick C1 disease. Human Molecular Genetics 2017;26:2277–2289.

156. Sharma D, Shastri S, Sharma P. Intrauterine Growth Restriction: Antenatal and Postnatal Aspects. Clin Med Insights Pediatr 2016;10:67–83.

157. Staretz-Chacham O, Lang TC, LaMarca ME, Krasnewich D, Sidransky E. Lysosomal storage disorders in the newborn. PEDIATRICS 2009;123:1191–1207.

158. Guillemot N, Troadec C, de Villemeur TB, Clement A, Fauroux B. Lung disease in Niemann-Pick disease. Pediatr Pulmonol 2007;42:1207–1214.

159. Odom DT, Dowell RD, Jacobsen ES, Gordon W, Danford TW, MacIsaac KD, Rolfe PA, Conboy CM, Gifford DK, Fraenkel E. Tissue-specific transcriptional regulation has diverged significantly between human and mouse. Nat Genet 2007;39:730–732.

160. Jones EA, Clement-Jones M, James OF, Wilson DI. Differences between human and mouse alpha-fetoprotein expression during early development. J Anat 2001;198:555–559.

161. Bernhard W. Lung surfactant: Function and composition in the context of development and respiratory physiology. Ann Anat 2016;208:146–150.

162. Rooney SA, Young SL, Mendelson CR. Molecular and cellular processing of lung surfactant. FASEB J 1994;8:957–967.

163. Edwards V, Cutz E, Viero S, Moore AM, Nogee L. Ultrastructure of Lamellar Bodies in Congenital Surfactant Deficiency. 2009;29:503–509.

164. Whitsett JA, Weaver TE. Hydrophobic Surfactant Proteins in Lung Function and Disease — NEJM. New England Journal of Medicine 2002;

165. Veldhuizen R, Nag K, Orgeig S, Possmayer F. The role of lipids in pulmonary surfactant. Biochim Biophys Acta 1998;1408:90–108.

166. Gunasekara L, Schürch S, Schoel WM, Nag K, Leonenko Z, Haufs M, Amrein M. Pulmonary surfactant function is abolished by an elevated proportion of cholesterol. Biochim Biophys Acta 2005;1737:27–35.

167. Vockeroth D, Gunasekara L, Amrein M, Possmayer F, Lewis JF, Veldhuizen RAW. Role of cholesterol in the biophysical dysfunction of surfactant in ventilator-induced lung injury. Am J Physiol Lung Cell Mol Physiol 2010;298:L117–25.

168. Roszell BR, Tao J-Q, Yu KJ, Huang S, Bates SR. Characterization of the Niemann-Pick C pathway in alveolar type II cells and lamellar bodies of the lung. Am J Physiol Lung Cell Mol Physiol 2012;302:L919–32.

169. Roszell BR, Tao J-Q, Yu KJ, Gao L, Huang S, Ning Y, Feinstein SI, Vite CH, Bates SR. Pulmonary abnormalities in animal models due to Niemann-Pick type C1 (NPC1) or C2 (NPC2) disease. PLoS ONE 2013;8:e67084.

170. Jan MM, Camfield PR. Nova Scotia Niemann-Pick disease (type D): clinical study of 20 cases. J Child Neurol 1998;13:75–78.

171. Walterfang M, Chien Y-H, Imrie J, Rushton D, Schubiger D, Patterson MC. Dysphagia as a risk factor for mortality in Niemann-Pick disease type C: systematic literature review and evidence from studies with miglustat. Orphanet J Rare Dis 2012;7:76.

172. KARRER HE. The ultrastructure of mouse lung: the alveolar macrophage. J Biophys Biochem Cytol 1958;4:693–700.

173. Mason RJ, Greene K, Voelker DR. Surfactant protein A and surfactant protein D in health and disease. Am J Physiol 1998;275:L1–13.

174. Vaandrager AB, van Golde LM. Lung surfactant proteins A and D in innate immune defense. Biol Neonate 2000;77 Suppl 1:9–13.

175. Bianconi SE, Hammond DI, Farhat NY, Dang Do A, Jenkins K, Cougnoux A, Martin K, Porter FD. Evaluation of age of death in Niemann-Pick disease, type C: Utility of disease support group websites to understand natural history. Molecular Genetics and Metabolism 2019;